

# **Towards quantum applications of buckled dome microcavity devices**

by

Lintong Bu

A thesis submitted in partial fulfillment of the requirements for the degree of

Master of Science

in

Photonics and Plasma

Department of Electrical and Computer Engineering  
University of Alberta

© Lintong Bu, 2022

# Abstract

This thesis describes the theory, fabrication, and characterization of monolithic integrated membrane-in-the-middle (MIM) optomechanical Fabry-Perot resonators and elliptical birefringent Fabry-Perot optical resonators. Both types of devices were fabricated on a silicon wafer using a thin-film buckling self-assembly technique.

The MIM optomechanical cavity work follows that of a previous student, who had developed a method for releasing a free-standing silicon nitride (SiN) membrane embedded in a buckled dome microcavity, by using a surface micromachining (sacrificial etching) approach. In the present work, an improved photolithography method and an improved PECVD recipe for SiN deposition were developed. Concurrently, a vacuum system was designed and constructed, enabling optical measurements to be performed under a vacuum environment. Finally, in-situ vacuum-sealing of the optical cavities was attempted by deposition of various ‘sealing’ layers such as parylene deposition, sputtering of Si/SiO<sub>2</sub>, and plasma enhance chemical vapor deposition (PECVD) of SiO<sub>2</sub>. While these attempts were not entirely successful, they did provide an important basis for future work. The fabricated optical cavities exhibited a finesse of  $\sim 500$  at 1550 nm wavelength range. Furthermore, mechanical vibrational modes were observed with mechanical quality factor  $\sim 200$  for fundamental resonant frequencies in the  $\sim 5\text{MHz}$ - $15\text{MHz}$  range for different devices.

For the elliptical cavities, buckled domes with a large difference in radius of curvature along the major and minor axis were realized through appropriate patterning of a low-adhesion layer. These birefringent optical cavities exhibit astigmatism (two nested sets of Hermite-Gaussian modes reflecting the two radii of curvature) and birefringence (slightly non-degenerate

resonant wavelengths for polarization along the major and minor axes of the ellipse). The observed astigmatism and birefringence are in good agreement with the predictions of a vector-modified paraxial wave theory. The cavities exhibited finesse of  $\sim 250$  at 1550 nm wavelength range and polarization-mode splitting of the fundamental mode by  $\sim 25$  GHz.

# Preface

This thesis contains the works that are the product of the whole research group of Professor Ray DeCorby. Both the MIM project and the elliptical birefringent optical cavity project (including the theory, fabrication, and characterization) were a collaboration between Dr. DeCorby, Mr. Graham Hornig, Ms. Sanaa Al-Sumaidae, and the author. For all the nanofabrication techniques, the whole research group has put great effort into preparing standard operating procedure (SOP), characterizing thin films, and supporting each other. Mr. Timothy Harrison and Mr. Kyle Scheuer helped the author in cleaning and sample preparation and providing ideas regarding fabrication processes.

Chapter 3 of the thesis is a version of the following published article: G. J. Hornig, L. Bu, S. Al-Sumaidae, and R. G. DeCorby, “Monolithic elliptical dome Fabry–Perot microcavities exhibiting large birefringence”, *J. Opt. Soc. Am. B* **39**(3), 884-890 (2022), where G. J. H, and L. B. were both identified as first authors due to their equal contributions to the work. L. B. led the experimental effort, while G. J. H. and L. B. jointly developed the theoretical model. L. B. and G. J. H. prepared the manuscript, with oversight from R. G. D.

Chapter 4 of the thesis is a set of so-far unpublished results regarding the second-generation of MIM optical cavity devices.

There is no conflict of interest.

# Acknowledgments

First, I would like to thank my supervisor Dr. Ray DeCorby for your mentorship for both projects. Thank you for having me as a graduate student and giving me this opportunity to learn as both an engineer and a graduate student. This is a lifetime experience for me. Conducting research is never easy, especially in a global pandemic. Thank you for all the support during this era of human history.

Secondly, I want to thank my colleagues: Tim Harrison for management of the lab and insight into fabrication processes. Graham Hornig for collaborating with me with various projects and your solid foundation about theories. Kyle Schueur for numerous inspiring ideas in both research and registration affair since we were admitted to the research group together. As well as Dr. Sanna Al-Sumaidae for helping in measurements and support. Dr. Seyed Azmayesh for sharing the same optical table with endless interesting talks. Danny Pulikkaseril for chatting in the cleanroom.

I also want to thank My parents Shenghua Bu and Yiwen Gao for their love and support. My girlfriend Leguan Wang for love and support. My cat Isaac for sitting on my laptop and purring.

Finally, I want to acknowledge the financial support of Alberta Government, and the University of Alberta.

## Contents

Chapter 1 - Introduction.....	1
1.1 Cavity Quantum Electrodynamics (C-QED) .....	1
1.2 Cavity Optomechanical Systems .....	2
1.3 Membrane-in-the-middle optomechanical systems .....	4
1.4 Historical work by the DeCorby research group .....	6
1.5 Description of the research project .....	8
1.6 Outline of the thesis .....	10
Chapter 2 -Theory .....	12
2.1- Bragg Mirrors .....	13
2.2 Fabry-Perot cavity/ Optical resonator .....	15
2.2.1 General definition .....	15
2.2.2 Free spectral range .....	16
2.2.3 Finesse.....	17
2.2.4 Quality factor .....	17
2.3 Gaussian beams.....	18
2.3.1 The general description of a Gaussian beam .....	19
2.3.2 Transverse higher-order Gaussian modes .....	20
2.4 Buckling process.....	23
2.5 Membrane resonators.....	25
2.5.1 Basic differential equation for a mechanical resonator.....	25
2.5.2 Quality factor of mechanical resonators .....	27
2.5.3 Viscous damping.....	28
2.5.4 Clamping loss.....	29
2.5.5 Optimization of the mechanical quality factor.....	30
2.5.6 Dissipation dilution.....	30
2.6 Thermomechanical calibration.....	31
2.7 Cavity optomechanics.....	33
2.7.1 Theory .....	34
2.7.2 Tuned-to-slope measurements .....	35

Chapter 3 – Fabrication and process flow.....	37
3.1 Fabrication of MIM device .....	37
3.2 Vacuum sealing of MIM device .....	40
3.3 Optimization of fabrication processes .....	44
3.3.1 Heidelberg MLA 150 maskless aligner .....	44
3.3.2 PECVD recipe.....	45
3.4 Fabrication of elliptical devices .....	47
Chapter 4 - Monolithic elliptical dome Fabry-Perot microcavities exhibiting large birefringence .....	49
4.1 Background and Introduction .....	49
4.2 Fabrication and Cavity Geometry.....	50
4.3 Plano-ellipsoidal cavities – theoretical treatment .....	54
4.3.1 Elliptical Gaussian beam modes .....	54
4.3.2 Vector modifications – mode birefringence .....	57
4.4 Plano-ellipsoidal microcavities – experimental .....	58
4.5 Discussion and conclusions .....	63
Chapter 5 -Integrated membrane-in-the-middle (MIM) cavity optomechanical devices .....	65
5.1 Optical studies of fabricated MIM devices before and after sealing attempts.....	67
5.1.1 Reflection mode measurement.....	68
5.1.2 Transmission mode measurement.....	68
5.2 Experimental results.....	69
5.2.1 Spectral response .....	69
5.2.2 No Sealing/ Control group.....	71
5.2.3 Sputter Sealing (sealing attempt 1 and 2) .....	73
5.2.4 Parylene Sealing Attempt (sealing attempt 3) .....	76
5.2.5 PECVD Sealing Attempt (sealing attempt 4) .....	78
5.2.6 Evidence for coupled mechanical resonators after the PECVD sealing attempt .....	83
5.2.7 Discussion .....	86
Chapter 6 - Conclusion, and future work.....	87
6.1 Summary .....	87
6.2 Future work.....	88

Reference .....	90
Appendix A- Record of Fabrication of the Device .....	97



## List of Tables

Table 2.1 the numerical value of nth zero of m-th Bessel function.....	26
Table 3.1 a summary of the attempts to vacuum seal the dome optical cavity.....	42
Table 3.2 a summary of the vacuum sealing methods attempted .....	42
Table 3.3 PECVD deposition parameters and their relationship with the thin film stress, adapted from [49]. RF power I and RF power II are the power of low RF (356 kHz) frequency and high (13.5 MHz) RF frequency respectively. [49].....	46
Table 4.1 Estimates of the polarization splitting for the fundamental cavity mode .....	62
Table 5.1 The frequency and quality factor selected mechanical mode of representative devices 1,2, and 3 from trial 2, compared to a similar size device from the control group.....	75
Table 5.2 The frequency and quality factor for selected mechanical modes of representative devices 1,2, and 3 from the chip coated with parylene in trial 3 and compared to the control group device.....	78
Table 5.3 The frequency and quality factor selected mechanical mode of samples 1,2, and 3 in trial 4. Defining quality factors for some peaks are not possible due to their asymmetric line shape which will be noted as NA.....	82
Table A.1 The detailed record of the sputtering deposition of bottom mirror.....	98
Table A.2 The result from scratch test using Estralus System for Teflon deposition .....	102
Table A.3 The recipe of Estralus for Teflon deposition .....	102
Table A.4 The detailed record of the sputtering deposition of top mirror .....	103
Table A.5 The detailed record of the sputtering deposition for vacuum sealing, first trial .....	106
Table A.6 The detailed record of the sputtering deposition for vacuum sealing, second trial ...	106

## List of Figures

Figure 1.1 A diagram showing a cavity QED system, adapted from [2].	2
Figure 1.2 Two realizations of cavity optomechanical systems; the optical cavity system (top), and the microwave cavity system (bottom), adapted from [4].	3
Figure 1.3 A cavity optomechanical system, adapted from [6]. (a), A vibrating mirror optomechanical system. (b), A membrane-in-the-middle optomechanical system. (c), An SEM image of a commercial silicon nitride membrane (Norcada). (d), a schematic diagram of a typical experimental setup.	4
Figure 1.4 (a), a commercial SiN membrane chip (Norcada) adapted from [6]. (b), optomechanical trampoline resonator, adapted from [10]. (c), left: a zoomed-out view of phononic crystal (soft clamping) resonator. Right: a zoomed-in version showing the ‘defect’ mechanical resonator in the center of the phononic crystal, adapted from [11].	5
Figure 1.5 The buckling self-assembly optical cavity, adapted from [14]. This is the original buckled optical cavity reported by the DeCorby group; further integration of emitters and mechanical resonators was pursued in subsequent work. (a) A cross-sectional schematic diagram, and (b) a microscope photo of an array of buckled cavities of various sizes.	7
Figure 1.6 (a), A small mode-volume channel-connected dome optical cavity, adapted from [15]. (b), A buckled-dome optical cavity with holes etched through the upper mirror to enable infiltration of gases or liquids into the cavity, adapted from [16]. (c), A microscope photo of a first-generation membrane-in-the-middle buckled-dome cavity, adapted from [8]. The circular structure is the optical cavity, whereas the floral structure is the released membrane.	8
Figure 1.7 (a), a microscope image of the MIM device, the outer semi-hexagonal ring is the released membrane, and the inner circular ring is the optical cavity. (b) a cross-section diagram of the MIM device.	9
Figure 1.8 The thermomechanical noise spectrum of the first generation MIM device, adapted from [8]. (a), the full spectrum with the main mechanical vibrational modes of the embedded membrane (as simulated using COMSOL) shown next to their predicted resonant frequencies. (b) The fundamental membrane vibrational mode (blue) along with a Lorentzian fitting (red).	10
Figure 2.1 A diagram of a QWS, with alternating high-index layers and low-index layers. Each period of the quarter wave stack will increase the total reflectance. Adapted from [19].	13
Figure 2.2 A reflectance versus wavelength plot of typical quarter wave stacks. For each curve, the period of QWS (N), the low index material (n2), and the high index material (n1) is labelled. Adapted from [19].	15
Figure 2.3 (a) A diagram showing light bouncing in an optical cavity. (b) Transverse modes of an optical cavity. (c) Line shape spectra of a planar Fabry-Perot optical cavity; each transmission line is well-described by a Lorentzian lineshape function. Adapted from [19].	16
Figure 2.4 a diagram showing that a plano concave Fabry-Perot cavity will exhibit Gaussian modes, adapted from [21].	18

Figure 2.5 (a) the shape of a fundamental Gaussian beam along the axis of propagation. (b) the intensity shaded profile of a Gaussian beam (c) a cross-sectional intensity profile of the Gaussian beam. Adapted from [19].	19
Figure 2.6 (a) The intensity profile of several Hermite-Gaussian modes. (b) The intensity profile of several Laguerre-Gaussian modes, adapted from [23] [24].	22
Figure 2.7 A diagram showing a buckling delamination process; when a thin film is under compressive stress, the film can delaminate and release some of its strain energy through buckling.	24
Figure 2.8 Different mode profiles of a circular vibrating membrane for modes $(m,n) = (1,0); (1,1); (1,1); (1,2); (1,2);$ and $(2,0)$ ; the red color and the blue color represent the positive and negative displacement of the membrane respectively, adapted from [28].	26
Figure 2.9 This is the same figure as Fig 1.4. (a), an SEM image of a SiN membrane resonator, adapted from [6]. (b) an optomechanical trampoline resonator, which minimizes the clamping loss by reducing physical contact between the central membrane ‘pad’ and the supporting frame, to reduce the elastic wave propagation, adapted from [29]. (c) A phononic crystal optomechanical resonator (a ‘soft clamping’ approach), which exploits forbidden bands for phonon propagation to limit the dissipation of thermal energy from the central ‘pad’ to the underlying substrate [11].	28
Figure 2.10 The thermomechanical noise spectrum of a mechanical oscillator at thermal equilibrium, adapted from [4].	31
Figure 2.11 A diagram illustrating the tuned-to-slope technique. (a) The blue curve is the Lorentzian lineshape of the optical cavity resonance, the red curve is the derivative of the Lorentzian, and the two vertical lines are the maximum slope locations, which is also the optimal probe laser settings to maximize the signal-to-noise ratio. (b), A diagram showing the relationship between optical detuning and optical intensity change.	35
Figure 3.1 The process flow of fabrication of MIM optomechanical resonator	40
Figure 3.2 A diagram showing four common deposition applications in semiconductor devices, adapted from [45].	41
Figure 3.3 A diagram showing various sealing techniques. A conformal sealing technique will deposit on all surfaces, whereas a line-of-sight sealing will only deposit on the surfaces which can directly receive sputter flux.	43
Figure 3.4 Photos showing the results of various trials aimed at vacuum sealing of the dome optical cavities. (a) 2 hours of SiO <sub>2</sub> sputtering to vacuum seal the optical cavity, corresponding to trial 2. (b) the sample for which the upper layers delaminated after 2 microns PECVD deposition; only the Si/SiO <sub>2</sub> layer got delaminated, which may have been due to poor adhesion resulting from lack of chip cleanliness prior to deposition of those layers. The outer ring corresponds to the membrane released by XeF <sub>2</sub> . (c)The delaminated sample from part (b) following sputtering of another Si/SiO <sub>2</sub> optical bilayer, which restored a sufficient optical quality factor to facilitate tuned-to-slope measurement, corresponding to trial 4.	43

Figure 3.5 The photograph of the alignment mark after all fabrication processes. (a) 5 magnification (b) 50 magnification .....	45
Figure 3.6 A thin film stress measurement of annealed PECVD nitride sample (~ 150 nm thick), deposited on a test (plain silicon) wafer, since the device wafer has additional layers that would affect the stress measurement. After the annealing process described in the main text, the stress is ~1 GPa tensile. ....	47
Figure 4.1 (a) Microscope image of an array of these devices. Note that 5 of the 6 devices shown are nominally identical, while the upper right device has a slightly less elongated profile. (b) Artist’s rendition of an elliptical dome Fabry-Perot microcavity, with an illustrated cutout showing the enclosed empty cavity. ....	51
Figure 4.2 Representative data for elliptical cavity devices labeled as type A (left column) and type B (right column). (a) Microscope images of the device, (b) 3D profilometer (ZYGO) scans of the devices, (c) Cross-sectional profile plot along the minor axis direction from the profilometer scan in part b. (red circles), along with a circle fit to the section of the curve spanning $\pm 10 \mu\text{m}$ from the peak (black dashed.) (d) As in part c., but for the major axis of each device. ....	53
Figure 4.3 Predicted (a-d) and observed (e-h) mode-field intensity profiles for selected low-order modes of the type B cavity. Simulations are plotted at $z = x = y = 0$ , and experimental measurements are taken focused at nominally the same point (the surface of the planar mirror.) All plots in the figure are on a common scale (scale bar: $10 \mu\text{m}$ ). ....	56
Figure 4.4 Spectral scans and mode-field intensity plots are shown for (a) device type A, and (b) device type B. In each case, the red curve corresponds to the input polarization aligned to minor (x) axis, while the blue curve corresponds to the input polarization aligned to the major (y) axis. Profile plots for (c) device type A and (d) device type B along x and y (green and magenta circles) of the fundamental TEM <sub>0,0</sub> elliptical mode (inset,) along with Gaussian fits. (solid lines.).....	60
Figure 4.5 Spectral scans near the resonant wavelength of the TEM <sub>0,0</sub> mode for: (a) the type A device and (b) the type B device for polarization along the minor (x) axis (red open circles) or along the major (y) axis (blue crosses). Lorentzian fits to the experimental data points are shown as a dashed line in each case. ....	61
Figure 5.1 The dependence of the mechanical Q-factor for a SiN drumhead membrane on the ambient pressure. Except for very low pressures where the Q-factor is limited by the intrinsic damping loss, the $1/Q$ is proportional to pressure. Adapted from [7].....	66
Figure 5.2 The vacuum chamber designed for optical measurements of microcavities at low ambient pressures. (a) an exploded-view schematic, (b) a photograph. ....	67
Figure 5.3 The experimental setup constructed to facilitate optical measurements of the MIM cavities is shown. This setup can perform the measurement of both the transmitted and reflected light from a cavity. The top right corner is a photo of the setup.....	67
Figure 5.4 Optical spectral response of two selected dome optical cavities, both with $50 \mu\text{m}$ base diameter. (a)(d), microscope photos of the domes. (b)(e), full-range optical scan. (c)(f) Short-	

range scan near the fundamental resonance as well as fitting of the fundamental mode lineshape to a Lorentzian profile. (Blue curve is the data, and red is the fitting) .....	70
Figure 5.5 (a), A typical thermo-mechanical noise spectrum for an ‘unsealed’ optical cavity. As discussed in the main text, the mechanical vibrational modes at various frequencies are attributed to either ‘mirror’ or ‘membrane’ oscillations. (b), a microscope photo of the optomechanical cavity.....	72
Figure 5.6 A sample spectral scan of a device from the chip which we attempted to seal through sputtering of additional layer. ....	74
Figure 5.7 (a)(c)(e), microscope image of devices from sealing attempt 2. (b)(d)(f) thermomechanical noise spectrum of the devices, taken from reflection mode measurements. ..	76
Figure 5.8 (a)(b) The thermomechanical noise spectrum after the parylene deposition attempt, showing that the peaks are broadened (i.e., lower mechanical quality factor) compared to trial 2 and also compared to the control devices. ....	78
Figure 5.9 A sample spectral scan of a device from the chip which we attempted to seal through PECVD deposition of additional layer. ....	80
Figure 5.10 (a) The microscope image after PECVD sealing but prior to re-sputtering Si/SiO <sub>2</sub> QWS, the outer perimeter of the released SiN membrane is visible, and the access holes appear to be sealed. (b) The microscope image of PECVD deposited chip after sputtering a Si/SiO <sub>2</sub> bilayer to regain sufficient optical Q for tuned-to-slope measurement. The perimeter of the membrane is no longer visible since Si is opaque to visible light. ....	80
Figure 5.11 (a)(b)(c), the thermomechanical noise spectrum after PECVD sealing and re-sputtering of a 1-period Si/SiO <sub>2</sub> bilayer (see main text). (a) shows an asymmetric Lorentzian at 20 MHz. (b) shows an asymmetric Lorentzian at 16 MHz, (c) shows an asymmetric Lorentzian at 16 MHz. ....	81
Figure 5.12 (a), the system diagram of an optomechanical system with coupled mechanical resonators, adapted from [70]. (b), the diagram of the setup in Qiang Lin’s work, adapted from [70]. (c), the cross-section diagram of the sample. (d) a microscope image of the studied dome, with a nominal base diameter of 50 μm.....	83
Figure 5.13 (a) Typical thermos-mechanical noise spectrum for the PECVD-deposited sample, with the device exhibiting an asymmetric Lorentzian feature at ~ 16.5 MHz, similar to the devices shown in Fig 4.17(b). (b), the zoomed and normalized view (From 14.3MHz to 18.2MHz) of the asymmetric Lorentzian, the MSE of the fitting is 7.0810. ....	84
Figure 5.14 The experimental data for the asymmetric resonance near 16.5 MHz, from Fig 4.19 (b). The blue curve is the experimental data, the red curve is the overall fitting using Eq. 4.2. The purple curve is for the assumed mode 1 (LDΩ), and the yellow curve is for the assumed mode 2 (LBΩ) associated with a coupled pair of mechanical oscillators. Mode 1 and 2 destructively interfere and form such an asymmetric line shape. ....	85

# Chapter 1 - Introduction

Quantum technologies are one of the most active areas of current research; they include quantum computing, quantum communication, and quantum sensing [1]. The demand for quantum technology is high, especially due to its potential in defense, encryption, and optimization. A long-term goal of our research group is to make a chip that can create, store, transduce, and detect quantum states. Furthermore, such a chip can be a building block of the quantum Internet [1], like its electronic counterpart.

## 1.1 Cavity Quantum Electrodynamics (C-QED)

Cavity quantum electrodynamics is focused on the interaction between light and atoms confined in an optical cavity [2]. It can be used to study fundamental quantum mechanics of open systems, the engineering of quantum states, and has potential applications in quantum information processing and transmission [3]. The simplest model involves an optical cavity with number state  $|n\rangle$ , and a two-level atom with ground state  $|g\rangle$  and excitation state  $|e\rangle$ . The Jaynes-Cummings Hamiltonian [2] [3] describes this system in terms of the atom, the electric field, and their interaction:

$$H_{\text{Jaynes-Cummings}} = \hbar\omega_r \left( a^\dagger a + \frac{1}{2} \right) + \frac{\hbar\Omega}{2} \sigma_z^2 + \hbar g (a^\dagger \sigma_- + a \sigma_+) + H_\kappa + H_\gamma \quad (\text{eq 1.1}) ,$$

where  $\hbar$  is the reduced Planck constant,  $\omega_r$  is the angular frequency of optical field,  $a^\dagger$  and  $a$  are creation and annihilation operators,  $\Omega$  is the atomic transition frequency,  $\sigma_z = |g\rangle\langle g| + |e\rangle\langle e|$  is the Hermitian Pauli operator,  $g$  is the coupling strength,  $\sigma_- = |e\rangle\langle g|$  and  $\sigma_+ = |g\rangle\langle e|$  are the atomic transition operator,  $H_\kappa$  and  $H_\gamma$  represent the photon decay ( $\kappa$ ) and atomic excited state decay ( $\gamma$ ) respectively [3]. This interaction is graphically illustrated in Fig 1.1

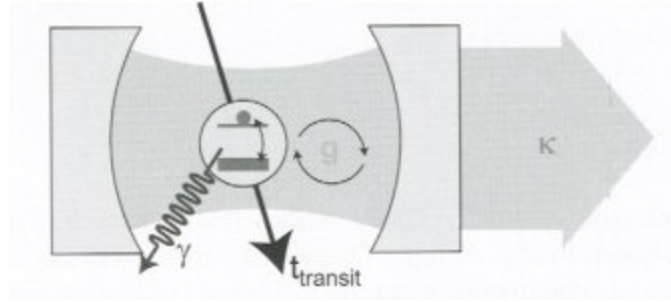


Figure 1.1 A diagram showing a cavity QED system, adapted from [2]

All the quantum states and interactions between quantum states are included in the Jaynes-Cummings Hamiltonian. Moreover, the C- QED system can be further categorized into two regimes, which are strong coupling ( $g \gg \kappa, \gamma$ ) and weak coupling ( $g \ll \kappa, \gamma$ ).

## 1.2 Cavity Optomechanical Systems

Cavity optomechanics is the field of study involving the interaction between light and mechanical objects confined within an optical cavity [4]. Figure 1.2 shows two realizations of cavity optomechanical systems, employing optical photons and microwave photons, respectively. Cavity optomechanical devices can potentially play the role of a ‘quantum transducer’ for converting quantum information between microwave and optical range frequencies, because mechanical subsystems can enable the exchange of quantum states between other physical entities such as electrons, photons, *etc.* [4] [5].

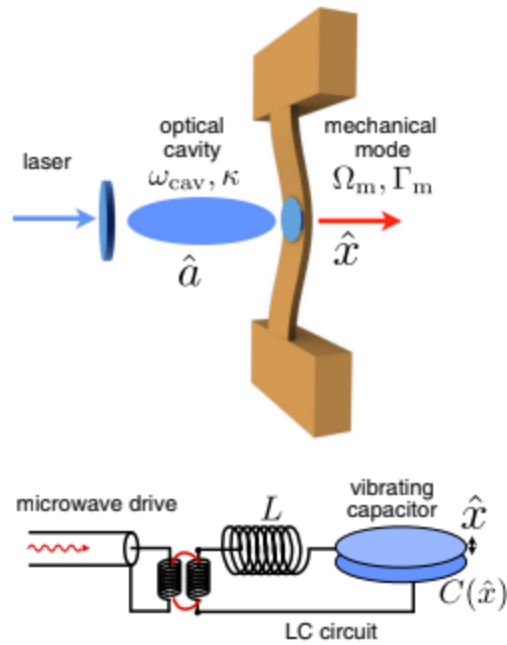


Figure 1.2 Two realizations of cavity optomechanical systems; the optical cavity system (top), and the microwave cavity system (bottom), adapted from [4].

The optomechanical system can be modeled in terms of the optical cavity, the mechanical resonator, and their interaction. Analogous to the C-QED system described above, the three most important quantities are the coupling rate ( $g$ ), the photon decay rate ( $\kappa$ ), and mechanical damping/ phonon decay rate ( $\Gamma_m$ ) [4].

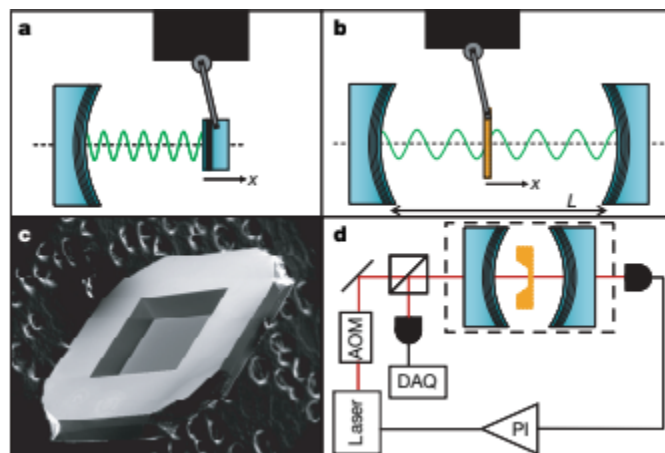




Figure 1.3 A cavity optomechanical system, adapted from [6]. (a), A vibrating mirror optomechanical system. (b), A membrane-in-the-middle optomechanical system. (c), An SEM image of a commercial silicon nitride membrane (Norcada). (d), a schematic diagram of a typical experimental setup.

### 1.3 Membrane-in-the-middle optomechanical systems

Amongst various implementations of cavity optomechanical devices, the membrane-in-the-middle (MIM) structure has attracted great interest [4] because of its simplicity and performance. Figure 1.3 (b) and (d) show a typical MIM cavity optomechanical system. A freely vibrating membrane is placed inside an optical cavity, such that the interaction and energy exchange between the optical cavity and the mechanical resonator are governed by a coupling parameter ( $g$ ).

The quality factor of the mechanical system ( $Q_m$ ) is a crucial parameter, and for example will determine the minimum detectable signal in sensing applications of a cavity optomechanical system. Another important quantity is the fundamental mechanical resonance frequency ( $f$ ), which for example will dictate the sampling frequency in sensing applications. To balance the quality factor and the resonator frequency, the  $Q$ - $f$  product is an often-used figure of merit [7]. Achieving a high mechanical quality factor can be realized by identifying and minimizing the loss mechanisms, which include: viscous damping, clamping loss, and material loss [8] [9]. Viscous damping is the energy loss to a viscous fluid, usually air or another gas, which is in contact with the vibrating mechanical element. Therefore, viscous damping can be minimized by performing measurements in a vacuum environment and reducing the temperature. Clamping loss is the energy loss through elastic waves which are propagated from the membrane resonator

to the supporting frame; it can be minimized by using a ‘trampoline’-style resonator or by use of phononic crystal (soft clamping) structures [10] [11]. Like photonic crystals, phononic crystals have a periodic structure such that certain frequency ranges of phonons, i.e. the quantization of mechanical vibration, are forbidden to propagate. [11] As a result, the energy loss due to clamping loss is minimized. Achieving high resonator frequency can be realized by making a smaller resonator.

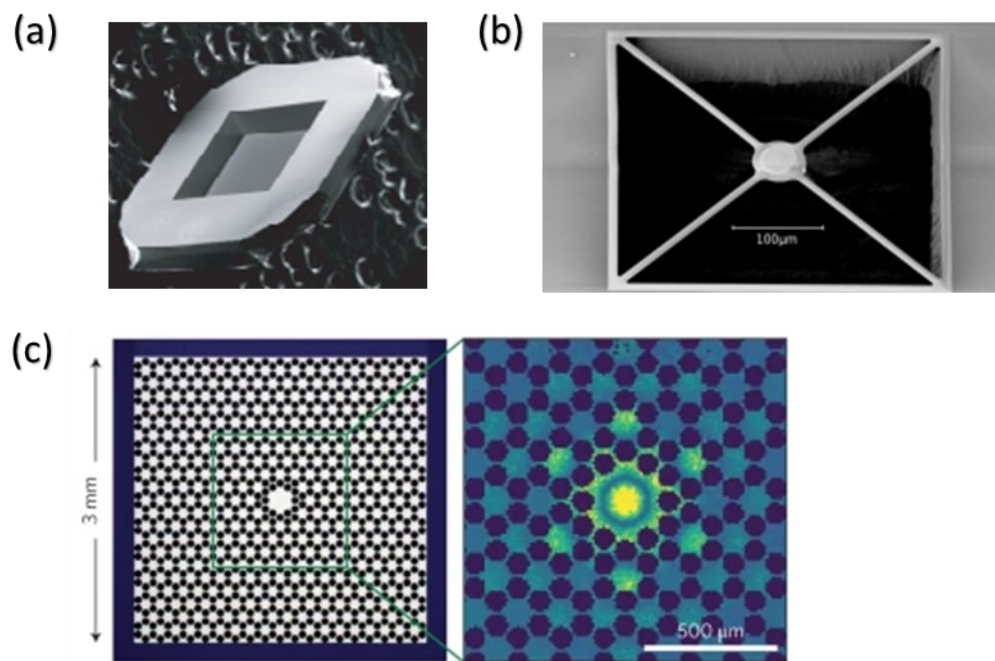


Figure 1.4 (a), a commercial SiN membrane chip (Norcada) adapted from [6]. (b), optomechanical trampoline resonator, adapted from [10]. (c), left: a zoomed-out view of phononic crystal (soft clamping) resonator. Right: a zoomed-in version showing the ‘defect’ mechanical resonator in the center of the phononic crystal, adapted from [11].

Nearly all MIM work to date has employed silicon nitride (SiN) membranes, which have been shown to support very high Q optical modes under appropriate processing conditions. A

few important historical milestones are summarized briefly as follows. J. D. Thompson *et al.* achieved a quality factor of  $1.2 * 10^7$  at a frequency of 130 kHz for measurements at low temperature (0.3 K) and low pressure ( $10^{-6}$  Torr) [6]. Dustin Kleckner *et al.* later proposed and demonstrated an optomechanical trampoline structure, which reduces the connection between the membrane and the supporting frame and thereby can reduce clamping losses. They achieved a quality factor of  $1.2 * 10^5$  at 300 mK, for a fundamental resonant frequency of 157.7 kHz [10]. Another approach to reducing the clamping loss is to employ a phononic crystal ‘shield’, where the fundamental resonant frequency of the mechanical oscillator is designed to lie in the forbidden band of the surrounding phononic crystal. Using this approach, Y. Tsaturyan *et al.* achieved a quality factor of  $\sim 1 * 10^8$  and a Q-f product of  $\sim 2 * 10^{14}$  [11]. Moreover, their measurements were performed at  $10^{-6}$  Torr and at room temperature.

The accelerometer is one of the applications of displacement sensing using a membrane in the middle structure. For a hanging membrane within an optical cavity, when acceleration occurs, the beam will have a certain displacement, similar to the force experience between a person and their seat in an accelerating car or plane. This displacement will affect the photon resonance frequency. [12]

#### **1.4 Historical work by the DeCorby research group**

When a thin-film stack has large compressive stress that exceeds a so-called critical stress, buckling delamination is one of the modes of fracture to release the stress [13]. Although this phenomenon is undesirable in most thin film deposition processes, our research group has developed a technology that uses a patterned low adhesion fluorocarbon film to control the locations and morphology of the thin film buckling delamination patterns. By depositing quarter

wave stack mirrors and controlling the adhesion at an interface embedded within them, high-quality plano-concave cavities can be fabricated [14]. This process is completely monolithic; thus, the whole fabrication process is scalable, repeatable, and ready for future integration.

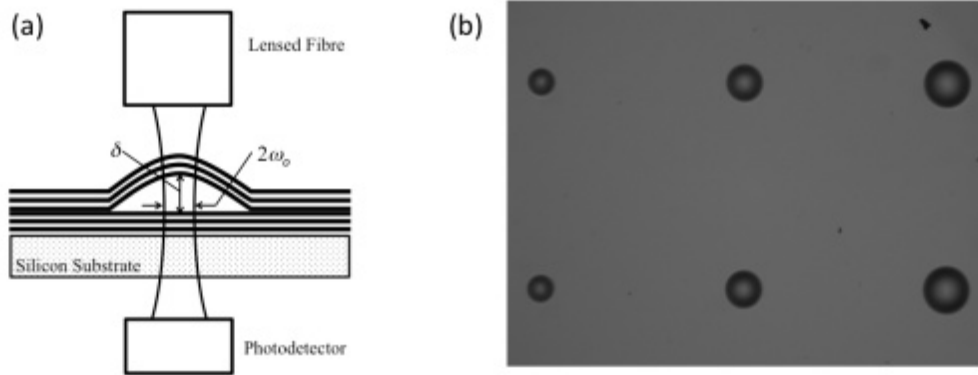


Figure 1.5 The buckling self-assembly optical cavity, adapted from [14]. This is the original buckled optical cavity reported by the DeCorby group; further integration of emitters and mechanical resonators was pursued in subsequent work. (a) A cross-sectional schematic diagram, and (b) a microscope photo of an array of buckled cavities of various sizes.

Moreover, by controlling the pattern of the low-adhesion fluorocarbon layer and by adding material and/or structures inside the self-assembled optical cavity, various integrated optical devices have been fabricated by our research group. This includes the integration of channel-connected domes [15], liquid infiltration of open-access optical cavities [16], and membrane-in-the-middle (MIM) cavity optomechanical structures [8].

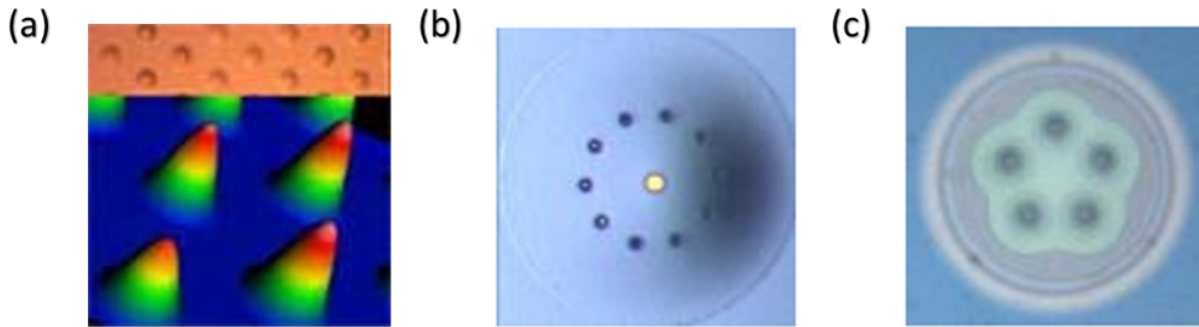


Figure 1.6 (a), A small mode-volume channel-connected dome optical cavity, adapted from [15].

(b), A buckled-dome optical cavity with holes etched through the upper mirror to enable infiltration of gases or liquids into the cavity, adapted from [16]. (c), A microscope photo of a first-generation membrane-in-the-middle buckled-dome cavity, adapted from [8]. The circular structure is the optical cavity, whereas the floral structure is the released membrane.

### 1.5 Description of the research project

My project involved the design, fabrication, and characterization of a monolithically integrated cavity optomechanical MIM structure. This project encompassed the development and application of novel nanotechnologies for fabricating the desired cavity optomechanical devices on a single chip, employing the tools commonly used for the fabrication of microelectronic devices. In simple terms, the MIM structure has an optical resonator and a mechanical resonator that is coupled together [4]. The optical resonator is made by a Fabry-Perot cavity, which is two highly reflective mirrors separated by a cavity spacer medium. The mechanical resonator is the membrane in the middle of the Fabry-Perot cavity. These are the main steps to fabricate such devices:

1. Bottom mirror deposition

2. Low adhesion layer deposition and patterning
3. Top mirror deposition
4. Buckle delamination self-assembly
5. Access hole etching
6. Membrane release by  $XeF_2$

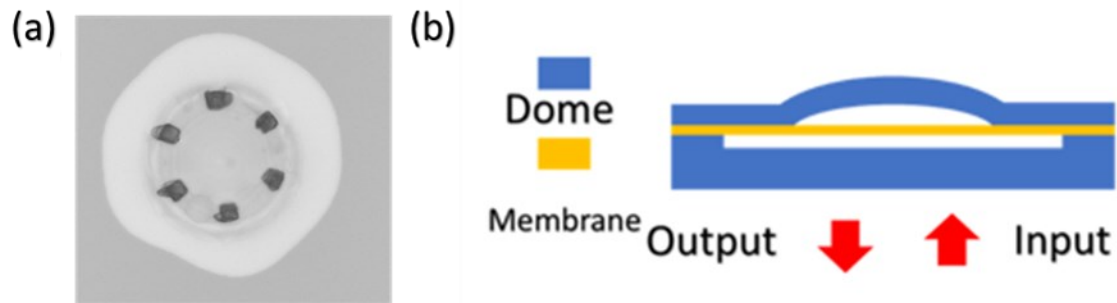


Figure 1.7 (a), a microscope image of the MIM device, the outer semi-hexagonal ring is the released membrane, and the inner circular ring is the optical cavity. (b) a cross-section diagram of the MIM device.

Our group has published a paper regarding this topic before [8], after Graham Hornig *et al.* successfully demonstrated a working membrane-in-the-middle optomechanical cavity. As shown in Fig.1.8, the thermomechanical noise spectrum indicates strong membrane modes exist; the quality factor of the fundamental mode is  $\sim 44$  and the fundamental frequency is about 10.5 MHz.

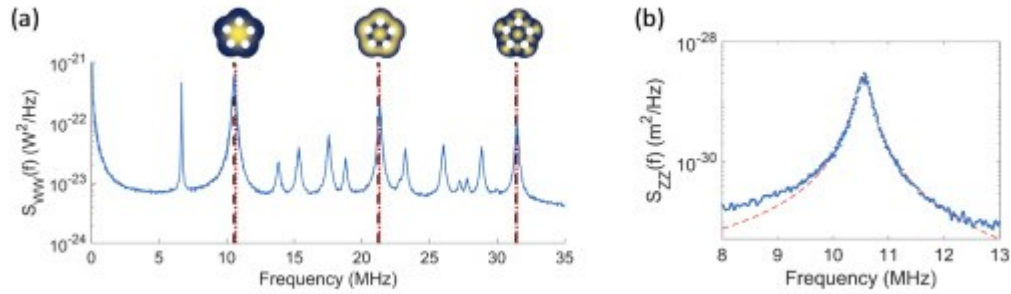


Figure 1.8 The thermomechanical noise spectrum of the first generation MIM device, adapted from [8]. (a), the full spectrum with the main mechanical vibrational modes of the embedded membrane (as simulated using COMSOL) shown next to their predicted resonant frequencies. (b) The fundamental membrane vibrational mode (blue) along with a Lorentzian fitting (red).

However, that previous work left significant room for improvement, owing mainly to the sub-optimal photolithography alignment and low value of the silicon nitride membrane stress that was achieved. Those shortcomings were addressed in this thesis project, through use of an improved lithographic tool and an optimized silicon nitride deposition recipe. The project also involved the implementation of an experimental apparatus to enable measurements under vacuum conditions, and subsequent attempts at the in-situ ‘vacuum-sealing’ of the membrane-in-the-middle optical cavities. Progress towards these goals is discussed in the later sections of this thesis.

## 1.6 Outline of the thesis

Following the brief background and overview provided in Chapter 1, Chapter 2 outlines some important theory related to the main thesis topics. Chapter 3 is a slight diversion from the main thesis topic outlined above, as it describes a study of *elliptical* buckled dome Fabry–Perot

microcavities. These cavities did not contain embedded mechanical oscillators but are of interest for quantum applications due to the fact they exhibit a large birefringence (i.e., a large and controllable polarization non-degeneracy for the optical modes). They were fabricated on the same wafer run as the MIM cavities described in the subsequent chapter. [17] Chapter 4 describes progress towards second-generation MIM cavity optomechanical devices. Chapter 5 provides a summary and discussion of the main results from the thesis work, as well as suggestions for future work.



## Chapter 2 -Theory

This chapter provides an overview of some theories relevant to the work described in later parts of the thesis. As introduced in Chapter 1, the thesis work is mainly concerned with the fabrication and study of cavity optomechanical devices. These devices can be analyzed as the interaction between two sub-systems: i.e., the optical sub-system, the mechanical subsystem, and their interaction [4]. The optical sub-system is a plano-concave Fabry-Perot optical microcavity with Si/SiO<sub>2</sub> and/or SiO<sub>2</sub>/Ta<sub>2</sub>O<sub>5</sub> quarter wave stacks (QWS) serving as the mirrors [14]. The primary mechanical sub-system is a circular, high-tensile-stressed plasma enhanced chemical vapor deposition (PECVD) silicon nitride membrane, although the buckled mirror of the plano-concave cavities also exhibits mechanical vibrational properties as detailed in Chapter 4. In addition to providing essential background theory related to these optical and mechanical sub-systems, a brief overview of the theory of elastic thin-film buckling is provided, since the plano-concave microcavities we study are formed by controlled formation of circular delamination buckles within a multi-layer thin-film stack.

Finally, some relevant theory pertinent to the interaction between the optical and mechanical sub-systems is provided, falling within the domain of so-called ‘cavity optomechanics’. A cavity optomechanical system is governed by the loss rate of the two sub-systems, and the coupling strength ( $g$ ) between them. Moreover, the free-standing membrane that serves as the primary mechanical sub-system exhibits mechanical vibration modes induced by thermal energy; this has been systematically studied by our group in previous work, using an approach labeled as ‘thermomechanical calibration’ [18].

# Selected topics from optical theory

## 2.1- Bragg Mirrors

Bragg mirrors are indispensable components for many applications in integrated optics, including the microcavities that are the subject of the current research. Within limits set by practical materials, they offer a customizable frequency range of flat response and high reflectance. A Bragg mirror is composed of a multi-layer stack of dielectric materials with alternating high and low refractive indices; typically, the thickness of each dielectric film is one-fourth of the wavelength in the given material, such that this type of reflector is also called a “Quarter Wave Stack” (QWS) [19]. The thickness of each layer, in order to satisfy the quarter-wave condition, is given as:

$$d_{1,2} = \frac{\lambda}{4n_{1,2}} \text{ (eq 2.1) ,}$$

where  $d_{1,2}$  denotes the layer thickness of material with refractive index  $n_{1,2}$  respectively. Within a stop band, electromagnetic waves reflected at different interfaces within the QWS will constructively interfere, thus functioning as a high reflectance mirror.

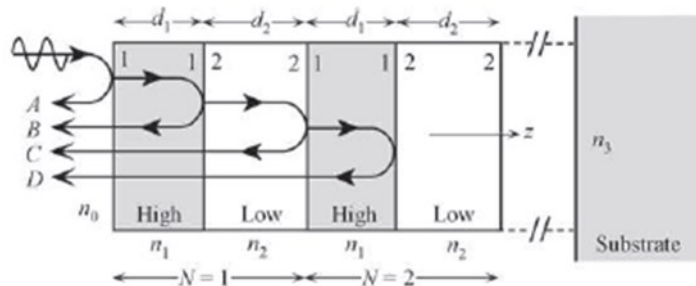


Figure 2.1 A diagram of a QWS, with alternating high-index layers and low-index layers. Each period of the quarter wave stack will increase the total reflectance. Adapted from [19].

The peak reflectance of a QWS (i.e., at the wavelength specified in Eq. 2.1) can be analytically expressed as:

$$R_{QWS} = \left( \left( 1 - \frac{n_0}{n_3} * \left( \frac{n_1}{n_2} \right)^{2N} \right) / \left( 1 + \frac{n_0}{n_3} * \left( \frac{n_1}{n_2} \right)^{2N} \right) \right)^2 \text{ (eq 2.2)},$$

where  $n_0, n_1, n_2, n_3$ , are the refractive indices of the incidence medium, the high-index dielectric material, the low-index material, and the substrate (i.e., exit) medium, respectively, and  $N$  is the number of alternating layers of high and low refractive index material. To increase the overall reflectance of a QWS, one can: 1. Increase the period ( $N$ ) of the QWS. 2. Use larger refractive index contrast material (i.e., Larger  $\frac{n_1}{n_2}$ ). However, when choosing materials for the QWS, absorption is another consideration; the material cannot be too lossy within the working wavelength range. The spectral width of the stopband, assuming a sufficiently large reflectance (i.e., large value of  $N$ ), is given as:

$$\Delta\lambda = \lambda_{Bragg} * \left( \frac{4}{\pi} \right) * \arcsin \left( \frac{|n_1 - n_2|}{n_1 + n_2} \right) \text{ (eq 2.3)},$$

where  $\lambda_{Bragg}$  is the center wavelength of the Bragg mirror (i.e., defined by eq. 2.1), and  $n_1, n_2$  are the refractive indices of the low- and high-index dielectric material, respectively. A typical spectral response of a Bragg mirror at normal incidence is shown below.

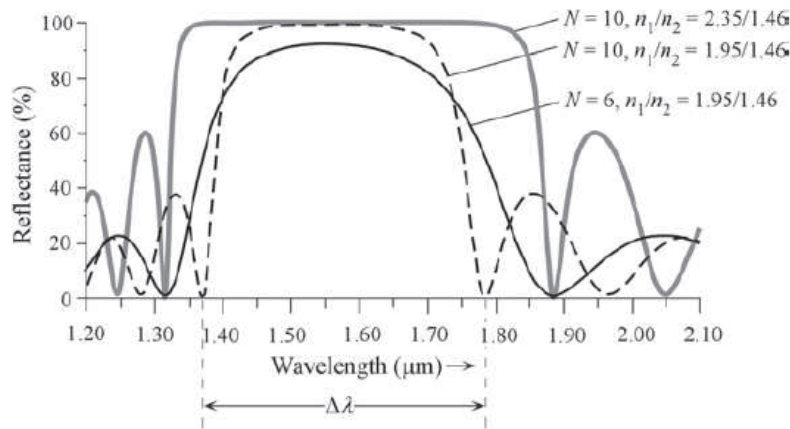


Figure 2.2 A reflectance versus wavelength plot of typical quarter wave stacks. For each curve, the period of QWS ( $N$ ), the low index material ( $n_2$ ), and the high index material ( $n_1$ ) is labelled.

Adapted from [19].

## 2.2 Fabry-Perot cavity/ Optical resonator

### 2.2.1 General definition

Optical cavities confine and store light at specific resonant frequencies [19], typically by incorporating one or more reflective components (i.e., mirrors). The Fabry-Perot cavity, sometimes called the Fabry-Perot Etalon, is an optical cavity with two parallel reflective mirrors on either side of a planar cavity region. At or near resonant frequencies, electromagnetic waves interfere constructively, and the fields form a standing wave inside the cavity. As shown in Fig 2.1, an infinite set (in principle, for ideal frequency-independent mirrors) of modes ( $f_m$ ) satisfy the standing wave condition, and those modes are integer multiples ( $m$ ) of the fundamental frequency. ( $f_1$ ) Moreover, the integer  $m$  is also called the longitudinal mode order [19].

$$v_m = m \left( \frac{c}{2nL} \right) = m * v_1 \text{ (eq 2.4),}$$

where  $m$  is the transverse mode order,  $c$  is the speed of light,  $\nu_1$  is frequency of the lowest-order mode,  $n$  is the refractive index of the cavity medium, and  $L$  is the cavity length. The transmitted intensity of light as a function of the wavenumber ( $k=2\pi n/\lambda_0$ ) is given as:

$$I_{cavity} = \frac{I_0}{(1-R)^2 + 4R \sin^2(kL)} \quad (eq\ 2.5),$$

, where  $I_0$  is the input intensity,  $R$  is the reflectance of both mirrors (assumed equal),  $k$  is the wavenumber ( $k = \frac{2n\pi}{\lambda_0}$ ), and  $L$  is the cavity length. Due to the finite lifetime of the electromagnetic wave inside an optical cavity, the spectral line shape of such a Fabry-Perot cavity is Lorentzian. Typical transmittance of longitudinal mode has been shown in Fig 2.3

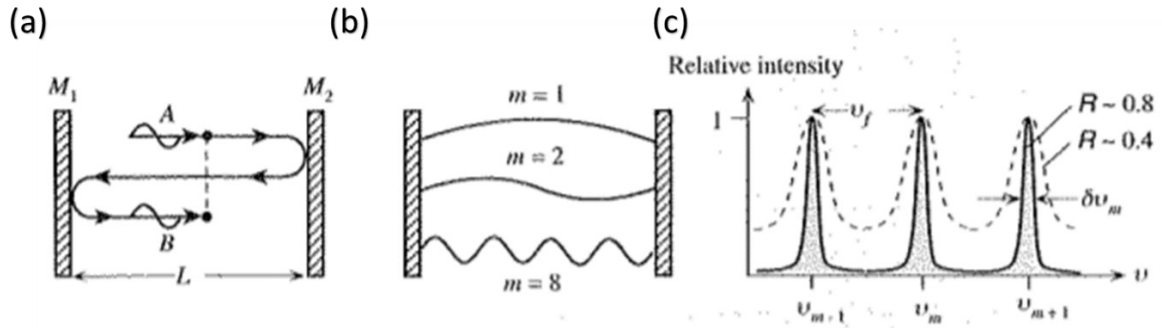


Figure 2.3 (a) A diagram showing light bouncing in an optical cavity. (b) Transverse modes of an optical cavity. (c) Line shape spectra of a planar Fabry-Perot optical cavity; each transmission line is well-described by a Lorentzian lineshape function. Adapted from [19].

### 2.2.2 Free spectral range

Free spectral range is defined as the wavelength or frequency difference between two adjacent longitudinal modes of the Fabry-Perot cavity [19], as denoted in Fig.2.3 (c). Moreover, this quantity can be calculated as:

$$\Delta\nu_{FSR} = \nu_1 = \left(\frac{c}{2nL}\right) \text{(eq 2.6)},$$

where  $\Delta\nu_{FSR}$  is the free spectral range measured in frequency,  $c$  is the speed of light,  $\nu_1$  is frequency of the first transverse mode,  $n$  is the refractive index of the cavity media, and  $L$  is the cavity length.

### 2.2.3 Finesse

Finesse is a very useful figure of merit for optical cavities [19]. For a Fabry-Perot cavity formed by two mirrors with identical reflectance  $R$ , the Finesse can be expressed as:

$$F = \frac{\pi\sqrt{R}}{1-R} \text{(eq 2.7)},$$

Finesse can also be defined as the free spectral range ( $\Delta\nu_{FSR}$ ) divided by the full width at half max ( $\Delta\nu_{FWHM}$ ) of one transverse mode.

$$F = \frac{\Delta\nu_{FSR}}{\Delta\nu_{FWHM}} \text{(eq 2.8)},$$

### 2.2.4 Quality factor

Quality factor ( $Q$ ) is a generalized concept applied to resonators of all kinds and is essentially the total energy stored in the resonator divided by the energy loss per cycle [19]. In other words, the quality factor quantifies the ability to temporally store energy inside a resonator. Practically speaking, the quality factor can be expressed as the center resonant frequency or wavelength ( $f_{resonant}, \lambda_{resonant}$ ) divided by the full width at half max linewidth ( $\Delta f_{FWHM}, \Delta\lambda_{FWHM}$ ) of the resonant peak:

$$Q = \frac{f_{resonating}}{\Delta f_{FWHM}} = \frac{\lambda_{resonating}}{\Delta\lambda_{FWHM}} \text{(eq 2.9)},$$

It is noteworthy that for the planar Fabry-Perot cavity discussed above, the quality factor ( $Q$ ) is related to the finesse ( $F$ ) and the longitudinal mode order ( $m$ ):

$$Q = m * F \text{ (eq 2.10).}$$

### 2.3 Gaussian beams

As shown in Fig 2.4, a plano-concave Fabry-Perot optical cavity supports modes with a Gaussian beam profile, and spherical mirror cavities of this type have historically been widely used in laser systems [20]. The planar mirror is located at the beam waist and the wavefront of the Gaussian-beam (in general Hermite-Gaussian or Laguerre-Gaussian) modes must match the curvature of the concave mirror at the position of the mirror.

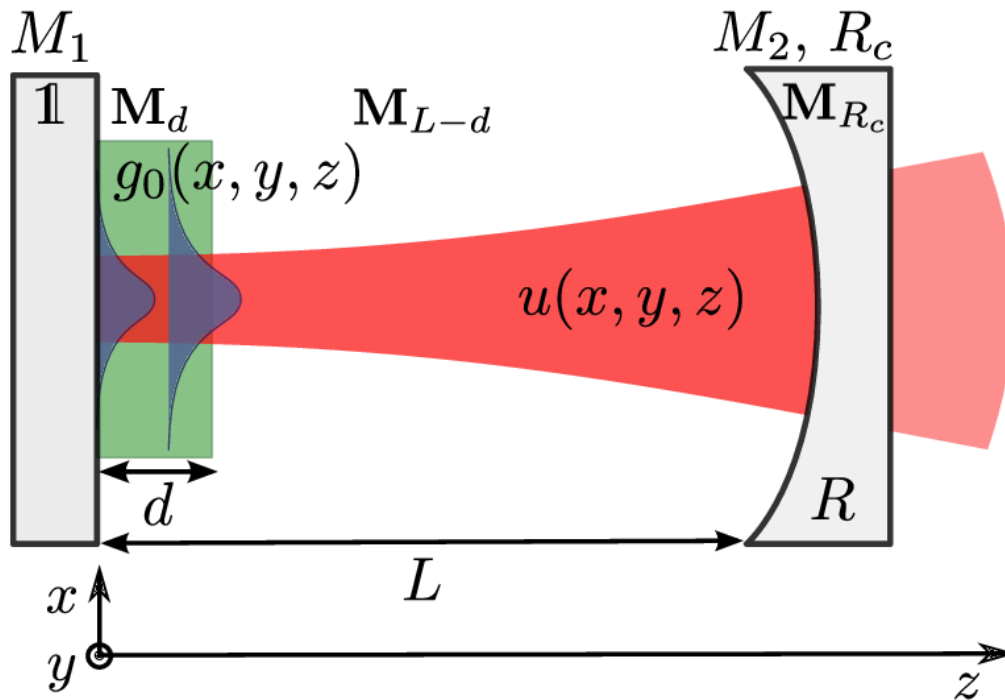


Figure 2.4 a diagram showing that a plano concave Fabry-Perot cavity will exhibit Gaussian modes, adapted from [21].

### 2.3.1 The general description of a Gaussian beam

Gaussian beams are solutions to the paraxial Helmholtz equation (PHE):

$$\frac{\partial^2 A}{\partial x^2} + \frac{\partial^2 A}{\partial y^2} + 2ik \frac{\partial A}{\partial z} = 0 \text{ (eq 2.11) ,}$$

where  $A(x, y, z)$  denotes the  $E$  or  $B$  field,  $x$ ,  $y$ , and  $z$  are cartesian coordinates, and  $k$  is the wavevector.

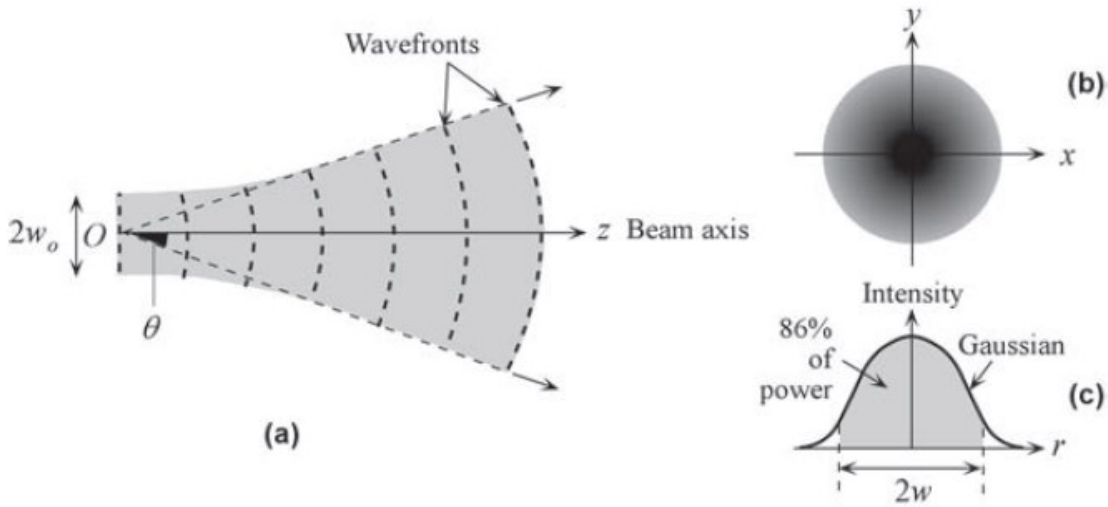


Figure 2.5 (a) the shape of a fundamental Gaussian beam along the axis of propagation. (b) the intensity shaded profile of a Gaussian beam (c) a cross-sectional intensity profile of the Gaussian beam. Adapted from [19].

The exact formula describing the Gaussian beam can be written [22]:

$$E(r, z) = E_0 \hat{P}(x, y) \left( \frac{w_0}{w(z)} \exp\left(\frac{-r^2}{w(z)^2}\right) \exp\left(-i\left(kz + k \frac{r^2}{2R(z)} - \psi(z)\right)\right) \right) \text{ (eq 2.12),}$$

$$z_R = \frac{\pi w_0^2 n}{\lambda} \text{ (eq 2.13),}$$



$$w(z) = w_0 \sqrt{1 + \left(\frac{z}{z_R}\right)^2} \text{ (eq 2.14),}$$

$$R(z) = z \left(1 + \left(\frac{z_R}{z}\right)^2\right) \text{ (eq 2.15),}$$

$$\psi(z) = \arctan\left(\frac{z}{z_R}\right) \text{ (eq 2.16).}$$

Here,  $r = \sqrt{x^2 + y^2}$  is the transverse distance from the optical axis,  $z$  is the longitudinal coordinate from the beam waist at  $z = 0$ ,  $\lambda$  is the vacuum wavelength of the electromagnetic field,  $k = 2\pi/\lambda$  is the wave vector of the electromagnetic field,  $n$  is the refractive index of the medium,  $z_R$  is called the Rayleigh range,  $E_0$  is the electrical field at the beam waist and on the optical axis,  $\hat{P}(x, y)$  is the polarization unit vector of the electric field,  $w_0$  is the beam waist (radius),  $w(z)$  characterizes the evolution of the beam waist,  $R(z)$  characterizes the evolution of the radius-of-curvature of the wavefront, and  $\psi(r)$  is called the Gouy Phase.

The Rayleigh range is the distance (along the  $z$  direction) from the beam waist to the point that the area of the beam has doubled, for a plano-concave cavity, the Rayleigh range is geometrically determined as [20]:

$$z_R = \sqrt{LR * \left(1 - \frac{L}{R}\right)} \text{ (eq 2.17),}$$

where  $L$  is the cavity length and  $R$  is the radius of curvature of the concave mirror.

### 2.3.2 Transverse higher-order Gaussian modes

Hermite polynomials and Laguerre polynomials are two sets of polynomial orthogonal basis functions which, when multiplied with the fundamental Gaussian beam, also satisfy the Paraxial

Helmholtz Equation. Both Hermite-Gaussian modes and Laguerre -Gaussian modes are schematically illustrated in Fig.2.6.

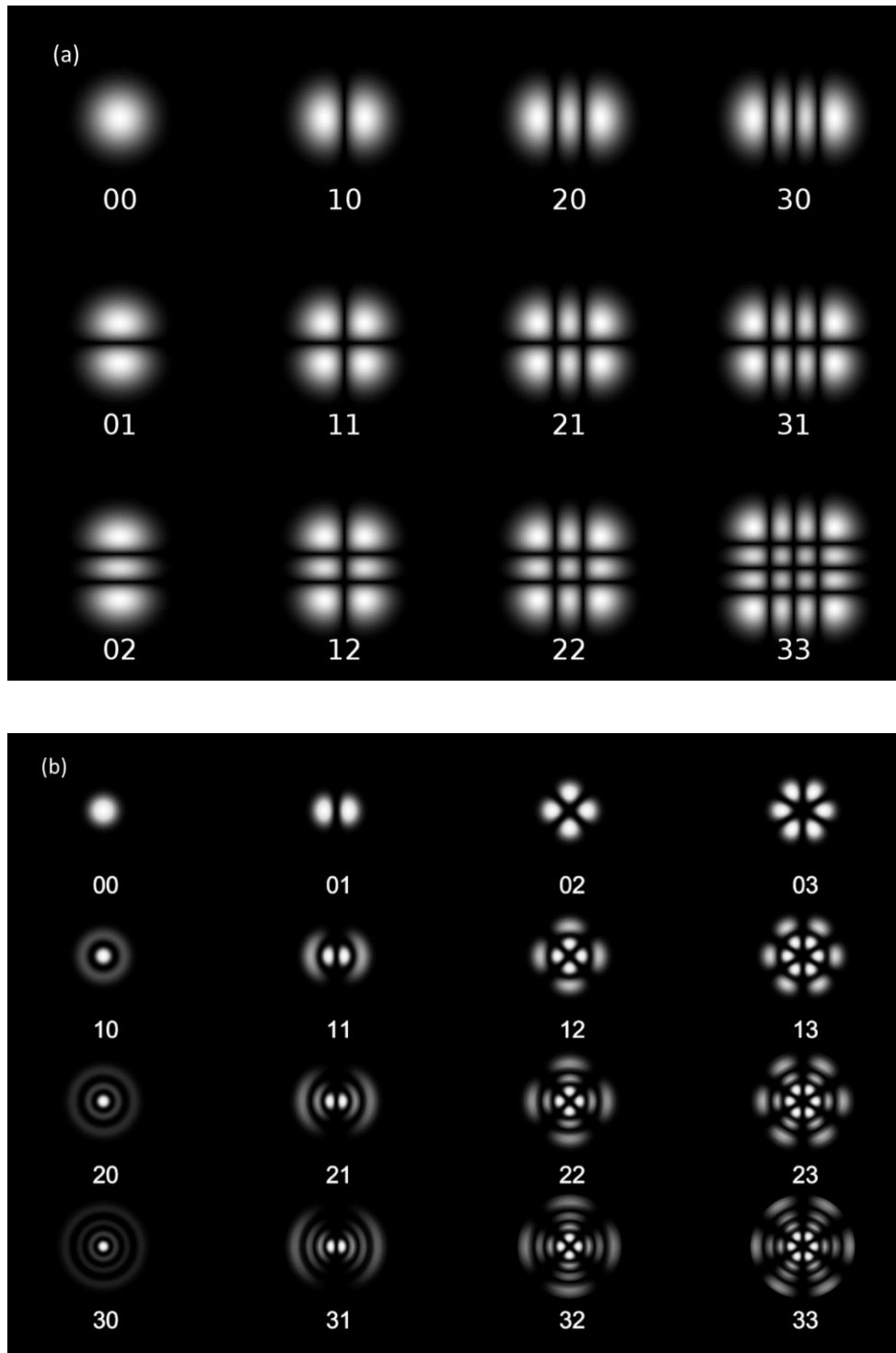


Figure 2.6 (a) The intensity profile of several Hermite-Gaussian modes. (b) The intensity profile of several Laguerre-Gaussian modes, adapted from [23] [24].

When the optical cavity shows a rectangular symmetry, it is natural to solve the Paraxial Helmholtz equation in cartesian coordinates and, thus, Hermite-Gaussian modes are typically observed. For a given mode order  $(m, n)$ , the Hermite Gaussian mode can be expressed:

$$\begin{aligned}
 E_{HG}(x, y, z, m, n) &= E_0 \hat{P}(x, y) \frac{w_0}{w(z)}, \\
 &* H_m \left( \sqrt{2} \frac{x}{w(z)} \right) \exp \left( \frac{-x^2}{w(z)^2} \right) * H_n \left( \sqrt{2} \frac{y}{w(z)} \right) \exp \left( \frac{-y^2}{w(z)^2} \right), \\
 &* \exp \left( -i \left( kz + k \frac{x^2 + y^2}{2R(z)} - (1 + m + n)\psi(z) \right) \right) \quad (eq \ 2.18),
 \end{aligned}$$

where  $m$  and  $n$  are the transverse mode order numbers of the Hermite Gaussian modes [25].

When the optical cavity shows a circular symmetry, it is natural to solve the Paraxial Helmholtz equation in cylindrical coordinates, and such cavities will tend to exhibit Laguerre-Gaussian modes. For a given mode order  $(m, n)$ , the Laguerre Gaussian mode can be described as:

$$\begin{aligned}
 E_{LG}(\rho, \varphi, z, m, n) &= C_{mn}^{LG} * E_0 \hat{P}(x, y) \frac{w_0}{w(z)} * \left( \frac{r\sqrt{2}}{w(z)} \right)^{abs(m)} * \exp \left( \frac{-r^2}{w(z)^2} \right) \\
 &* L_n^{abs(l)} \left( \frac{2r^2}{w(z)^2} \right) * \exp \left( -i \left( m\varphi + k \frac{r^2}{2R(z)} - \psi(z) \right) \right) \quad (eq \ 2.19),
 \end{aligned}$$

where  $\rho$ ,  $\varphi$ , and  $z$  are the cylindrical coordinates,  $C_{mn}^{LG}$  is the normalization constant for Laguerre Gaussian modes,  $m$  is the angular mode number,  $n$  is the radial mode number, and  $L_n^{abs(l)}\left(\frac{2r^2}{w(z)^2}\right)$  is the associated Laguerre polynomial [25].

## Mechanical properties of thin films and membranes

### 2.4 Buckling process

For thin films under compressive stress, which often arises due to the thermal expansion mismatch between the film(s) and the substrate, buckling delamination is a common failure mode [13]. The self-assembled microcavities developed by our group exploit such a buckling delamination process in order to fabricate ‘self-assembled’ plano-concave Fabry-Perot structures [14]. The critical stress ( $\sigma_c^*$ ) for the buckling of a circular delamination feature is given as [13] :

$$\sigma_c^* = 1.2235 \frac{E_1}{1-\nu_1^2} \left(\frac{h}{R}\right)^2 \quad (eq\ 2.20),$$

where  $E_1$  is Young’s modulus,  $\nu_1$  is the Poisson’s ratio,  $h$  is the film thickness, and  $R$  is the radius of the buckle.

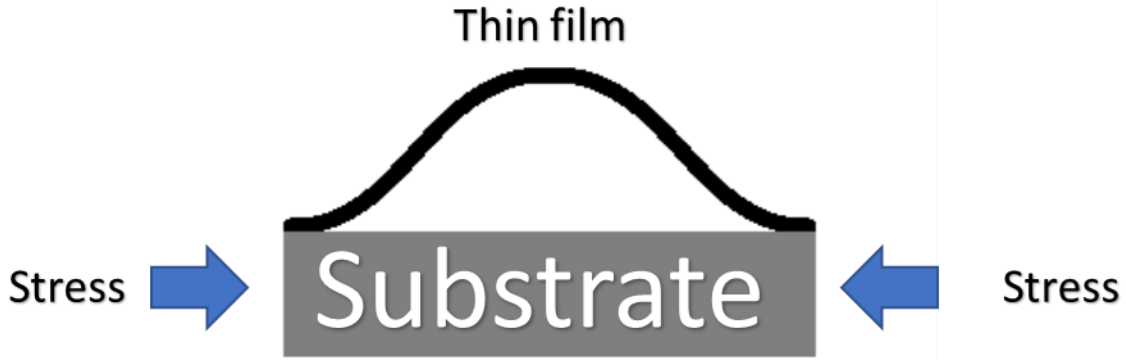


Figure 2.7 A diagram showing a buckling delamination process; when a thin film is under compressive stress, the film can delaminate and release some of its strain energy through buckling.

The corresponding buckling height ( $\delta$ ), assuming the buckling process is elastic (i.e., in the absence of plastic deformation of the film or substrate), can be predicted as [13]:

$$\delta = h * \frac{1}{0.2473(1+v_1)+0.2231(1-v_1^2)} \left( \frac{\sigma}{\sigma_c^*} - 1 \right)^{\frac{1}{2}} \quad (eq\ 2.21),$$

where  $\sigma$  is the stress of this film. Assuming an effective Poisson's ratio of 0.3 (typical for many thin film materials), the equation can be simplified as [14]:

$$\delta = h * 1.9 * \left( \frac{\sigma}{\sigma_c^*} - 1 \right)^{\frac{1}{2}} \quad (eq\ 2.22),$$

The buckle cross-section profile ( $w(r)$ ) can be written as [13]:

$$w(r) = [0.2871 + 0.7129J_0(\mu r)] * h \quad (eq\ 2.23),$$

where  $J_n(x)$  is the nth order of the Bessel's function, and  $\mu = 3.8317$ , which is the first nontrivial zero of  $J_1(x)$ .

## 2.5 Membrane resonators

Analogous to an optical resonator, a mechanical resonator stores mechanical energy at certain resonant frequencies. Nanomechanical resonators are small-scale versions of the macroscopic mechanical resonators familiar in everyday life, such as tuning forks or drumheads.

Nanomechanical resonators can have extremely low effective mass, high resonance frequencies (in the MHz or GHz range), and high quality factor [18]. Typical examples are nano-string [26] or nano-disk [27] resonators. Here, we are most interested in circular membrane mechanical resonators.

### 2.5.1 Basic differential equation for a mechanical resonator

For a circular membrane mechanical resonator, the equation of motion is [18]:

$$\frac{1}{s} \frac{\partial}{\partial s} \left( s \frac{\partial z}{\partial s} \right) + \frac{1}{s^2} \frac{\partial^2 z}{\partial \phi^2} - \frac{\rho}{\sigma} \frac{\partial^2 z}{\partial t^2} = 0 \quad (\text{eq 2.24}),$$

where  $z$  is the amplitude of the membrane vibration,  $s$  is the radial coordinate,  $\phi$  is the angular coordinate,  $\rho$  is the density of the resonator,  $\sigma$  is the tensile stress of the membrane, and  $t$  is the time. The solutions  $\psi(s, \phi)$  can be expressed [18]:

$$\psi_{mn}(s, \phi) = K_m \cos(m\phi) J_m \left( \frac{\alpha_{mn}s}{a} \right) \quad (\text{eq 2.25}),$$

where  $K_m$  is a normalization constant,  $J_m(x)$  is the Bessel function of the first kind with order  $m$ ,  $\alpha_{mn}$  is the  $n$ th zero of  $m$ th order of Bessel function of the first kind, and  $m, n$  are mode order numbers. The values of  $\alpha_{mn}$  are tabulated below:

$\alpha_{mn}$	n=1	n=2	n=3	n=4
m=0	2.4048	5.5201	8.6537	11.79

m=1	3.8317	7.0156	10.1735	13.3239
m=2	5.1536	8.4172	11.6198	14.7960
m=3	6.3802	9.7610	13.0152	16.2235

Table 2.1 the numerical value of nth zero of m-th Bessel function

The resonant frequencies are given by:

$$f_{mn} = \frac{1}{2\pi} \sqrt{\frac{\sigma}{\rho}} \frac{\alpha_{mn}}{a} \quad (\text{eq 2.29}),$$

where  $\rho$  is the density of the resonator,  $\sigma$  is the tensile stress of the membrane,  $a$  is the radius of the membrane.

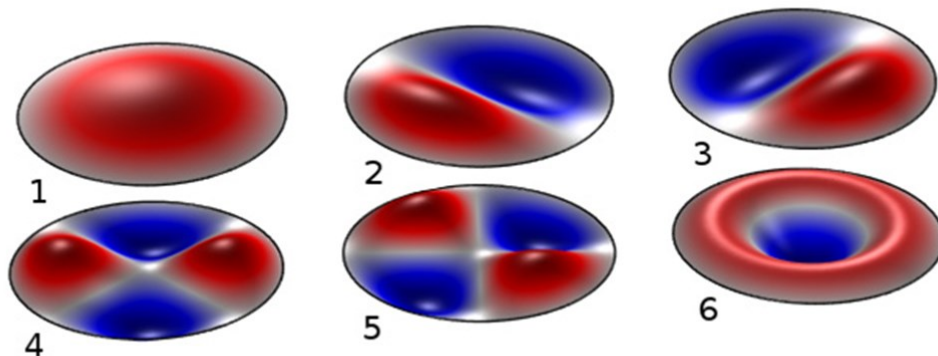


Figure 2.8 Different mode profiles of a circular vibrating membrane for modes  $(m,n) = (1,0)$ ;  $(1,1)$ ;  $(1,1)$ ;  $(1,2)$ ;  $(1,2)$ ; and  $(2,0)$ ; the red color and the blue color represent the positive and negative displacement of the membrane respectively, adapted from [28].

## 2.5.2 Quality factor of mechanical resonators

The quality factor of the mechanical system ( $Q_m$ ) is important, as it impacts the sensitivity in sensing application of optomechanical systems such as high bandwidth accelerometry [12]. For any resonator, the quality factor reflects the ability to temporally confine the energy, and can generally be defined as:

$$Q = 2\pi * \frac{\text{energy stored}}{\text{energy loss per cycle}} \text{ (eq 2.26),}$$

For a membrane mechanical resonator, the three primary mechanisms of energy loss are: “viscous or acoustic damping, clamping losses, and material losses” [8] [9]. The overall quality factor is the inverse sum of the Q factor due to different mechanisms of energy loss:

$$\frac{1}{Q_{tot}} = \frac{1}{Q_1} + \frac{1}{Q_2} + \frac{1}{Q_3} + \dots \text{ (eq 2.27),}$$

All these loss mechanisms and methods to mitigate the loss mechanisms will be discussed further below. Figure 2.9 shows common methods to address the primary loss mechanisms. Part (a) represent the measurement inside a vacuum environment to reduce viscous damping. Part (b) and (c) represent the trampoline and phononic crystal approaches to reduce the clamping loss.



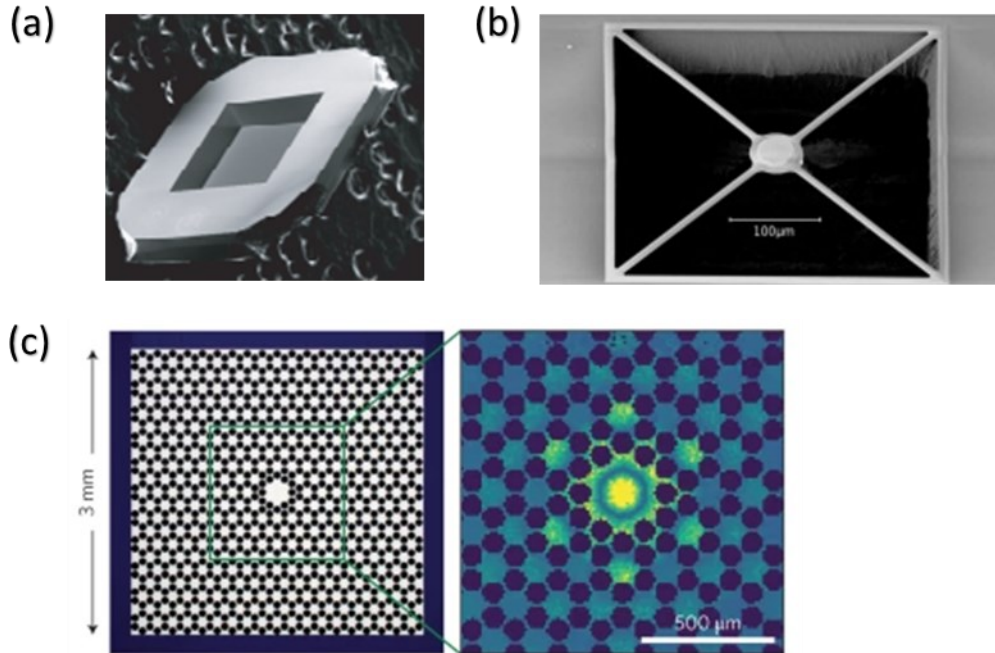


Figure 2.9 This is the same figure as Fig 1.4. (a), an SEM image of a SiN membrane resonator, adapted from [6]. (b) an optomechanical trampoline resonator, which minimizes the clamping loss by reducing physical contact between the central membrane ‘pad’ and the supporting frame, to reduce the elastic wave propagation, adapted from [29]. (c) A phononic crystal optomechanical resonator (a ‘soft clamping’ approach), which exploits forbidden bands for phonon propagation to limit the dissipation of thermal energy from the central ‘pad’ to the underlying substrate [11].

### 2.5.3 Viscous damping

A vibrating membrane resonator in a lab atmosphere will transfer some energy to air through both friction and radiation of pressure (acoustic) waves [9] [7] [30] This energy loss mechanism is significant in MEMS-scale devices, due to the large surface to volume ratio and small effective mass. At 1 atmosphere and 15°C, the air is modeled as a fluid with a viscosity constant ( $\mu$ ) of  $\sim 1.8 \times 10^{-5}$ . For a circular plate, the coefficient of damping force  $c_{air}$  is [30]:

$$c_{air} = \frac{3\pi}{2h^3} \mu a^4 \text{ (eq 2.28),}$$

where  $\mu$  is the viscosity constant,  $h$  is the thickness, and  $a$  is the radius of the plate.

Moreover, Southworth *et al.* proposed that the gas-damping limited quality factor can be calculated as [7]:

$$Q^{-1} = \frac{\rho_{gas} c_{gas}}{\rho_{res} t f} \text{ (eq 2.29),}$$

where  $\rho_{gas}$  and  $\rho_{res}$  are the density of the gas and resonator material, respectively,  $c_{gas}$  is the speed of sound,  $t$  is the thickness, and  $f$  is the resonant frequency.

#### 2.5.4 Clamping loss

For a vibrating membrane, energy is transferred (i.e., lost) to the supporting frame by the propagation of elastic waves through the boundaries of the membrane. Thus, the quality factor of the mechanical resonator is reduced. For the fundamental vibrational mode, the clamping-loss limited quality factor can be expressed as [31]:

$$Q_{01} = 0.029 \sqrt{\frac{\rho_r}{\rho_s} \left(\frac{E_s}{\sigma}\right)^3} \frac{D}{t} \text{ (eq 2.30) ,}$$

where  $\rho_r$  and  $\rho_s$  are the density of the membrane resonator and the substrate, respectively,  $E_s$  is Young's modulus of the substrate,  $\sigma$  is the stress of the resonator,  $D$  is the membrane diameter, and  $t$  is the thickness of the membrane resonator. Lastly, it is worth mentioning that, for the higher order modes, the clamping loss grows exponentially with the increase of the order of the Bessel function [31].

### 2.5.5 Optimization of the mechanical quality factor

This section discusses some methods to reduce the above-mentioned loss mechanisms. To reduce the loss of viscous damping, the membrane is usually placed in a vacuum and cryogenic environment [7]. To reduce the clamping loss, the mechanical resonator can employ a trampoline structure or a phononic crystal structure [29] [32]. As shown in Fig 2.9 (b), the trampoline structure reduces the elastic wave transmission into the substrate, by only keeping minimal supporting material [29]. A phononic crystal is a periodic structure that creates a forbidden band for phonons in a certain energy range, so that propagation of elastic waves from the central membrane pad to the substrate is reduced. An example structure is shown in Fig 2.9 (c); this approach has also been referred to as ‘soft clamping’ [32].

### 2.5.6 Dissipation dilution

The quality factor of a nanomechanical resonator increases due to its tensile stress, a phenomenon which is called dissipation dilution [33] [34]. The dilution factor is the quality factor ratio of a tensile-stressed film relative to that of the unstressed thin film [35]:

$$D_Q = \frac{Q}{Q_0} = 1 + \frac{W_{tensile}}{W_{elongation} + W_{bending}} \quad (eq\ 2.31),$$

where  $D_Q$  is the dilution factor,  $Q$  is the quality factor under tensile stress,  $Q_0$  is the intrinsic quality factor,  $W_{elongation}$  and  $W_{bending}$  are potential energy stored in the elongation and bending of the resonator, and  $W_{tensile}$  is the energy stored in a tensile stressed resonator. The intrinsic quality factor is defined as [35]:

$$Q_0 = 2\pi \frac{W_{elongation} + W_{bending}}{\Delta W_{elongation} + \Delta W_{bending}} \quad (eq\ 2.32),$$

where  $W_{elongation}$  and  $W_{bending}$  are potential energy stored in the elongation and bending of the resonator, and  $\Delta W_{elongation}$  and  $\Delta W_{bending}$  are the potential energy loss per cycle, respectively. [33] [35] The potential energy stored in elongation and bending of the resonator is lossy due to frictions, in comparison, the potential energy stored in tensile stress is lossless in the linear region. [33] [35] As a result, high-tensile stressed thin film resonators are desirable.

## 2.6 Thermomechanical calibration

At thermal equilibrium, the membrane nanomechanical resonator will preferentially vibrate at certain modal frequencies, driven by thermal energy. [4] In experiments, the displacement of the nanomechanical resonator is not typically analysed in the time domain but rather in the frequency domain. The outcome of such analysis techniques is a thermomechanical noise spectrum [4], as shown in Fig. 2.10.

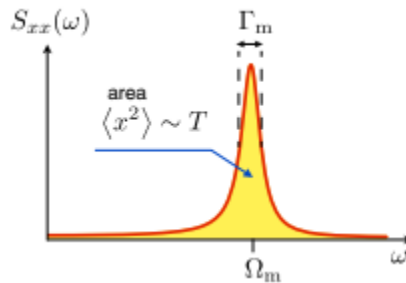


Figure 2.10 The thermomechanical noise spectrum of a mechanical oscillator at thermal equilibrium, adapted from [4].

The displacement of the nanomechanical resonator  $R(x, t)$  can be decomposed into mechanical vibration modes ( $R_n(x, t)$ ), where each mode has a spatial ( $r_n(x)$ ) and a temporal component ( $a_n(t)$ ) [18]:

$$R(x, t) = \sum_n R_n(x, t) = \sum_n r_n(x) a_n(t) \quad (\text{eq 2.33}).$$

Using a simple harmonic oscillator model and analyzing in the frequency domain, the ratio of the temporal response ( $A_n(\omega) = \mathcal{F}(a_n(t))$ ) to its driving force ( $\mathcal{F}(F(t))$ ) is defined as the mechanical susceptibility ( $\chi(\omega)$ ) [18]:

$$\chi(\omega) = \frac{\mathcal{F}(a_n(t))}{\mathcal{F}(F(t))} = \frac{1}{m_{eff,n}(\omega_n^2 - \omega^2 - i\omega\omega_n/Q_n)} \quad (\text{eq 2.34}),$$

where  $\omega_n$  is the natural frequency of mode  $n$ ,  $Q_n$  is the quality factor of mode  $n$ ,  $F(t)$  is the driving force, and  $m_{eff,n}$  is the effective mass of mode  $n$ . This equation is similar to its electrical counterpart, the electrical susceptibility from the Lorentzian Oscillator model [36]. Assuming the driving force is thermal vibration, it can be categorized as white noise. Thus, the input power spectral density ( $S_{FF}(\omega)$ ) is a constant. The output power spectral density ( $S_{ZZ}(\omega)$ ) is then:

$$S_{ZZ}(\omega) = |\chi(\omega)|^2 S_{FF}(\omega) = \frac{const}{m_{eff,n}^2 ((\omega_n^2 - \omega^2)^2 + (\frac{\omega\omega_n}{Q_n})^2)} \quad (\text{eq 2.35}),$$

The equipartition theorem states that in a thermal equilibrium system, energy in any available state should be equal. If we idealize the membranes as the superposition of 1D harmonic oscillators, the average potential energy  $\langle U \rangle$  in a given mode should be:

$$\langle U \rangle = \frac{1}{2} k_b T = \frac{1}{2} m_{eff,n} \omega_n^2 \langle a_n^2(t) \rangle \quad (\text{eq 2.37}),$$

The average potential energy is also equal to  $\int_0^\infty S_{ZZ}(\omega) d\omega$ , and evaluating the integral will give us:

$$const = \frac{4k_B T \omega_n m_{eff,n}}{Q_n} \quad (\text{eq 2.38}).$$

It follows that the output power spectral density can be written as:

$$S_{ZZ}(\omega) = |\chi(\omega)|^2 S_{FF}(\omega) = \frac{4k_B T \omega_n}{m_{eff,n} Q_n ((\omega_n^2 - \omega^2)^2 + (\frac{\omega \omega_n}{Q_n})^2)} \quad (eq. 2.39),$$

Including the noise floor of the detection system results in an overall spectral density:

$$S_{VV}(\omega) = S_0 + \alpha S_{ZZ}(\omega) \quad (eq. 2.40),$$

The parameter  $S_{VV}(\omega)$  is the complete lineshape of one mode in a thermomechanical noise spectrum, within the limits of the linear harmonic oscillator model. In practice, experimental results are usually a superposition of mechanical modes as discussed in Section 2.5.1.

## Selected topic on Optomechanical interactions

### 2.7 Cavity optomechanics

Cavity optomechanics is the study and exploitation of the interaction between optical and mechanical resonators, where this interaction is typically mediated by photon radiation pressure. Figures 1.2 and 1.3 schematically illustrate some typical optomechanical systems. Analogous to the C-QED model, the three most important quantities in a cavity optomechanical system are the coupling rate ( $g$ ) between the optics and mechanics, photon decay rate ( $\kappa$ ), and the mechanical damping/ phonon decay rate ( $\Gamma_m$ ). In a completely analogous fashion, the photon decay rate is equal to the optical resonant frequency divided by the optical quality factor, while the phonon decay rate is equal to the mechanical resonant frequency divided by the mechanical quality factor. (*i. e. Decay rate =  $\frac{Resonating Frequency}{Quality Factor}$* ). When  $g \gg \kappa, \Gamma_m$ , the optomechanical system is said to be in the strong-coupling regime. When  $g \leq \kappa, \Gamma_m$  the optomechanical system is said to be in the weak-coupling regime [4]. The optical subsystem and the mechanical subsystem has been discussed in Section 2.1-2.6, so the following section will focus on their interaction.

### 2.7.1 Theory

For a given optomechanical system, the optical frequency shift per displacement of the mechanical element is defined as [4]:

$$G = \frac{\partial\omega(x)}{\partial x} \text{ (eq 2.41).}$$

Such a coupling can be achieved by both a moving-mirror optomechanical system ( $v_m = m \left(\frac{c}{2nL}\right)$ ) and a membrane-in-the-middle (MIM) optomechanical system, amongst a myriad of others. For a membrane-in-the-middle (MIM) optomechanical system, the optical resonant frequency ( $\omega_{cav}$ ) is related to the position ( $x$ ) of the membrane as follows [6]:

$$\omega_{cav}(x) = \left(\frac{c}{L}\right) \cos^{-1} \left( |r_c| \cos \left( 4\pi \frac{x}{\lambda} \right) \right) \text{ (eq 2.42),}$$

where  $r_c$  is the field reflection coefficient of the membrane,  $c$  is the speed of light,  $L$  is the cavity length, and  $\lambda$  is the wavelength. If the membrane is sufficiently cooled in a vacuum environment, the membrane is modeled as a quantum oscillator at its ground state, and the level of fluctuation at the ground state is [4]:

$$x_{ZPF} = \sqrt{\frac{\hbar}{2m_{eff}\Omega_m}} \text{ (eq 2.43) ,}$$

where  $\hbar$  is the reduced Planck constant,  $m_{eff}$  is the effective mass of the membrane, and  $\Omega_m$  is the mechanical resonating frequency.

The single photon coupling efficiency ( $g_0$ ), an important parameter in many applications of cavity optomechanics [ref], can then be defined as:

$$g_0 = G * x_{ZPF} \text{ (eq 2.44)}$$

## 2.7.2 Tuned-to-slope measurements

As mentioned above, the location of the membrane has an effect on the resonant frequency (wavelength) of the optical cavity.

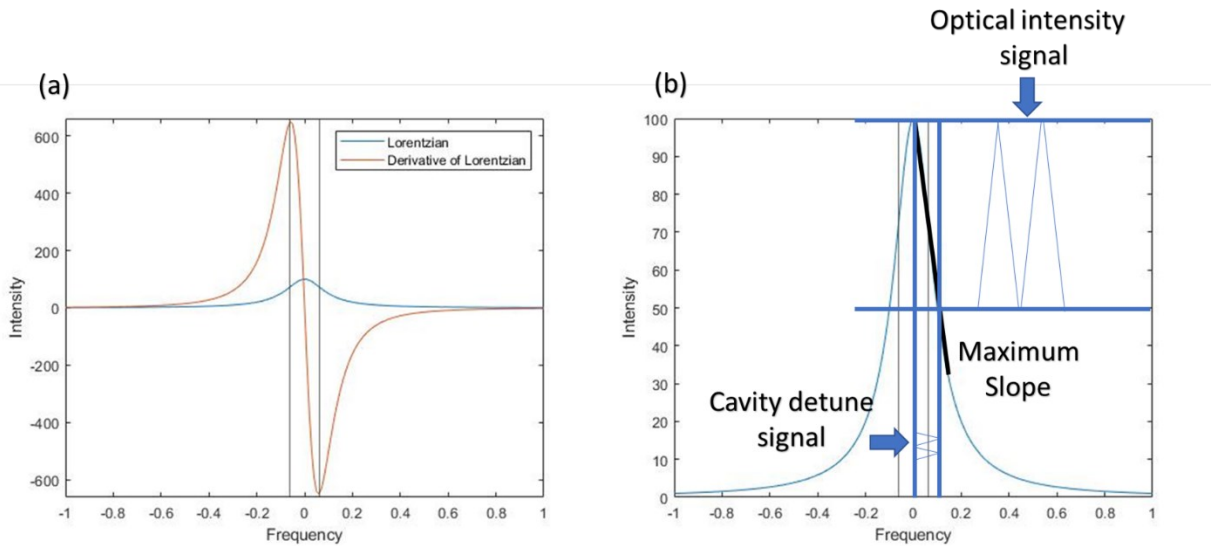


Figure 2.11 A diagram illustrating the tuned-to-slope technique. (a) The blue curve is the Lorentzian lineshape of the optical cavity resonance, the red curve is the derivative of the Lorentzian, and the two vertical lines are the maximum slope locations, which is also the optimal probe laser settings to maximize the signal-to-noise ratio. (b), A diagram showing the relationship between optical detuning and optical intensity change.

By employing a laser with a fixed wavelength as a probe laser, a power fluctuation in the time domain is observed, because the transmitted intensity depends on the difference between the laser frequency and the cavity resonance frequency. A changing cavity resonant frequency (i.e., due to vibrations of the membrane or end mirror) and a fixed laser frequency are equivalent to a fixed cavity resonating frequency and a changing laser frequency. To ensure maximum signal-to-noise ratio, the probe wavelength should be at the maximum slope of the Lorentzian response of



the optical cavity which corresponds to zeros of the second derivative of the Lorentzian function.

For a Lorentzian with center frequency ( $\omega_{cav}$ ) and linewidth (full-width-at-half-max (FWHM),

$\delta\omega_{FWHM}$ ), the maximum slope location is at:

$$\omega_{max} = \omega_{cav} \pm \frac{\sqrt{3}}{6} \delta\omega_{FWHM}^2 \text{ (eq 2.45).}$$

## Chapter 3 – Fabrication

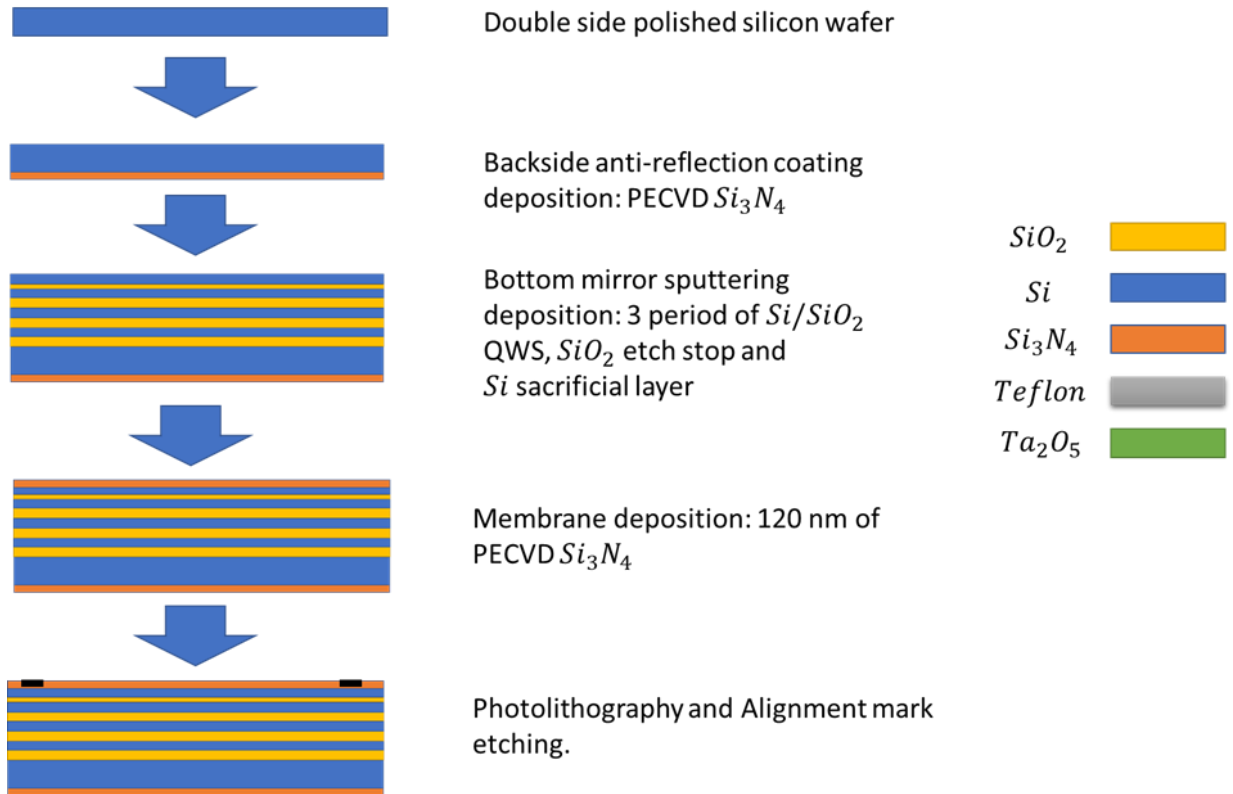
Microelectronics is an essential part in everyday life. The fabrication processes and techniques are thoroughly studied and developed. Common microelectronic fabrication techniques, including thin-film deposition, etching, pattern transfer, and thermal processes [37], were employed in the fabrication of the devices described in this thesis. Thin-film deposition techniques include physical vapor deposition (PVD) and chemical vapor deposition (CVD); these techniques add thin-films to a given structure. Pattern transfer refers to producing designed pattern, usually using a photolithography/etching technique or a lift-off technique. We take advantage of the nanofabrication facility (NanoFAB) at the University of Alberta to fabricate the MIM optomechanical microcavities as well as the elliptical optical cavities described later. Detailed parameters and recipes regarding fabrication are presented in appendix A.

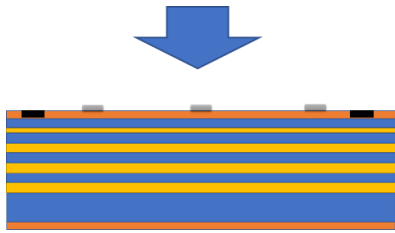
### 3.1 Fabrication of MIM devices

For the MIM optomechanical cavity, as discussed briefly in Chapter 1, the fabrication can be separated into 7 steps:

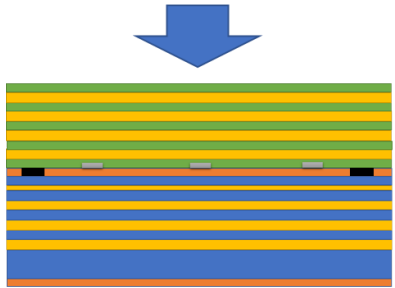
1. Back side anti-reflection coating deposition
2. Bottom mirror deposition (Sputtering of 3 period of  $Si/SiO_2$  QWS)
3. Low adhesion layer deposition and patterning (Oxford Estralus for teflon deposition, MLA 150 for alignment, and lift-off technique for pattern transfer)
4. Top mirror deposition (Sputtering of 4.5 period of  $Ta_2O_5/SiO_2$  QWS)
5. Buckle delamination self-assembly (Rapid thermal annealing)
6. Access hole etching (Cobra etching)
7. Membrane release by  $XeF_2$

Figure 3.1 graphically represent the process flow of the fabrication sequence, it is noteworthy that the thickness of each layer on the figure is not the actual scale. Also, this figure illustrates the device prior to vacuum sealing attempts, which are discussed in subsequent sections.

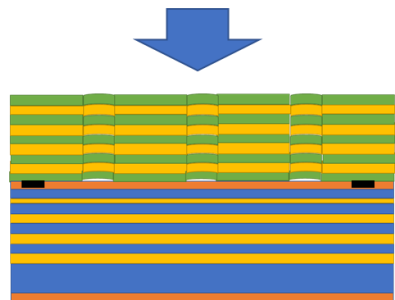




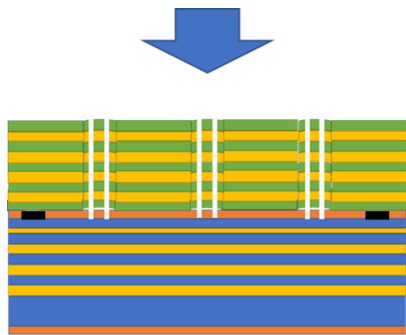
Deposition of low-adhesion fluorocarbon (Teflon), patterned by lift-off process



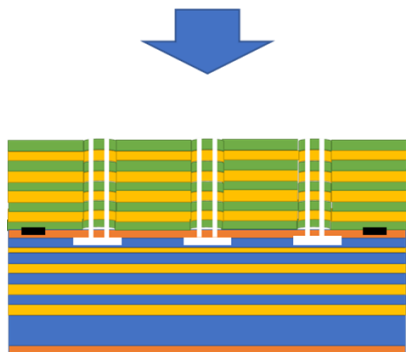
Top mirror sputtering deposition: 4.5 periods of  $SiO_2/Ta_2O_5$  QWS








Rapid thermal annealing to buckle delaminate the device, form optical cavities



Access holes etching



$XeF_2$  membrane release

$SiO_2$	
$Si$	
$Si_3N_4$	
Teflon	
$Ta_2O_5$	






$SiO_2$	
$Si$	
$Si_3N_4$	
Teflon	
$Ta_2O_5$	

Figure 3.1 The basic process flow of fabrication of the MIM optomechanical resonator

### **3.2 Vacuum sealing of MIM device**

In order to reduce the viscous damping effect, and inspired by work on capacitive micromachined ultrasound transducer (CMUT) devices [38] [39] [40] [41] and vacuum sealed MIM devices [42], we decided to explore the possibility for fabricating an integrated vacuum-sealed MIM optical microcavity. To seal the optical cavity after the membrane release step (see Figure 3.2 and Figure 3.3), a potentially straightforward approach is to deposit a (sufficiently thick) thin film under a vacuum environment. This sealing strategy is widely used in the MEMS industry and has been called MEMS ‘vacuum packaging’ [43] [44]. In our process development, various deposition methods were tried, including sputtering, Parylene deposition, and PECVD. An important concept to introduce is conformality [45], which means preserving the shape of the device that exists prior to the deposition. To achieve a good vacuum seal, a good sidewall coverage is required [46], which implies a need for more conformality. However, minimal material deposition on the embedded membrane is also desirable, which requires less conformality. In search of an appropriate compromise, various methods were tried as shown in Table 3.1, and each will be discussed in a later section.

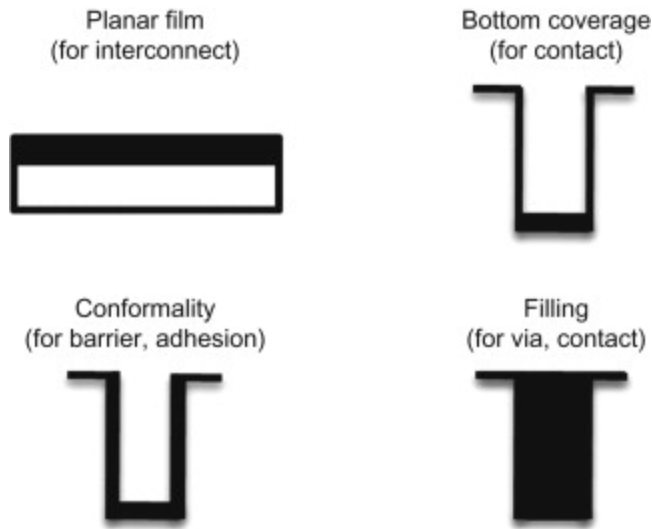


Figure 3.2 A diagram showing four common deposition applications in semiconductor devices, adapted from [45].

Furthermore, some important properties of the alternative sealing methods are tabulated and presented in Table 4.2. Note that each of these were attempts to seal portions of the same wafer and followed the basic MIM cavity fabrication process described in Appendix A.

Attempt	Sequence of films deposited after membrane release
1. Sputter Seal Attempt	Sputtering: 2-period of Si/SiO <sub>2</sub> QWS  Sputtering: 1 hour of SiO <sub>2</sub> deposition
2. Sputter Seal Attempt	Sputtering: 2-period of Si/SiO <sub>2</sub> QWS  Sputtering: 2 hours of SiO <sub>2</sub> deposition

3. Parylene Sealing Attempt [47]	<p>Sputtering: 2-period of Si/SiO<sub>2</sub> QWS</p> <p>Sputtering: 2 hours of SiO<sub>2</sub> deposition</p> <p>Parylene Deposition: 2 μm of parylene, followed the SOP provided by Nanofab</p>
4. PECVD Sealing Attempt	<p>PECVD: 2 microns of SiO<sub>2</sub></p> <p>Delaminated due to poor adhesion and /or stress mismatch</p> <p>Sputtering: 1-period of Si/SiO<sub>2</sub> QWS</p>

Table 3.1 a summary of the attempts to vacuum seal the dome optical cavity

Deposition method	Conformal?	Deposition/ vacuum sealing pressure
Sputtering (PVD)	No	3.8 mTorr
PECVD (CVD)	Yes	800 mTorr
Parylene (PVD) [47]	Yes	10 mTorr

Table 3.2 a summary of the vacuum sealing methods attempted

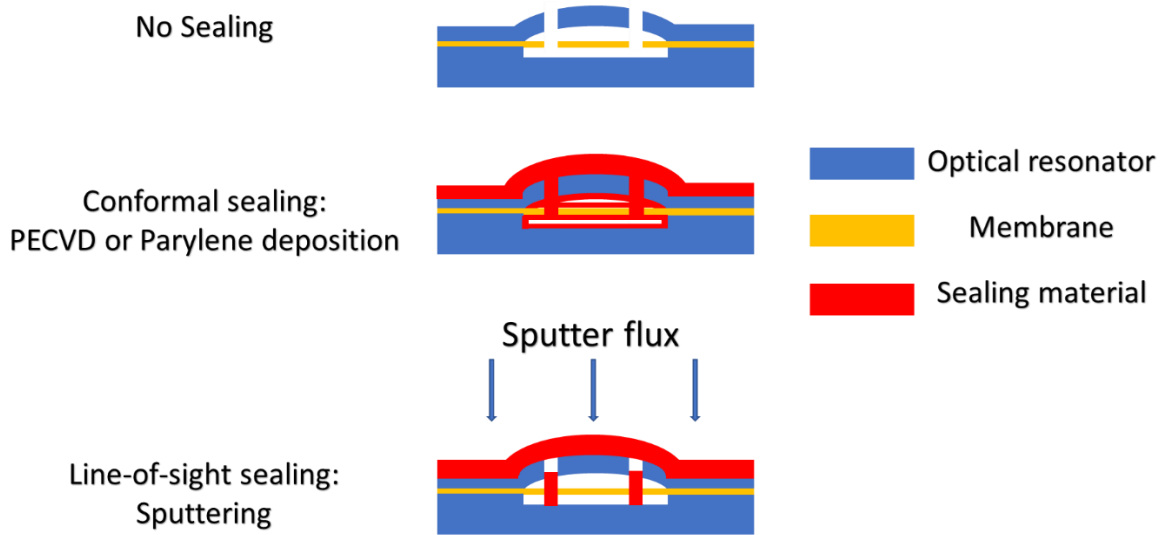


Figure 3.3 A diagram showing various sealing techniques. A conformal sealing technique will deposit on all surfaces, whereas a line-of-sight sealing will only deposit on the surfaces which can directly receive sputter flux.

Some typical photos of cavities after deposition of ‘sealing’ layers are presented below in Fig.3.4. For the cavities shown, the nominal base diameter is 50  $\mu\text{m}$ , and the nominal size of the access holes is 4  $\mu\text{m}$ .

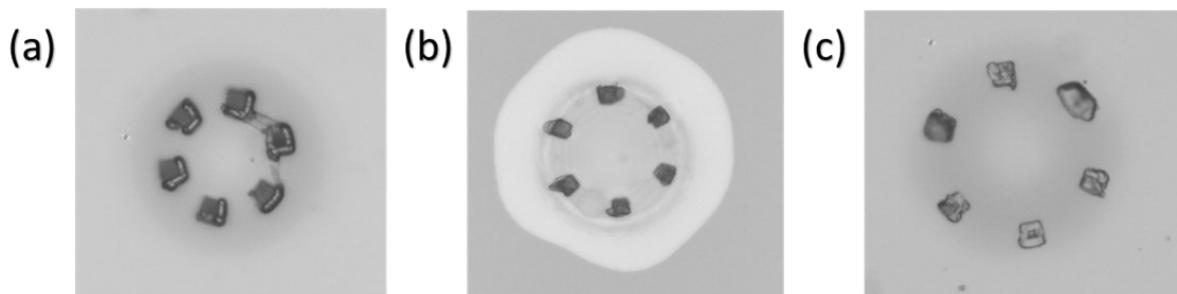


Figure 3.4 Photos showing the results of various trials aimed at vacuum sealing of the dome optical cavities. (a) 2 hours of  $\text{SiO}_2$  sputtering to vacuum seal the optical cavity, corresponding to trial 2. (b) the sample for which the upper layers delaminated after 2 microns PECVD



deposition; only the Si/SiO<sub>2</sub> layer got delaminated, which may have been due to poor adhesion resulting from lack of chip cleanliness prior to deposition of those layers. The outer ring corresponds to the membrane released by XeF<sub>2</sub>. (c) The delaminated sample from part (b) following sputtering of another Si/SiO<sub>2</sub> optical bilayer, which restored a sufficient optical quality factor to facilitate tuned-to-slope measurement, corresponding to trial 4.

### 3.3 Optimization of fabrication processes

As discussed in Chapter 1, an improved photolithographic alignment method, as well as an improved silicon nitride PECVD deposition recipe, was developed. The rest of the fabrication steps will be documented in Appendix A.

#### 3.3.1 Heidelberg MLA 150 maskless aligner

The Heidelberg MLA 150 maskless aligner system, a relatively recent addition to the U of A nanoFab, was used to improve alignment. Unlike the manual aligner, this system employs direct laser writing and automatic positioning. The optimal position accuracy 250 nm [48], whereas the manual mask aligner has a position accuracy of  $\sim 2 \mu\text{m}$ . Considering the dome diameter is 50  $\mu\text{m}$ , a 2  $\mu\text{m}$  misalignment is significant. Detailed processes and recipes are presented below:

1. Place the sample in the HMDS oven for promoting adhesion of the photoresist.
2. The photoresist used was AZ 1512, the dosage was 110mJ, and the laser wavelength was 405 nm.
3. The alignment mark position is manually input into the system, which is  $((x, y) = (\pm 27150, \pm 31000) \text{ microns})$ .
4. After exposure, soak the sample in AZ400K developer 40s and inspect. If not fully developed, put the sample back in the developer for another 20s.

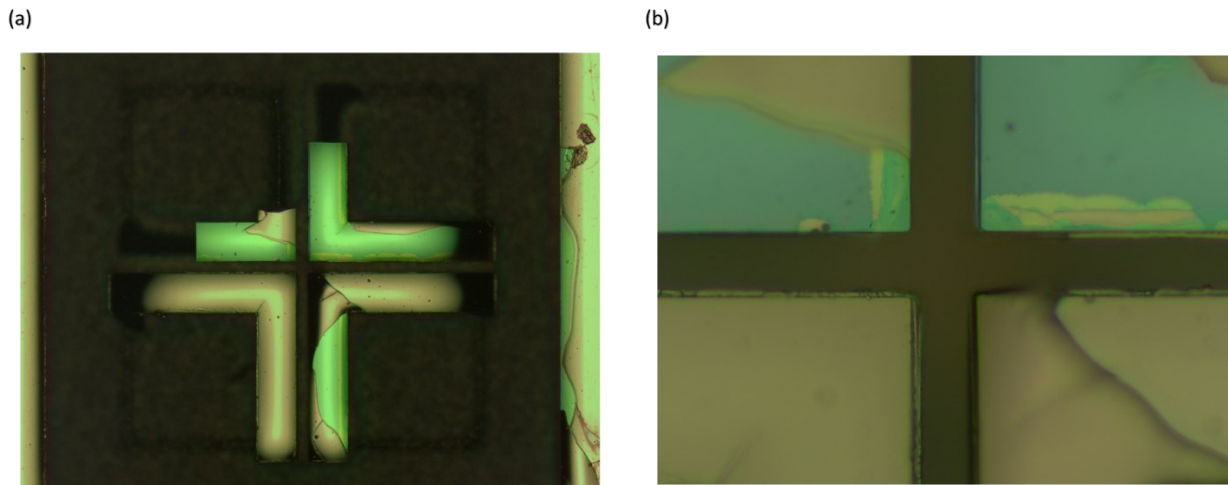


Figure 3.5 The photograph of the alignment mark after all fabrication processes. (a) 5 magnification (b) 50 magnification

When performing alignment on our 4-inch silicon wafers, the pneumatic alignment method is required, since the optical alignment method is only used for a smaller sample. Moreover, only 4 alignment marks are required, and the overall alignment will not benefit from additional alignment marks. When choosing photoresist in the MLA system menu, be aware not to choose large or extra-large depth of focus, this will result in under exposure due to blocking most of the laser beam.

### 3.3.2 PECVD recipe

The goal was to implement a 150 nm thick PECVD SiN high tensile-stressed membrane. Using the standard nitride recipe supplied by the nanoFab staff, the as-deposited thin film stress is typically highly compressive (700 MPa compressive). While annealing (see later section) causes this stress to become tensile, the value of tensile stress is typically below  $\sim 300$  MPa.

R. Arghavani et.al conduct research regarding various deposition parameter and the resultant tensile stress. [49] Thus, I modified the standard PECVD recipe guided by the table below:

<b>Variable ↑</b>	<b>Tensile Stress Response</b>	<b>Compressive Stress Response</b>
<b>Temperature</b>	<b>Increases</b>	<b>Increases</b>
<b>Pressure</b>	<b>Increases</b>	<b>Decreases</b>
<b>RF Power I</b>	<b>Increases</b>	<b>No Response</b>
<b>RF Power II</b>	<b>Decreases</b>	<b>Increases</b>
<b>Electrode Spacing</b>	<b>No Response</b>	<b>Decreases</b>
<b>Inert Gas Flow</b>	<b>No Response</b>	<b>Increases</b>
<b>Total SiH<sub>4</sub>+NH<sub>3</sub></b>	<b>Decreases</b>	<b>Decreases</b>
<b>Total SiH<sub>4</sub>/NH<sub>3</sub></b>	<b>Decreases</b>	<b>No Response</b>

Table 3.3 PECVD deposition parameters and their relationship with the thin film stress, adapted from [49]. RF power I and RF power II are the power of low RF (356 kHz) frequency and high (13.5 MHz) RF frequency respectively. [49]

According to Table 4.3, I developed and tested a new recipe: the deposition pressure was increased from 1000 mTorr to 1500 mTorr, RF power was increased from 80W to 120W, and substrate temperature was increased to 300°C from 325°C. Sequentially, the SiN thin films were annealed at 600 °C for 2 hours to bake out the hydrogen–silicon bonds [50] [51]. The exact details of the annealing recipe were as follows: ramp up from 450°C (the annealing system idle at 450 °C) to 600°C in 2 hours, hold at 600°C for 2 hours, and then ramp down to 450 °C for 2 hours. The measured film stress was ~250 MPa compressive and ~1GPa tensile before and after annealing, respectively.

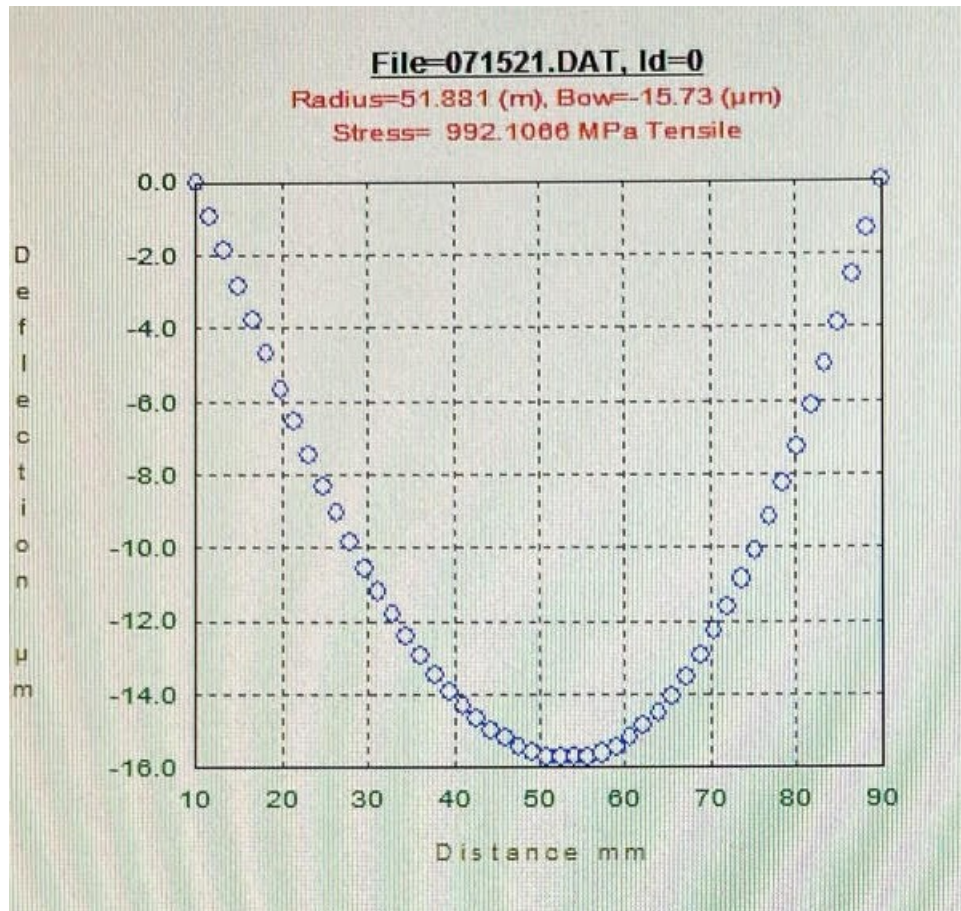


Figure 3.6 A thin film stress measurement of annealed PECVD nitride sample (~ 150 nm thick), deposited on a test (plain silicon) wafer, since the device wafer has additional layers that would affect the stress measurement. After the annealing process described in the main text, the stress is ~1 GPa tensile.

### 3.4 Fabrication of elliptical devices

The elliptical devices were realized using the same fabrication processes and on the same silicon wafer as the above-mentioned MIM devices. However, there is no need for the access holes etching and XeF2 membrane release treatment. For the sake of completeness and clarity, the fabrication of the elliptical optical cavity can be separated into 5 steps:

1. Back side anti-reflection coating deposition
2. Bottom mirror deposition (Sputtering of 3 period of  $Si/SiO_2$  QWS)
3. Low adhesion layer deposition and pattern (Oxford Estralus for teflon deposition, MLA 150 for alignment, and lift-off technique for pattern transfer)
4. Top mirror deposition (Sputtering of 4.5 period of  $Ta_2O_5/SiO_2$  QWS)
5. Buckle delamination self-assembly (Rapid thermal annealing)

# Chapter 4 - Monolithic elliptical dome Fabry-Perot microcavities exhibiting large birefringence

## 4.1 Background and Introduction

Fabry-Perot micro-cavities [52] [53] have been widely studied, with applications including sensing [54] and cavity quantum electrodynamics (cavity QED) [55]. These optical cavities are typically configured as either plano-concave or concave-concave spherical mirror resonators [53] [54]. Traditionally, CO<sub>2</sub> laser ablation [52] or focused ion beam (FIB) milling [54] have been employed to fabricate such optical cavities, but wafer-scale fabrication technologies are also under development [53]. Normally these cavities are hybrid-assembled by nano-scale alignment of separate mirrors deposited on either a substrate or a fiber end facet. In comparison, we have demonstrated a monolithic approach using a controlled thin-film self-assembly buckling process [15] [56], and reported preliminary efforts towards embedding mechanical resonators [8] and emitters [16] into this process.

Generally speaking, the micro-machined curved mirrors of these micro-cavities have a non-parabolic shape. Thus, both spherical aberration and astigmatism contribute to lifting the degeneracy for higher-order transverse modes of nominally identical order [57] [58]. Astigmatism of the curved mirrors can also introduce significant splitting of the polarization modes, which can be a complicating factor for many cavity QED applications [59]. Thus, optimizing the cylindrical symmetry of the curved mirrors is often a preferred goal for cavity QED systems [52], in order to minimize the non-degeneracy of polarization modes. Recently, however, highly birefringent cavities with intentionally introduced astigmatism have attracted significant interest [60] [61] [62] [63]. If polarization mode splitting can be intentionally and

controllably made to greatly exceed the cavity linewidth, this non-degeneracy might be exploited to increase the efficiency of single-photon emitters [64], to create new modalities of photon-phonon interactions in cavity optomechanics [65], and even to potentially exceed the traditional limits of Purcell enhancement [66].

Here, we study elliptical versions of the buckled-dome monolithic microcavities reported previously [15] [56]. The previously studied circularly symmetric cavities exhibit smoothly curved mirrors of predictable shape, and correspondingly ‘textbook’ manifestations of paraxial cavity modes. The elliptical cavities discussed here possess large astigmatism due to a significant difference in the effective mirror curvature along the major and minor axes. We show that the transverse mode structure is well described as two ‘nested’ families of elliptic Hermite-Gaussian beams, which can be predicted by applying a separation of variables approach to the scalar paraxial wave equation. Furthermore, we demonstrate a large splitting of the polarization eigenmodes ( $>25$  GHz for the fundamental cavity mode in the 1550 nm wavelength range), in good agreement with predictions from a vector-corrected paraxial resonator model [60].

## **4.2 Fabrication and Cavity Geometry**

The essential details of the fabrication process for these devices has been developed and studied extensively in previous works [8] [15] [16] [56]. In brief overview, a thin, fluorocarbon low adhesion layer is placed between an upper and lower sputtered Bragg mirror on top of a silicon substrate. Compressive stress in the upper mirror causes the upper mirror to delaminate and buckle along the regions with the patterned low adhesion layer. In past work, circular patterns were used to produce buckled upper mirrors exhibiting a smooth and predictable ‘spherical dome’ shape. Those samples typically exhibit Laguerre-Gaussian (LG) modes, as expected for a

plano-concave spherical mirror cavity possessing a high degree of axial symmetry [56]. In this work, we instead patterned elliptical delamination patterns and observed a similarly well-behaved buckle process with the center of the buckled film now forming the concave ellipsoid-like top mirror of a half-symmetric Fabry-Perot resonator (Fig. 3.1). The ellipsoidal character of the top mirror means it now has a different radius-of-curvature along each of its orthogonal axes. We fabricated elliptical domes of two different geometries, which we will refer to as ‘type A’ and ‘type B’ cavities, differing somewhat in terms of their major-to-minor axis ratios and their peak heights. Representative results for each type are described below and shown to be in good agreement with predictions of a vector-modified paraxial theory.

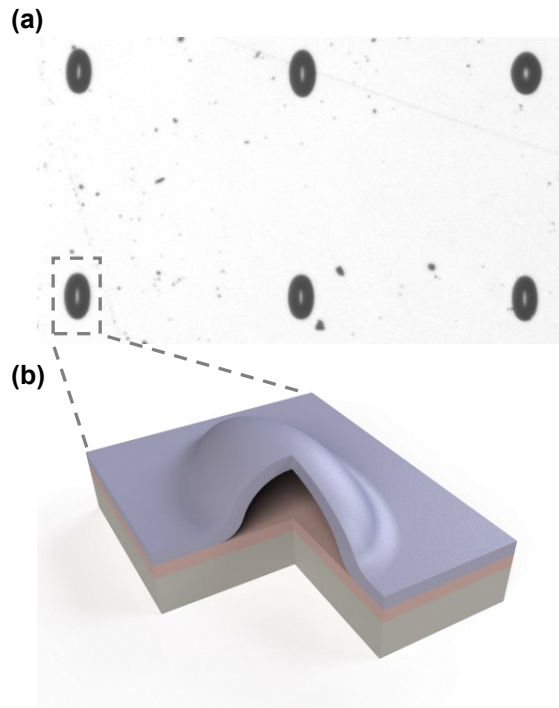


Figure 4.1 (a) Microscope image of an array of these devices. Note that 5 of the 6 devices shown are nominally identical, while the upper right device has a slightly less elongated profile. (b) Artist’s rendition of an elliptical dome Fabry-Perot microcavity, with an illustrated cutout showing the enclosed empty cavity.



Figure 4.2 shows microscope images of the two representative devices studied. The two device types studied here were the products of two different elliptical delamination patterns. For device type A, an elliptical pattern with major and minor radii of 33  $\mu\text{m}$  and 68  $\mu\text{m}$ , respectively, was used, while device type B was the result of a higher eccentricity elliptical pattern with major and minor radii of 25  $\mu\text{m}$  and 125  $\mu\text{m}$ , respectively. Owing to the self-assembly nature of their formation, the shape of the elliptical buckled structures is remarkably smooth and elliptically symmetric throughout the entire height. The geometry of each device was studied through optical profilometer (ZYGO) scans, as shown in Fig 3.2. In the case of the type A device, the base of the dome is well approximated by an ellipse with a major and minor radius of 35  $\mu\text{m}$  and 70  $\mu\text{m}$ , respectively, and with a peak buckle height of approximately 4.6  $\mu\text{m}$ . For the type B device, the corresponding radii are 35  $\mu\text{m}$  and 60  $\mu\text{m}$ , with a peak height of 5.5  $\mu\text{m}$ . Figures 2(c-d) show slices of the profilometer scan at the device center along the x and y directions. Circles were fit to the section of each curve within  $\pm 10$   $\mu\text{m}$  of the peak in order to approximate the effective radii-of-curvature for the optical modes, which reside mainly near the center of the cavity (see below). For convenience, we align the elliptical minor axis to the experimental horizontal x-axis, and the elliptical major axis to the experimental vertical y-axis. We obtained good fits (black dashed lines on Fig. 2(c-d)) for  $R_{x,A} = 74$   $\mu\text{m}$ ,  $R_{y,A} = 365$   $\mu\text{m}$ , and  $R_{x,B} = 58$   $\mu\text{m}$ ,  $R_{y,B} = 574$   $\mu\text{m}$ , for the radius-of-curvature for the type A and B cavities respectively.

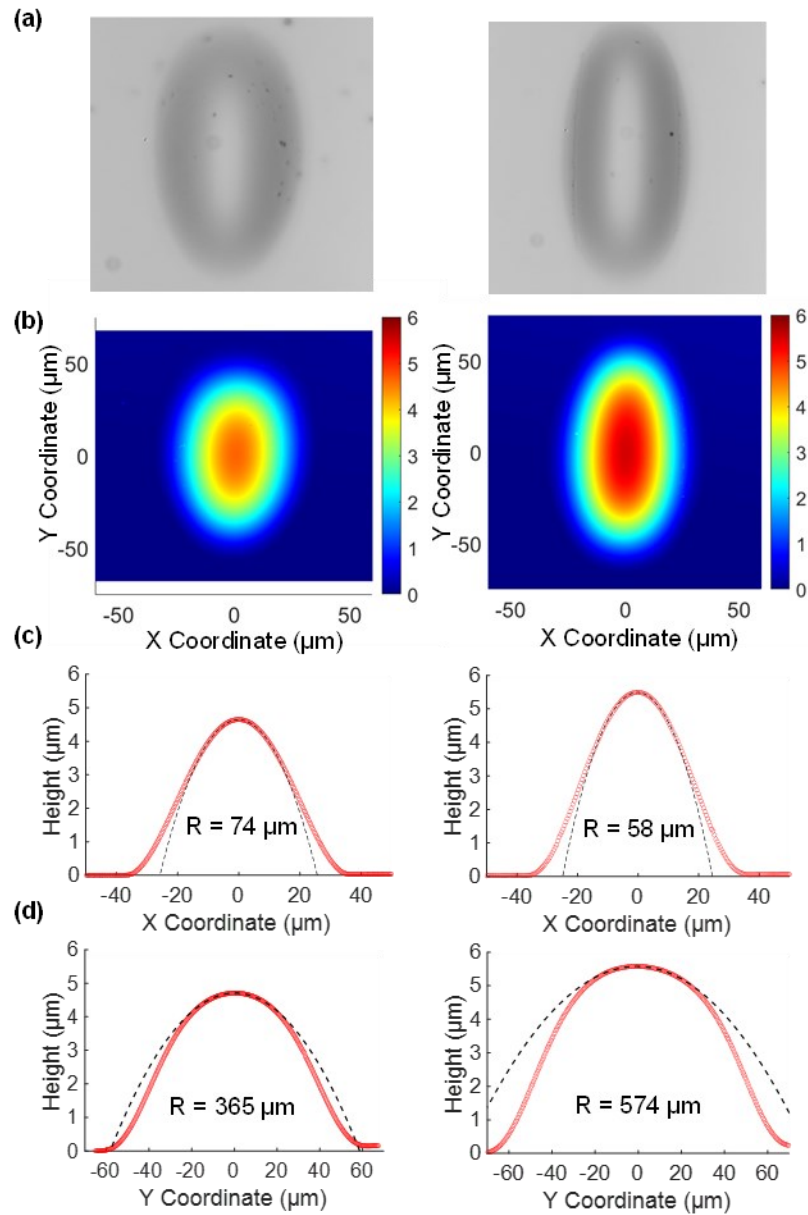


Figure 4.2 Representative data for elliptical cavity devices labeled as type A (left column) and type B (right column). (a) Microscope images of the device, (b) 3D profilometer (ZYGO) scans of the devices, (c) Cross-sectional profile plot along the minor axis direction from the profilometer scan in part b. (red circles), along with a circle fit to the section of the curve spanning  $\pm 10 \mu\text{m}$  from the peak (black dashed.) (d) As in part c., but for the major axis of each device.

The devices studied here have an  $\text{SiO}_2/\text{a-Si}$  bottom mirror and an  $\text{a-Si/SiO}_2/\text{Ta}_2\text{O}_5$  top mirror. They are from a wafer that was primarily designed for a study of integrated membrane devices as in Ref. [8], where the bottom mirror was terminated by a 200 nm layer of a-Si (which functions as a sacrificial layer for the membrane-embedded cavities) and a 150 nm layer of SiN. In the elliptical cavities studied here, these additional layers simply reduce the finesse. From transfer-matrix simulations we estimate a top and bottom mirror reflectance of  $R_T \sim 0.990$  and  $R_B \sim 0.985$  respectively, resulting in a predicted finesse  $F \sim 250$  which is in good agreement with the optical measurements described in Section 4. With improved mirror design, it is possible to achieve much higher finesse in these buckled cavities [15] [56]. Some implications of a higher finesse for exploiting the birefringence of the elliptical dome cavities are discussed in Section 3.5.

### **4.3 Plano-ellipsoidal cavities – theoretical treatment**

#### **4.3.1 Elliptical Gaussian beam modes**

Due to their elliptical shape, in particular the ellipsoid profile of their upper mirror, these cavities support optical modes that differ from those of a cylindrically symmetric cavity. Light confined within these astigmatic cavities will take the form of an ‘elliptical Gaussian beam’ (EGB) (also known as an astigmatic Gaussian beam.) The fundamental EGB is the elliptical analogy to a canonical (circular) Gaussian beam and can be described as a straightforward combination of two independent Gaussian beams along the x and y axes, each with its own set of independent Gaussian beam parameters [67]. By following a similar procedure, an expression for the higher-order elliptical Hermite-Gaussian (HG) modes can be obtained in the usual way from the paraxial wave equation, but by using a separation-of-variables approach to account for a unique

wavefront curvature along each axis. Following this approach, the electric field profiles of the  $TEM_{l,m}$  elliptical HG modes at position  $z$  along the beam axis can be expressed:

$$E_{l,m}(x, y, z) = E_0 \left( \frac{w_{0x}w_{0y}}{w_x(z)w_y(z)} \right)^{1/2} H_l \left( \frac{\sqrt{2}x}{w_x(z)} \right) H_m \left( \frac{\sqrt{2}y}{w_y(z)} \right) \exp \left( -ikz + i\eta_x(z) \left( l + \frac{1}{2} \right) + i\eta_y(z) \left( m + \frac{1}{2} \right) - \frac{i\pi x^2}{\lambda_0 q_x(z)} - \frac{i\pi y^2}{\lambda_0 q_y(z)} \right), \text{ (eq 4.1)}$$

$$q_j(z) = z - z_j + i \frac{\pi w_{0j}^2}{\lambda_0},$$

$$w_j^2(z) = w_{0j}^2 \left[ 1 + \left( \frac{\lambda_0(z-z_j)}{\pi w_{0j}^2} \right)^2 \right],$$

$$\eta_j(z) = \tan^{-1} \left( \frac{\lambda_0(z-z_j)}{\pi w_{0j}^2} \right), \text{ (eq. 4.1)}$$

where  $l / m$ ,  $w_{0x}/w_{0y}$ , and  $z_x/z_y$  are the respective x / y mode numbers, beam waists, and waist locations. By extension, we allow  $g_j(z)$ ,  $w_j(z)$ , and  $\eta_j(z)$  for  $j = x, y$  to be, respectively, the astigmatic complex beam parameter, spot size, and Gouy phase. Finally,  $H_n$  represents the Hermite polynomial of degree  $n$ ,  $\lambda_0$  is the free space wavelength of the beam, and  $E_0$  an arbitrary field amplitude in units of V/m. As expected, in the case of symmetry between x and y, eq 4.1 reduces to the well-known canonical expressions for the HG modes of an axially symmetric cavity.

Equation 4.1 predicts a set of modes very similar to traditional HG modes, but with an elliptical character. Selected mode-field intensity profiles are plotted at  $z=0$  in Fig. 3.3 for mode indices  $l$  and  $m$  as labeled in the figure and using beam waist values which are representative of the devices studied in this paper (e.g., for device type B:  $w_{0x} = 3.1 \mu\text{m}$ ,  $w_{0y} = 5.3 \mu\text{m}$ , at  $\lambda_0 = 1600 \text{ nm}$ .) Also shown in the figure are the corresponding experimentally observed mode-field intensity profiles (see Section 3.4) for each case, with the optics nominally focused at the beam

waist location near the surface of the planar mirror. There is good agreement between observation and theory for both the fundamental mode and higher order modes. Modes of a higher order have a larger spatial extent and are not as well characterized by a single fixed radius-of-curvature along each axis. Thus, a greater discrepancy between the simple paraxial theory and experiment is expected for the higher-order modes, since spherical aberrations impact the experimental beam profiles.

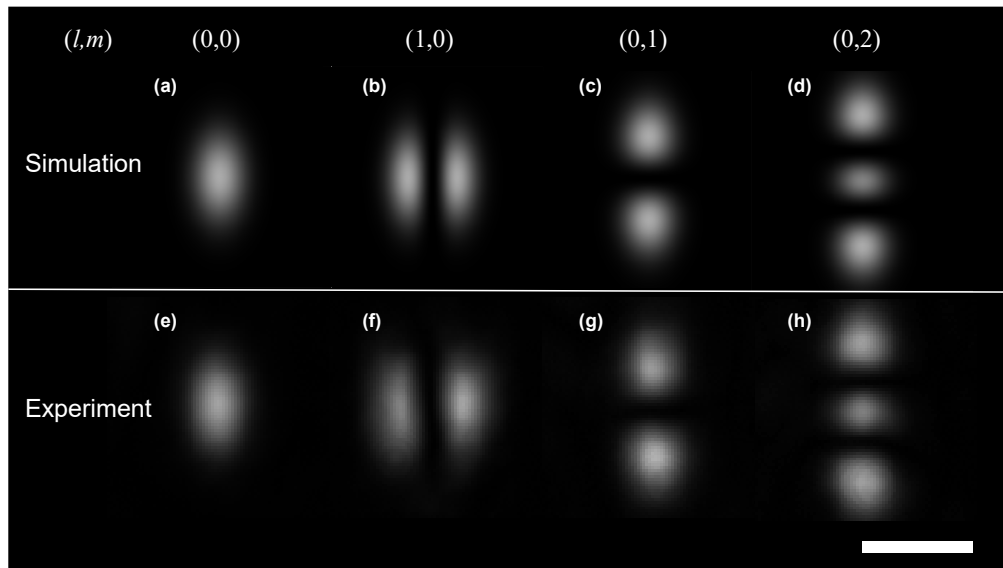


Figure 4.3 Predicted (a-d) and observed (e-h) mode-field intensity profiles for selected low-order modes of the type B cavity. Simulations are plotted at  $z = z_x = z_y = 0$ , and experimental measurements are taken focused at nominally the same point (the surface of the planar mirror.)

All plots in the figure are on a common scale (scale bar: 10  $\mu\text{m}$ ).

Since the spatial transverse confinement is axis-dependent, it follows that the spacing between transverse modes of a given longitudinal mode order will also be axis-dependent. Following a similar approximation of separability in  $x$  and  $y$ , the respective contributions to the Gouy phase factor of mode number  $l$  and  $m$  can be treated separately. This leads to a

straightforward expression for the transverse mode separation (i.e., relative to the longitudinal  $TEM_{0,0}$  elliptical HG mode) [68]:

$$\Delta\lambda_T = \frac{\lambda_0^2}{2\pi L} \left( \Delta l \cdot \cos^{-1} \sqrt{1 - \frac{L}{R_x}} + \Delta m \cdot \cos^{-1} \sqrt{1 - \frac{L}{R_y}} \right) \text{ (Eq 4.2)}$$

As was the case with Eq. (3.1), for symmetry in x and y this expression reduces to the well-known result for axially symmetric HG beams. We note that eq 4.2 is only correct to first order; for small radii-of-curvature, corrections are required to account for higher order effects such as spherical aberrations [57].

### 4.3.2 Vector modifications – mode birefringence

Typically, when the paraxial wave equation is used to predict the resonant wavelength of a curved-mirror cavity, polarization is not taken into account. However, when one considers a vector analysis of polarized light within the cavity, polarization-dependent corrections to the modal solutions arise. Consequently, since in these cavities there are different radii-of-curvature along the x and y axes, we can expect a polarization-dependent splitting to occur in the resonant wavelength of each of the elliptical HG modes predicted by the paraxial theory above. In other words, the cavity modes exhibit polarization non-degeneracy (birefringence). Uphoff et al. [60] provided polarization-dependent corrections to the paraxial theory for the  $TEM_{0,0}$  mode, for cavities very similar to those studied here. The wavelength splitting  $\Delta\lambda_p$  of the  $TEM_{0,0}$  mode between two different orthogonal polarizations in a plano-ellipsoidal cavity (to first order in  $\lambda_0/2\pi w_0$ ) is given by [60]:

$$\Delta\lambda_P = \frac{\lambda_0^3}{8\pi^2 L} \cdot \frac{R_y - R_x}{R_y R_x} \text{ (Eq. 4.3)}$$

where  $\lambda_0$  is the wavelength of operation in free space,  $L$  is the length of the cavity, and  $R_x$  and  $R_y$  are the radii-of-curvature along the minor and major axes of the ellipsoidal mirror. Equation 4.3 is valid provided that  $\Delta\lambda_p \gg \lambda_0^6/64\pi^4 w_0^4 L$ , which is easily within the regime of the cavities studied here. As discussed in the introduction, a large polarization-mode splitting can be exploited for many emerging applications. Often, it is necessary that the polarization modes are well resolved [64], i.e., that  $\Delta\lambda_p/\delta\lambda \gg 1$ , where  $\delta\lambda$  is the full-width at half-maximum (FWHM) of the modes. Cavity linewidth can be predicted according to  $\delta\lambda = \lambda_0/nF$  where  $n$  is the longitudinal mode order of the cavity resonance, and  $F$  is the cavity finesse. The degree of mode splitting can then be predicted by taking the ratio of the two expressions:

$$\frac{\Delta\lambda_p}{\delta\lambda} \approx \frac{\lambda_0 F}{4\pi^2} \cdot \frac{R_y - R_x}{R_y R_x} \text{ (Eq. 4.4)}$$

#### 4.4 Plano-ellipsoidal microcavities – experimental

The experimental optical properties of the domes were studied in a transmission setup similar to that described in our past work [56] [8] [16], with an additional capability for polarization control. Light is sent from a linearly polarized fiber-coupled tunable laser (Santec TSL-710) through SMF-28 fiber into a manual 3-paddle fiber polarization controller (Thorlabs FPC560) wound in a  $\lambda/2 - \lambda/4 - \lambda/2$  configuration. The light was coupled to a cavity from underneath (i.e. through the anti-reflection-coated, double-side-polished silicon substrate) using a reflective collimator (Thorlabs RC-08) and an objective lens. Light was collected from the top (i.e. the buckled mirror side) of the cavity using an infinity-corrected 50x objective lens (Zeiss Epiplan-NEOFLUAR) and sent through a rotatable broadband polarizer (Meadowlark Optics.) The light was then focused by a tube lens onto a near-infrared camera (Raptor Ninox 640 NX1.7-VS-CL-640) for both mode imaging and spectral scans. Polarization-dependent scans were

obtained by orienting the collection-side polarizer along the x/y axis of the domes and then adjusting the input polarization and coupling conditions. Specifically, the paddle polarizer was adjusted until the output signal was maximized for a given orientation of the output polarizer, and then the process was repeated for the orthogonal polarization condition.

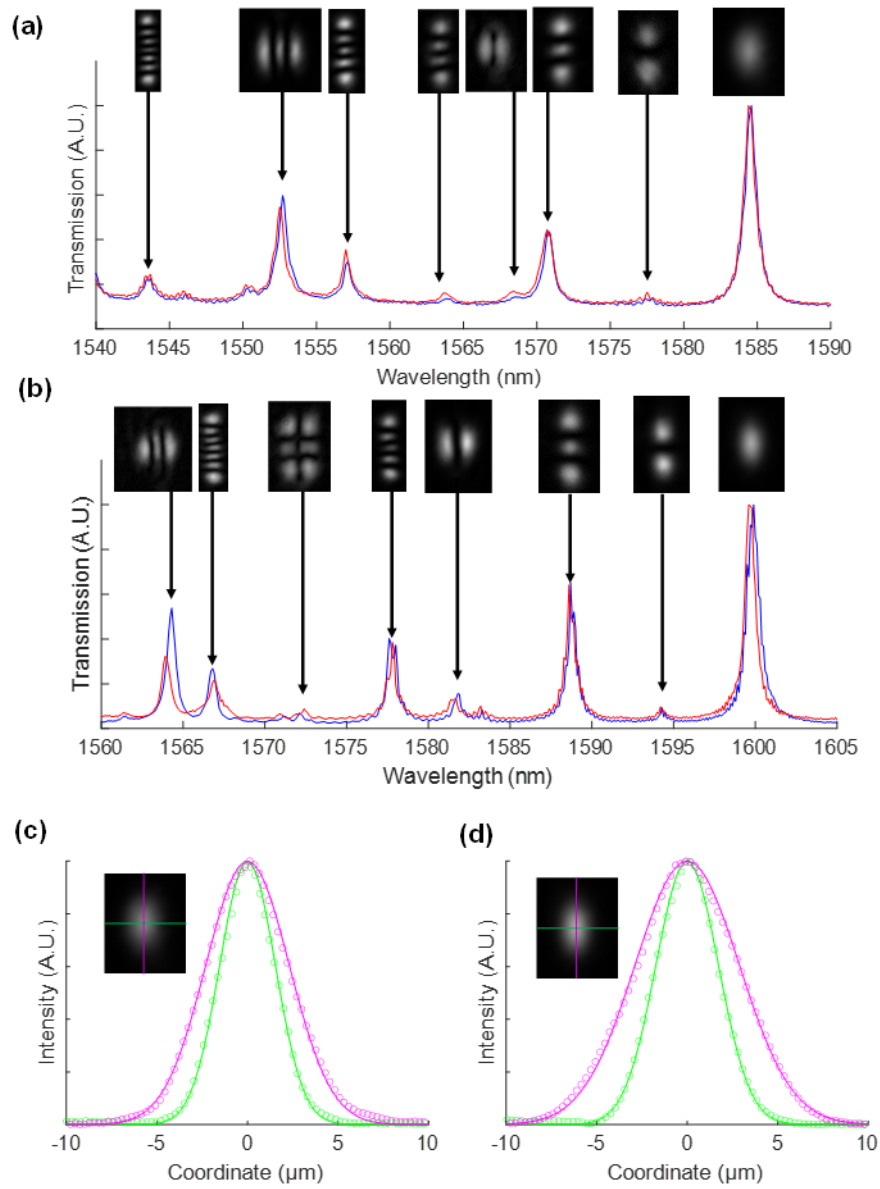




Figure 4.4 Spectral scans and mode-field intensity plots are shown for (a) device type A, and (b) device type B. In each case, the red curve corresponds to the input polarization aligned to minor (x) axis, while the blue curve corresponds to the input polarization aligned to the major (y) axis.

Profile plots for (c) device type A and (d) device type B along x and y (green and magenta circles) of the fundamental  $TEM_{0,0}$  elliptical mode (inset,) along with Gaussian fits. (solid lines.)

Figures 4.4 (a) and (b) show spectral scans for device types A and B respectively, and for the input laser polarization aligned to either the minor or major axis of the elliptical cavity. The inset photographs show various observed mode-field intensity patterns, with their corresponding resonant frequencies indicated by the arrows. The birefringent character of the cavities is clearly discerned in these plots, which reveal small but distinct polarization non-degeneracy for each of the resonant modes. The mode-field patterns are characteristic of elliptical HG modes, with a complete lifting of the usual  $m + l$  degeneracies expected in an axially symmetric cavity. Using the effective radii-of-curvatures from Table 4.1, we found that the frequencies of the transverse modes are only approximately predicted by eq 4.2. The best fit (not shown) was obtained for the case of the  $TEM_{0,m}$  modes in device type B, which possessed the largest radius-of-curvature along the y-axis. As mentioned above, corrections to eq 4.2, in order to account for spherical aberrations and non-paraxial effects, are likely required as the radii-of-curvature gets smaller. Nevertheless, the wavelengths of the transverse modes are roughly predicted by eq 4.2, and the experimentally observed modes appear in the order predicted by the simple paraxial theory.

Turning our focus to the  $TEM_{0,0}$  mode, we find that it is well predicted by paraxial theory for both devices. For example, using the estimated peak height and radii-of-curvature from Fig. 3.2, we can predict the waist size  $w_{0j} = (\lambda_0/\pi)^{0.5}(L/R_j)^{0.25}$  [15], with  $j = x, y$ . For device type

A,  $w_{0x} \sim 3.0 \mu\text{m}$  and  $w_{0y} \sim 4.5 \mu\text{m}$  are predicted, in excellent agreement with the Gaussian fits to the experimental profiles in Fig. 3.4(c), which yields  $w_{0x} \sim 3 \mu\text{m}$  and  $w_{0y} \sim 4.6 \mu\text{m}$ . Similar agreement is achieved for device B, with waists of  $w_{0x} \sim 3.0 \mu\text{m}$  and  $w_{0y} \sim 5.3 \mu\text{m}$  predicted, compared to the fitted beam waists of  $w_{0x} \sim 3.1 \mu\text{m}$  and  $w_{0y} \sim 5.3 \mu\text{m}$ .

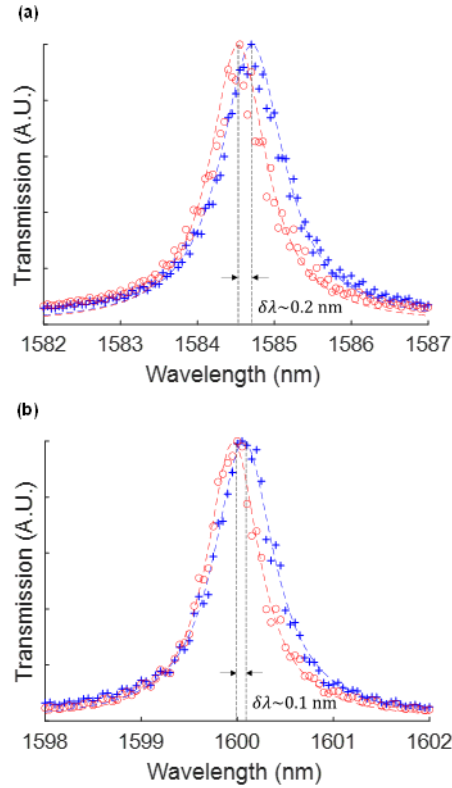


Figure 4.5 Spectral scans near the resonant wavelength of the  $TEM_{0,0}$  mode for: (a) the type A device and (b) the type B device for polarization along the minor (x) axis (red open circles) or along the major (y) axis (blue crosses). Lorentzian fits to the experimental data points are shown as a dashed line in each case.

Property	Type <i>A</i>	Type <i>B</i>
<i>X</i> -polarized center wavelength (nm) - $\lambda_{0x}$	1584.7	1600.1
<i>X</i> -polarized FWHM (nm) - $\delta\lambda_x$	1.0	0.8
<i>Y</i> -polarized center wavelength (nm) - $\lambda_{0y}$	1584.5	1600.0
<i>Y</i> -polarized FWHM (nm) - $\delta\lambda_y$	0.9	1.1
Measured polarization eigenmode splitting (nm) - $\Delta\lambda_p$	0.2	0.1
Predicted polarization eigenmode splitting (nm) - $\Delta\lambda_p$	0.2	0.1

Table 4.1 Estimates of the polarization splitting for the fundamental cavity mode

In order to further assess the birefringent properties of the cavities, spectral scans near the resonant wavelength of the  $TEM_{0,0}$  modes were obtained using a small step size (0.05 nm) setting of the tunable laser, and for input polarization aligned along the minor or major axis of the ellipse. Typical results are shown in Fig. 3.5, with the spectra for each polarization fit to a Lorentzian lineshape of center wavelength  $\lambda_0$  and linewidth  $\delta\lambda$ . Table 1 gives the results of these fits, with coefficient of determination  $R^2 > 0.95$  estimated in each case. The observed polarization eigenmode splitting of  $\Delta\lambda_p \sim 0.2$  nm ( $\sim 25$  GHz) for device type A and  $\Delta\lambda_p \sim 0.1$  nm ( $\sim 12$  GHz) for device B are both in excellent agreement with the predictions of Eq. (3.3). Note also that measured linewidths are in accordance with the predicted linewidths (i.e., on the order of  $\sim 1$  nm) using the estimated finesse ( $F \sim 250$ ) discussed in Section 2, and the measured heights of the cavities. A similar splitting was observed on multiple devices of each type, with the polarization splitting still reasonable within measurement error and variations in the precise geometry of each buckled structure. Finally, note that the splitting-to-linewidth ratio is  $\Delta\lambda_p/\delta\lambda \sim 0.2$  and  $\Delta\lambda_p/\delta\lambda \sim 0.1$  for devices type A and B, respectively. These devices do not satisfy the linewidth-resolved condition discussed in Section 3, primarily because of their low finesse.

As mentioned above, the longer-range spectral scans in Fig 3.4(a) and (b) revealed that birefringence is also present for the higher-order elliptical HG modes. However, Eq 4.3 is strictly valid for the TEM 0,0 mode only, so we have made no effort to quantify the splitting of the higher-order modes. Finally, it is worth mentioning that we did not observe polarization-dependent changes in the experimental mode-field intensity profiles. Although not conclusive, this does suggest that any such differences in mode-field profile associated with polarization are beneath the resolution of our imaging setup.

#### **4.5 Discussion and conclusions**

We have demonstrated large astigmatism and birefringence in plano-ellipsoidal microcavities fabricated using a thin-film buckling process. The experimentally observed modes were shown to be well predicted by paraxial beam theory using a separation-of-variables approach. Furthermore, the polarization eigenmode splitting of the fundamental cavity modes was shown to be in good agreement with predictions from a vector-modified paraxial theory. It is worth mentioning that an even larger birefringence and astigmatism might be possible with refinement of the fabrication processes. For example, it might be feasible to reduce the effective radius-of-curvature along the short axis through patterning of higher aspect ratio elliptical patterns in the low-adhesion layer. Moreover, the height of the buckled top mirror can be increased for a given feature size by buckling a thinner multilayer stack (i.e., fewer periods in the top mirror at the time of buckling). We have shown in past work [8] that additional periods can be added post-buckling in order to increase the reflectance and cavity finesse. A taller buckle height for a similar base profile would force the top mirror to bend even more, resulting in a shorter radius-of-curvature and an even greater eigenmode polarization splitting as predicted by eq 4.3

While the splitting is not linewidth resolved (i.e.,  $\Delta\lambda_p/\delta\lambda > 1$  is not achieved) for the particular devices studied here, this is mainly due to their low finesse ( $F \sim 250$ ). We have routinely achieved a much higher finesse ( $F > 2000$ ) in previous work [15] [56] [8] [16], which would result in  $\Delta\lambda_p/\delta\lambda \sim 1$  for the elliptical geometries described. Furthermore, the finesse of our buckled cavities to date has been primarily limited by residual absorption in our sputtered thin films. We anticipate that improved thin film processes should allow for  $F > 10^4$  [69], and thus enable mode splitting  $\Delta\lambda_p/\delta\lambda > 5$ . Such improvements would place these devices into a regime where they may be suitable for practical realizations of high efficiency polarized single-photon sources [64], and we hope to explore these and other applications in future work.

## Chapter 5 -Integrated membrane-in-the-middle (MIM) cavity optomechanical devices

As overviewed in Chapter 1, our group has previously reported an integrated MIM cavity optomechanics platform [8]. However, further optimization of those first-generation devices is desirable. Specifically, for the second-generation devices we aimed to have a membrane with higher tensile stress (1 GPa), better alignment (by using MLA 150 direct laser lithography), and to implement vacuum-sealing of the optical cavities.

As discussed in the theory chapter, the membrane resonators are impacted by three dominant loss mechanisms: viscous damping, clamping loss, and material loss [8] [9].

Southworth *et al.* [7] proposed a theory for the viscous damping of a membrane resonator in a gas environment, encapsulated by recalling Equation 2.29:

$$Q^{-1} = \frac{\rho_{gas}c_{gas}}{\rho_{rest}tf} \text{ (eq 2.29) .}$$

Here,  $\rho_{gas}$  and  $\rho_{res}$  are the density of the adjacent gas and membrane material, respectively,  $c_{gas}$  is the speed of sound,  $t$  is the thickness of the membrane, and  $f$  is the resonant frequency. The quality factor is inversely proportional to the density of the gas, which is related to pressure (P) by:

$$P = \frac{Nk_B T}{V} = \frac{Nm_0}{V} * \frac{k_B T}{m_0} = const * \frac{M}{V} = const * \rho_{gas} \text{ (eq 5.1)}$$

Thus, performing measurement in a vacuum environment can reduce viscous damping and increase the quality factor. Figure 5.1 shows the relationship between the mechanical quality factor and pressure as measured by Southworth for a series of SiN drumhead membranes [7].

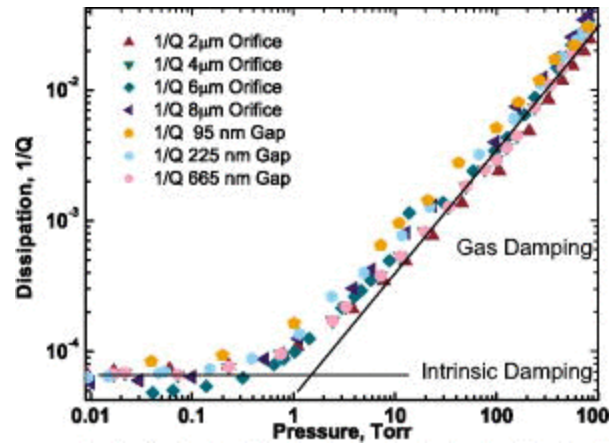


Figure 5.1 The dependence of the mechanical Q-factor for a SiN drumhead membrane on the ambient pressure. Except for very low pressures where the Q-factor is limited by the intrinsic damping loss, the  $1/Q$  is proportional to pressure. Adapted from [7].

These types of experiments are usually performed in an optical vacuum chamber with windows on either side for optical access. By integrating the vacuum chamber into the optical system, the optical microcavities can then be measured in a vacuum environment. Figure 5.2 shows a vacuum chamber which I designed to facilitate studies of this type; several experiments were successfully performed using this system, as described below.

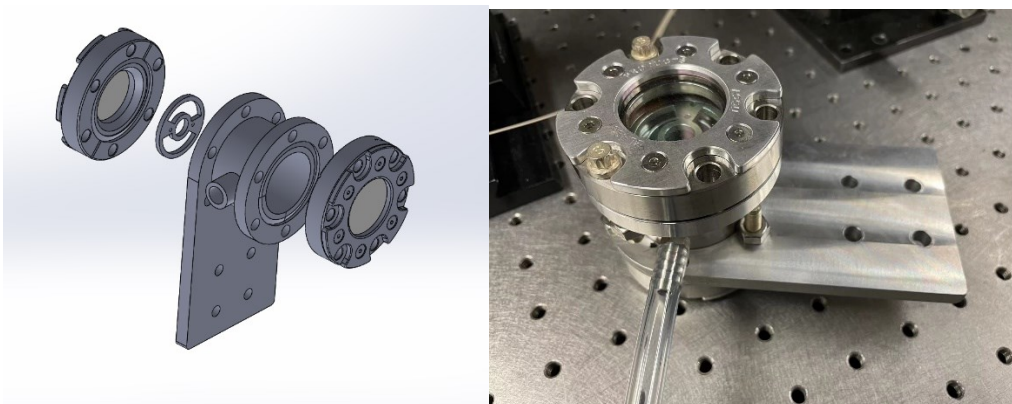


Figure 5.2 The vacuum chamber designed for optical measurements of microcavities at low ambient pressures. (a) an exploded-view schematic, (b) a photograph.

### 5.1 Optical studies of fabricated MIM devices before and after sealing attempts

The optical measurement of our cavity devices can be performed in either reflection or transmission. Given an input signal, the experimental setup can measure either the transmitted optical signal or reflected optical signal, as illustrated in Fig. 5.3. An illuminator (white light lamp) was also added for a more efficient investigation of the dome optical cavity.

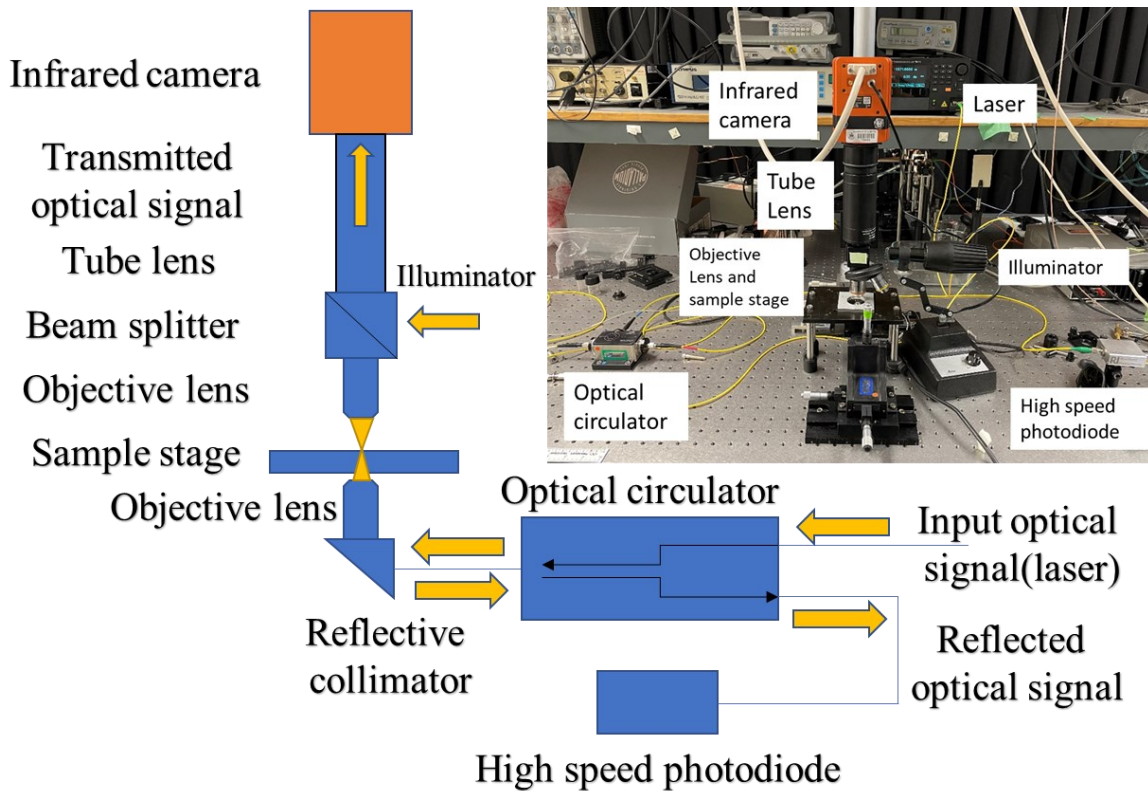


Figure 5.3 The experimental setup constructed to facilitate optical measurements of the MIM cavities is shown. This setup can perform the measurement of both the transmitted and reflected light from a cavity. The top right corner is a photo of the setup.



### **5.1.1 Reflection mode measurement**

Reflection mode measurements can be employed to characterize the thermo-mechanical properties of the mechanical membrane resonators embedded inside our MIM cavities, using a tuned-to-slope technique [8]. The reflection measurement system consists of a Santec TSL 550 tunable laser (1480-1640 nm), a Thorlabs RC08FC-P01 reflective collimator, an optical circulator, and a Resolved Instruments high-speed photodiode. The optical circulator has 3 ports: input, bidirectional, and output. The input port is connected to the Santec laser, the bidirectional port is connected to the RC08 reflective collimator and a 20X objective lens, and the output port is connected to the Resolved Instruments high-speed photodiode. All the connections are fiber-coupled; the specification of the fibers is single-mode (SMF-28) fiber suitable for operation for wavelengths in the 1550 nm range. The optical signal is input to the RC08 reflective collimator followed by a 20X objective lens and is focused onto the device of interest. It is noteworthy that the input sample stage is fixed to reduce the mechanical vibration since the mechanical vibration of the sample stage will reduce the signal-to-noise ratio of the tuned-to-slope noise spectral measurement.

### **5.1.2 Transmission mode measurement**

The transmission setup is used for measuring the spectral response of the optical cavity. The transmission measurement can be categorized into two main parts: the input and output optical system. The input optical system is the same as the reflection mode measurement system, and the output system contains a 10X objective lens, a 90:10 beam splitter, a tube lens, and the Raptor NIR camera. For an improved signal-to-noise ratio, the optical circulator is removed for the transmission measurements.

## 5.2 Experimental results

### 5.2.1 Spectral response

Having a fundamental optical mode within the range of the tunable laser is required to facilitate the tuned- to-slope measurement. The mechanical noise spectrum is extracted by monitoring the optical intensity fluctuations caused by the change in position of the buckled mirror and/or the membrane, which in turn modulates the optical resonance of the cavity. Spectral scans are obtained from the transmission mode measurements. Our group has developed an algorithm to perform the spectral scan, which can be divided into two steps: 1. Changing the wavelength of the laser. 2. Computing the pixel sum of the optical mode-field intensity captured by the NIR camera. By alternating these steps of the algorithm, a spectral scan is collected. To obtain a high signal-to-noise ratio spectral scan, one has to carefully align the laser in order to excite the optical modes, while also being careful to not saturate the camera pixels (i.e., to ensure a linear measurement).

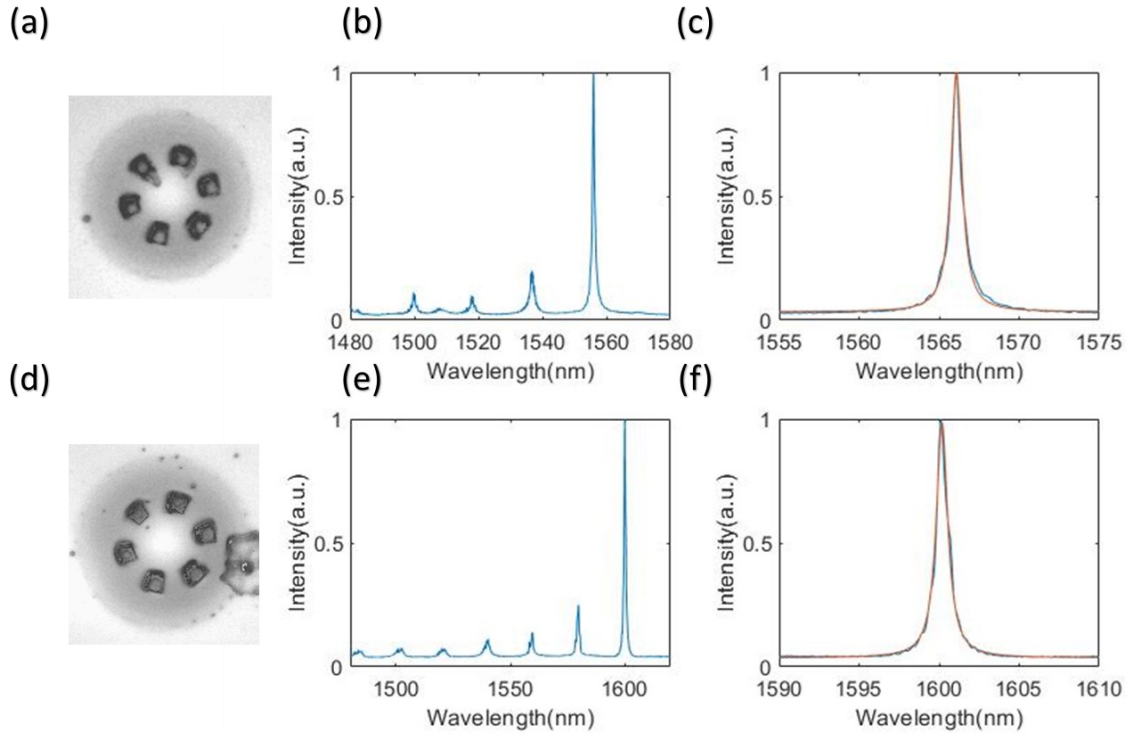


Figure 5.4 Optical spectral response of two selected dome optical cavities, both with  $50 \mu\text{m}$  base diameter. (a)(d), microscope photos of the domes. (b)(e), full-range optical scan. (c)(f) Short-range scan near the fundamental resonance as well as fitting of the fundamental mode lineshape to a Lorentzian profile. (Blue curve is the data, and red is the fitting)

The optical responses amongst a large number of trials were similar. The spectral responses presented in Fig. 5.4 are from devices corresponding to trial number 2 (see Table 4.1). As shown in Fig. 5.4, these microcavities exhibit a typical linewidth of about  $0.8 \text{ nm}$  for their fundamental resonance, and the spacing between higher-order Hermite-Gaussian modes is about  $20 \text{ nm}$ , both of which were in good agreement with theoretical predictions ( $\Delta f = \frac{c}{2\pi z_0} \sim 3 \text{ THz}$  corresponding to  $24 \text{ nm}$  at  $1550 \text{ nm}$  wavelength range) and with our previous results for similar cavities [15]. From profilometer scans, the length of these optical cavities (i.e., the peak height of

the buckled domes) is  $\sim 3\text{-}4$  microns, which corresponds to about the fourth-order longitudinal mode. Based on this data, the estimated optical quality factor is  $Q \sim 1800$ , corresponding to the finesse  $F \sim 450$ . This is lower than the finesse predicted by simulations ( $F \sim 900$ ), possibly due to the extra scattering loss caused by the embedded SiN membrane.

### 5.2.2 No Sealing/ Control group

As in the preceding discussion, the following study is focused on MIM optomechanical cavities with base diameter of  $50\ \mu\text{m}$ . We first studied thermal-mechanical noise spectra for the cavities that were not subjected to any ‘sealing’ depositions. Thus, these cavities have open access holes, and the embedded SiN membranes are expected to have their mechanical resonances damped by their interactions with the ambient (air) environment [8]. A typical result is shown in Fig. 5.5. For the tuned-to-slope measurement shown, the input laser power was 4 dBm, and the input wavelength was 1583.3 nm (i.e., on the side of the fundamental resonance determined by an optical spectral scan for this device). As in our previous work [8], we believe that the mechanical vibrational resonances in the 0-40 MHz range shown can be attributed to vibrations of either the buckled mirror (‘mirror’ modes) or the embedded SiN membrane (‘membrane’ modes). One goal of these measurements, and related modeling, is to confirm the existence of a freely vibrating membrane inside a given cavity. For the device shown in Fig. 5.5, which was typical, the first mechanical resonance is located at 5.02 MHz, with a quality factor of 166, and is almost certainly associated with a vibrational mode of the buckled mirror [8]. However, the second vibrational resonance located at 8.86 MHz, and with a quality factor of 146, is possibly associated with the SiN membrane vibrations, since we do not expect a second order ‘mirror’ vibrational mode at this frequency [8]. If the two peaks present on the thermomechanical noise spectrum are from the same (nominally circular) structure, then the resonating frequency ratio

between modes should satisfy the ratio between zeros of the Bessel functions. For instance, the first zero of Bessel function is at 2.4048 and the second zero is at 3.8317. Assume two vibrating modes are caused by same structure: if the fundamental mode is at 5.02 MHz, the second mode should be located at 7.99 MHz, not the observed 8.86 MHz. Thus, an assumption was made that the 8.86 MHz peak is corresponding to the membrane mode. As mentioned, the data shown in Fig. 4.11 was typical for ‘unsealed’ devices and serves as a baseline for comparison to the results after sealing attempts.

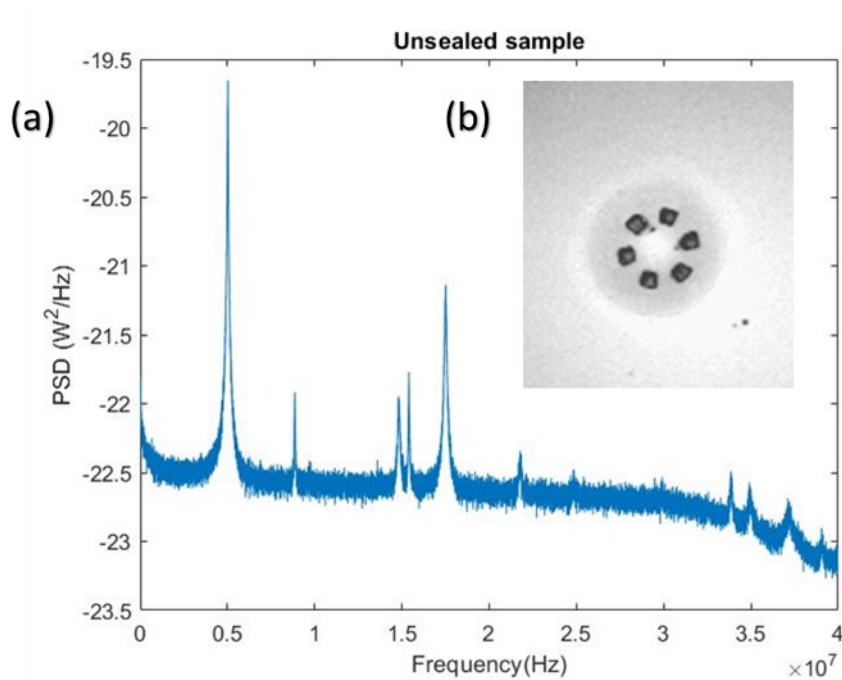


Figure 5.5 (a), A typical thermo-mechanical noise spectrum for an ‘unsealed’ optical cavity. As discussed in the main text, the mechanical vibrational modes at various frequencies are attributed to either ‘mirror’ or ‘membrane’ oscillations. (b), a microscope photo of the optomechanical cavity.

### 5.2.3 Sputter Sealing (sealing attempt 1 and 2)

Sputtering is a line-of-sight deposition method. In the vacuum-sealing process, this is advantageous in terms of eliminating unwanted deposition onto the membrane. In this experiment, the deposition pressure of the sputtering is 4mTorr. However, likely due to the poor sidewall coverage of the sputtering process, the sealing attempts that used sputtering (attempts 1 and 2 as detailed in Table 3.1) were unsuccessful, as evidenced by the fact (shown below) that we did not observe a significant improvement in the mechanical quality factor compared to the results for the control group domes discussed in Section 5.2.2.

A typical spectral scan obtained using the transmission setup discussed earlier is shown in Fig. 4.12. The wavelength range of scanning was from 1480 nm to 1640 nm, with a wavelength increment of 0.1 nm, and power was kept at -14 dBm to minimize the heating of the device. In terms of optical quality factor and transverse mode spacing, these devices were very similar to those in the control group.

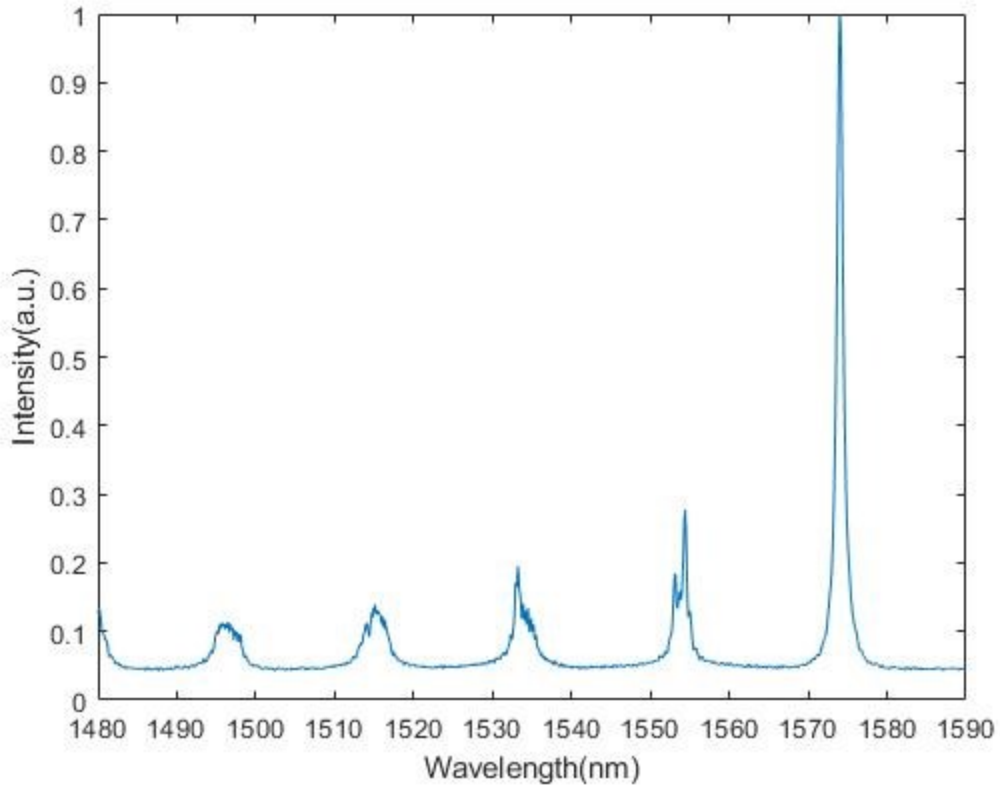


Figure 5.6 A sample spectral scan of a device from the chip which we attempted to seal through sputtering of additional layer.

Figure.5.6 shows microscope photos of typical devices and their corresponding thermomechanical noise spectra. As above, the nominal base diameter of the MIM optomechanical cavities studied is  $50 \mu\text{m}$ . The mechanical quality factor of the first two peaks is listed in Table 5.1.

Sample	First peak location/ quality factor	Second peak location/ quality factor
1	7.76 MHz/ 277	11.7 MHz/ 194

2	7.45 MHz/ 185	11.6 MHz/ 290
3	7.69 MHz/ 256	11.5 MHz/ NA
No sealing/ control group	5.02 MHz/ 166	8.86 MHz/ 146

Table 5.1 The frequency and quality factor selected mechanical mode of representative devices 1,2, and 3 from trial 2, compared to a similar size device from the control group.

Following a similar analysis in section 5.2.2, if the two peaks are attributable to the same structure, the resonating frequency ratio between modes should satisfy the ratio between zeros of the Bessel functions. Thus, it was speculated that the first peak is due to the buckled mirror vibration while the second peak is due to the vibration of the embedded membrane. While the mechanical quality factors were not significantly altered by the additional sputtered layers, it is clear that the addition of these extra layers caused the fundamental mechanical mode resonance frequency to be increased from  $\sim 5$  MHz to  $\sim 7.5$  Mhz. This phenomenon might be related to ‘pinning’ of the membrane at the locations of the etch holes, which is a result of the sputtering deposition. Such a pinned membrane has smaller effective diameter and mass, and thus would be expected to exhibit higher resonant vibrational frequencies as was observed. According to eq 2.32, if the effective pressure adjacent to the internal membrane had been decreased from  $\sim 760$  Torr to  $\sim 4$  mTorr (i.e., the pressure of sputtering chamber during the layer deposition), the quality factor of the mechanical resonator should increase to  $\sim 10^4$ , which is not observed. Thus, we concluded that this vacuum sealing attempt was not successful, possibly due to the line-of-sight deposition resulting in poor sidewall coverage. It is noteworthy that device 3 shows an asymmetric Lorentzian lineshape at  $\sim 11.5$  MHz, possibly due to the coupled oscillation between the dome and the membrane, as is discussed in more detail below.



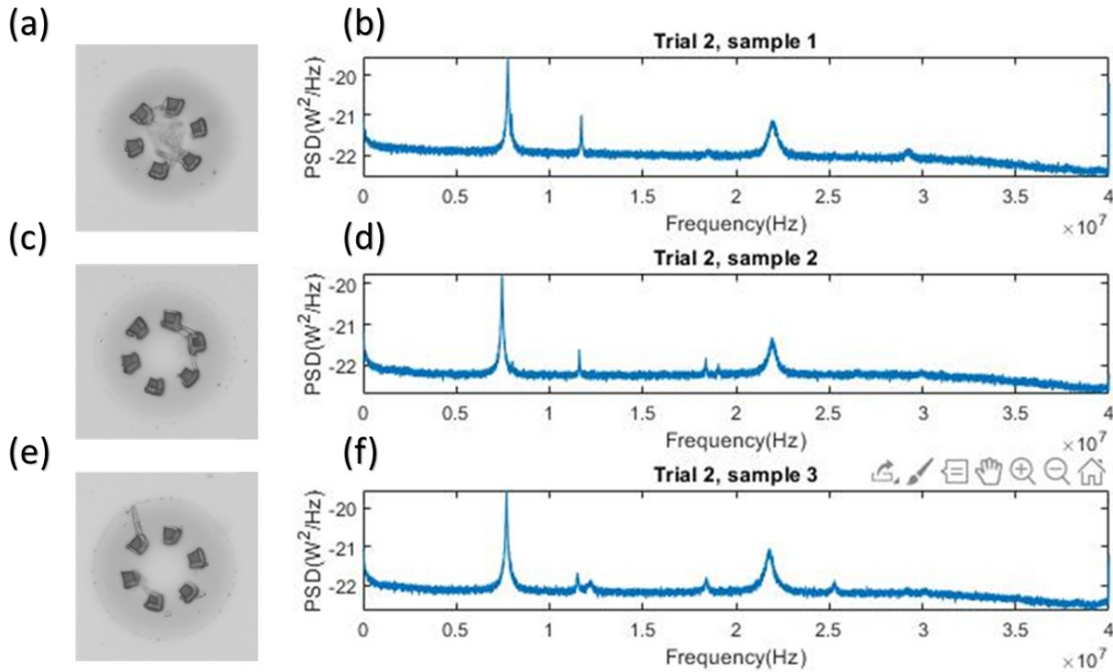


Figure 5.7 (a)(c)(e), microscope image of devices from sealing attempt 2. (b)(d)(f) thermomechanical noise spectrum of the devices, taken from reflection mode measurements.

### 5.2.4 Parylene Sealing Attempt (sealing attempt 3)

Parylene is deposited using a physical vapor deposition method (PVD), such that the parylene vapor condenses on any cooled surface. Thus, parylene deposition is a truly conformal coating method. There are three types of Parylene, namely, type C, type D and type N [47]. In this experiment a parylene type C coating is used because type C has better conformality and lower gas permeability [38] [39] [40] [41]. To seal the optical cavities which have etch access holes with a minimum size of 4  $\mu\text{m}$ , it follows for a conformal deposition that at least 2  $\mu\text{m}$  of Parylene coating is needed. As above, the experimental results below are restricted to buckled domes with nominal base diameter of 50  $\mu\text{m}$ . The hope was that the parylene coating would grow inward from the sidewalls of the access holes and eventually merge such that the process

would seal the optical cavity. However, there is a concerning fact that the parylene deposition is too conformal and may result in deposition on the silicon nitride membrane too, thus, greatly damping the membrane. The deposition pressure of the parylene system is 70 mTorr.

After the Parylene deposition attempt, it was observed that the fundamental mechanical mode resonant frequency shifted from  $\sim 5$  MHz to 7-9 Mhz. As discussed earlier, the assumption is made that the first peak is due to the buckled mirror vibrational mode, and the second peak is due to the membrane vibrational mode. This is shown for two representative devices, in Table 5.2 and Fig. 5.8. The quality factor of the fundamental resonance was  $\sim 121$  and  $\sim 88$ , respectively, for devices 1 and 2, which is lower than the control group ( $Q=166$ ). According to eq 2.32, if the pressure decreases from 760 Torr to about 70 mTorr, the quality factor of the mechanical resonator should increase to  $\sim 10^4$ , which was clearly not observed. We speculated that this might possibly be due to the deposition of parylene onto the silicon nitride membrane itself, thereby damping the mechanical quality factor of the membrane. Another possibility is that the parylene did not actually result in a sealed cavity, such that viscous damping is still dominant.

Sample	First peak location/ quality factor	Second peak location/ quality factor
1	9.74 MHz/ 88	14.6 MHz/ 73
2	7.09 MHz/ 121	10.6 MHz/132
No sealing/ control group	5.02 MHz/166	8.86 MHz/146

Table 5.2 The frequency and quality factor for selected mechanical modes of representative devices 1,2, and 3 from the chip coated with parylene in trial 3 and compared to the control group device.

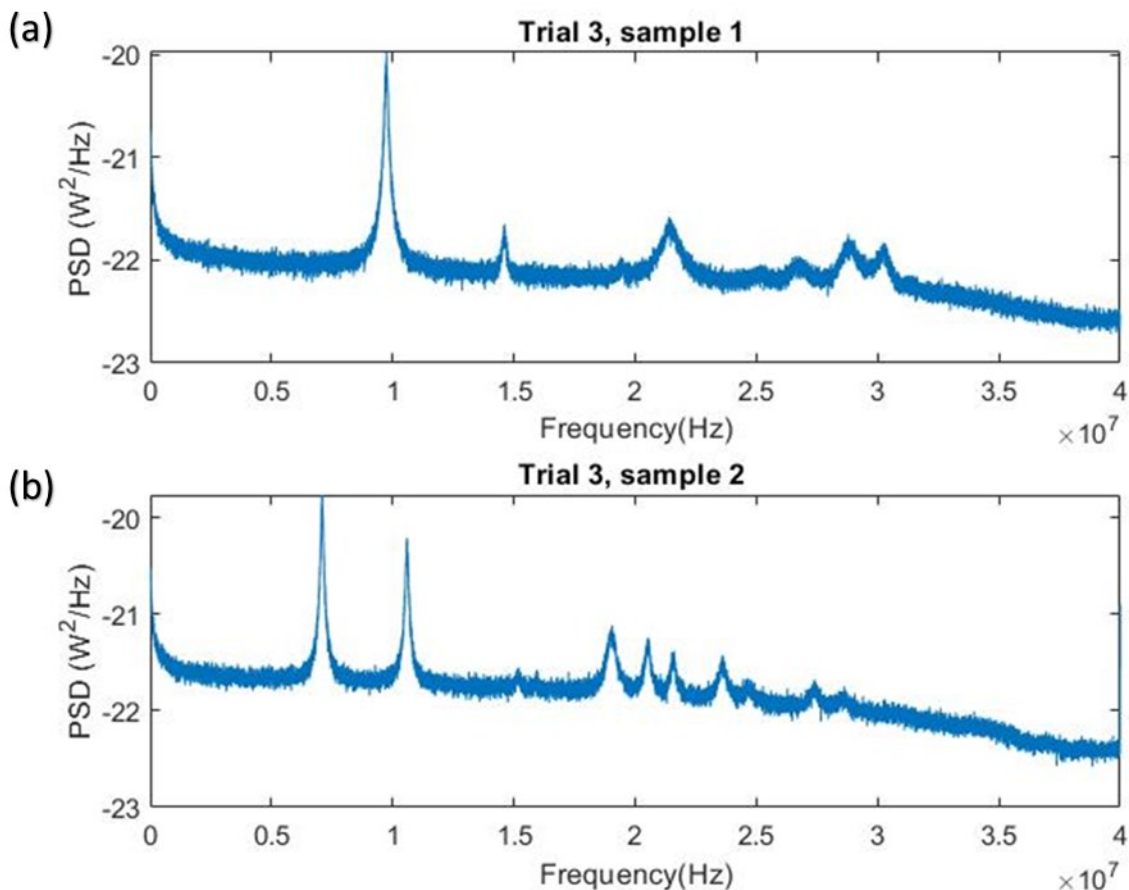


Figure 5.8 (a)(b) The thermomechanical noise spectrum after the parylene deposition attempt, showing that the peaks are broadened (i.e., lower mechanical quality factor) compared to trial 2 and compared to the control devices.

### 5.2.5 PECVD Sealing Attempt (sealing attempt 4)

Another option which was attempted for sealing the dome optical cavities was the deposition of a thick PECVD oxide overlayer. This is a widely reported vacuum sealing technique in the

literature and is known as MEMS vacuum packaging [43] [44]. Since this sealing process is a chemical reaction, any surface that has access to precursor gas will be subject to thin film deposition. In our experiment, a standard U of A nanoFab PECVD silicon dioxide recipe was used, with the deposition pressure at 800 mTorr and the substrate temperature at 325 °C. As detailed in Table 4.1, this PECVD oxide layer (~2  $\mu\text{m}$  thick) was deposited onto a chip which had already been deposited with a 2-period (sputtered) Si/SiO<sub>2</sub> addition to the upper buckled mirror. As above, the results shown below are for buckled dome cavities with nominal base diameter of 50  $\mu\text{m}$ .

Unfortunately, likely due to high substrate temperature inducing thermal mismatch and the poor adhesion between Si/SiO<sub>2</sub> QWS layers and the underlying SiO<sub>2</sub>/Ta<sub>2</sub>O<sub>5</sub> QWS layers, all the Si/SiO<sub>2</sub> QWS layers delaminated (along with the added PECVD oxide) following the PECVD deposition step. Nevertheless, the buckled cavities (with the original upper mirror intact) survived the process. Moreover, from microscope inspection, it appeared that the etch access holes were left ‘plugged’ by the PECVD oxide, such that the optical cavities had in fact possibly been vacuum- sealed. To ensure a sufficiently high optical quality factor to perform tuned-to-slope measurements, this chip was subsequently cleaned and deposited (by sputtering) with another 1 period of Si/SiO<sub>2</sub> QWS layers.

Spectral scans were obtained with the transmission setup discussed earlier. As above, the wavelength range of scanning was from 1480 nm to 1640 nm, with a wavelength increment of 0.1 nm, and power was kept at -14 dBm to minimize the heating of the device. Fig.4.15 shows a typical spectral scan for a device on this chip.

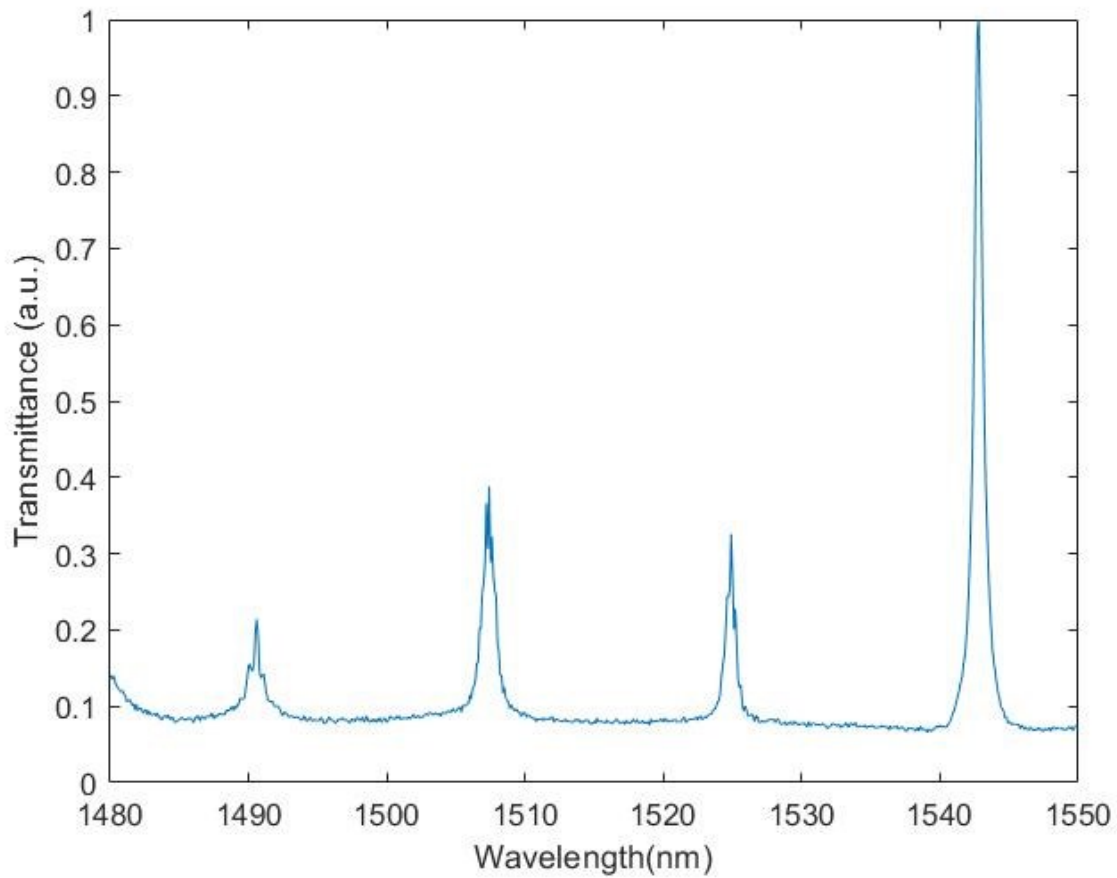


Figure 5.9 A sample spectral scan of a device from the chip which we attempted to seal through PECVD deposition of additional layer.

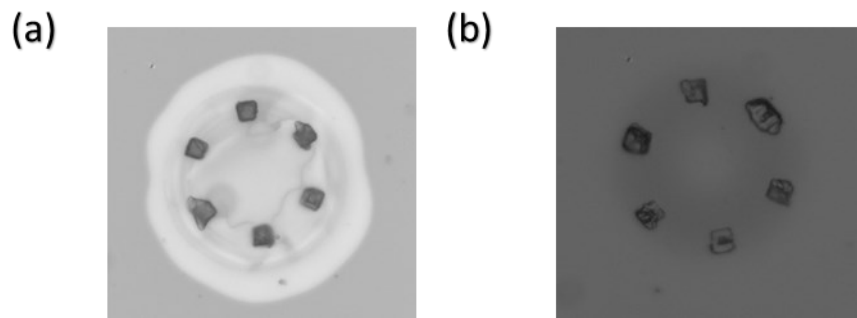


Figure 5.10 (a) The microscope image after PECVD sealing but prior to re-sputtering Si/SiO<sub>2</sub> QWS, the outer perimeter of the released SiN membrane is visible, and the access holes appear

to be sealed. (b) The microscope image of PECVD deposited chip after sputtering a Si/SiO<sub>2</sub> bilayer to regain sufficient optical Q for tuned-to-slope measurement. The perimeter of the membrane is no longer visible since Si is opaque to visible light.

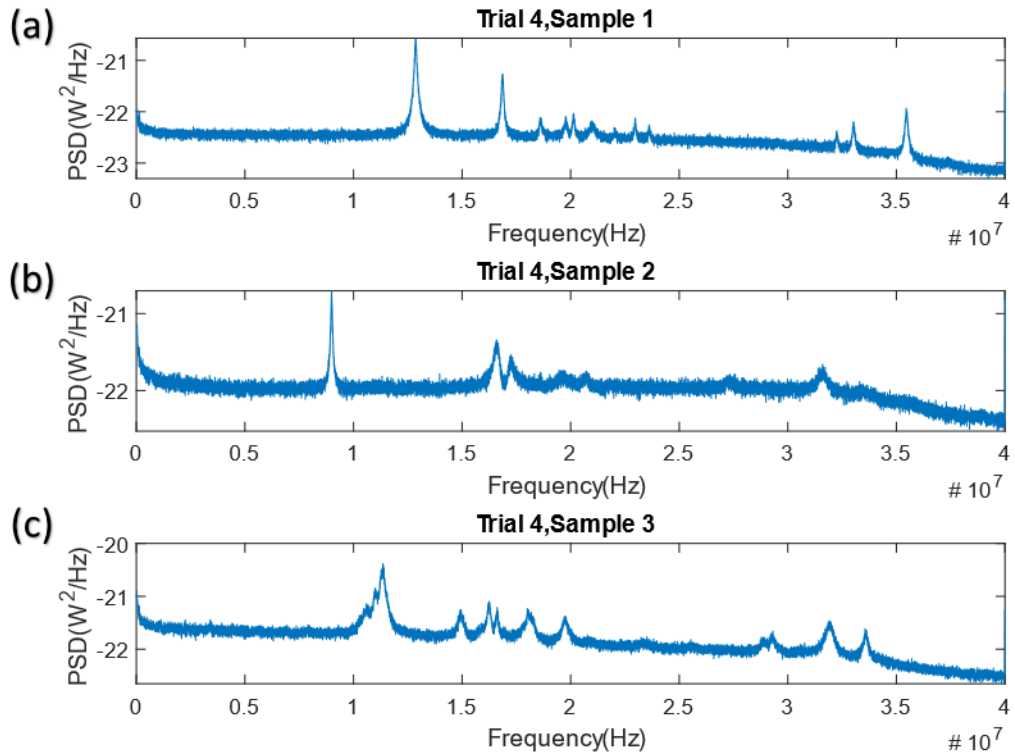


Figure 5.11 (a)(b)(c), the thermomechanical noise spectrum after PECVD sealing and re-sputtering of a 1-period Si/SiO<sub>2</sub> bilayer (see main text). (a) shows an asymmetric Lorentzian at 20 MHz. (b) shows an asymmetric Lorentzian at 16 MHz, (c) shows an asymmetric Lorentzian at 16 MHz.

Device	First peak location/ quality factor	Second peak location/ quality factor
1	12.86 MHz/ 143	16.86 MHz/ 168
2	9.00 MHz/ 150	NA
3	NA	NA
No sealing/ control group	5.02 MHz/ 166	8.86 MHz/ 146

Table 5.3 The frequency and quality factor selected mechanical mode of samples 1,2, and 3 in trial 4. Defining quality factors for some peaks are not possible due to their asymmetric line shape which will be noted as NA.

Representative thermo-mechanical noise spectra are shown in Fig. 5.11 and summarized in Table 5.3. Similar to above, the assumption is made that the first peak is due to the buckled mirror vibrational mode and the second peak is due to the membrane vibrational mode. Besides, the attempt at sealing clearly resulted in an increase in the fundamental mechanical resonance frequency (from  $\sim 5$  MHz to 8-12 MHz). However, the quality factors are similar to that observed for the control group. According to Eq. 2.32, if the pressure experienced by the embedded membrane had truly decreased from 760 Torr to about 800 mTorr, the quality factor of the mechanical resonator should increase to  $\sim 10^3$ . As for the previous sealing attempts described above, this unfortunately not observed. This indicates either that the PECVD deposition also failed to seal the internal cavity from the external environment, or that the viscous damping is not actually the main mechanical loss mechanism of our optomechanical system. The answers to these questions are left for future work.

### 5.2.6 Evidence for coupled mechanical resonators after the PECVD sealing attempt

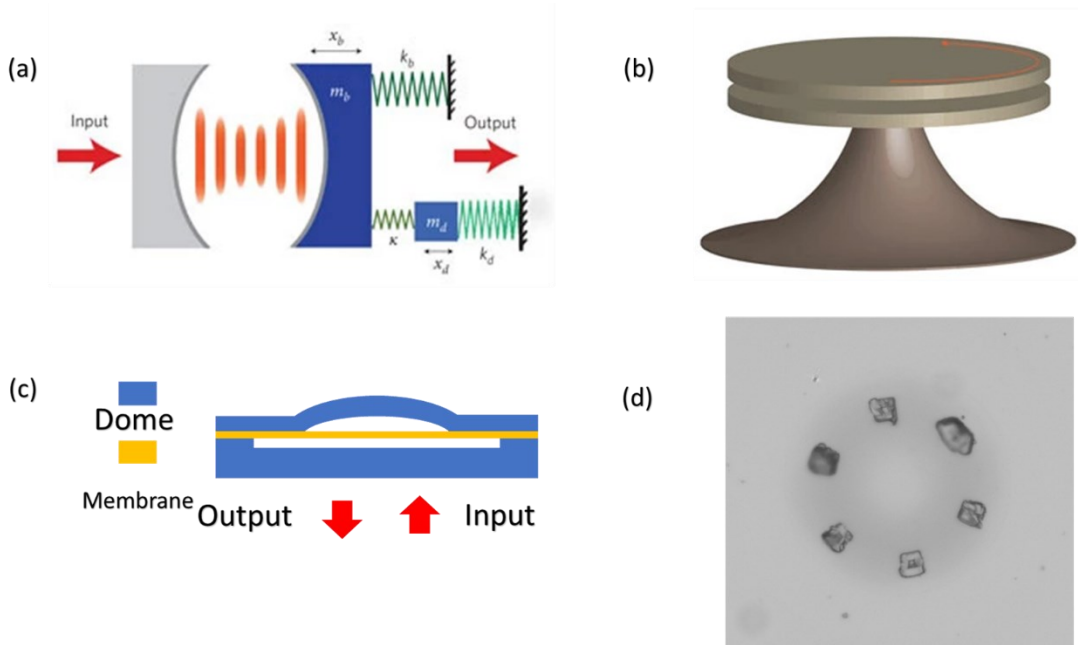


Figure 5.12 (a), the system diagram of an optomechanical system with coupled mechanical resonators, adapted from [70]. (b), the diagram of the setup in Qiang Lin’s work, adapted from [70]. (c), the cross-section diagram of the sample. (d) a microscope image of the studied dome, with a nominal base diameter of  $50 \mu\text{m}$ .

After using PECVD deposited oxide in an attempt to seal the optical cavities, some devices exhibited mechanical modes with an asymmetric Lorentzian response, which might be related to the presence of coupled mechanical resonators [70] [71]. The asymmetric lineshape is the mechanical counterpart of Fano resonance and electromagnetically induced transparency (EIT) [71] [72]. Our optomechanical system involves a vibrating buckled mirror and a vibrating membrane, which is equivalent to simultaneously incorporating a mirror-at-end and a membrane-in-the-middle optomechanical system. As above, the results shown here are for buckled domes with nominal base diameter of  $50 \mu\text{m}$ .



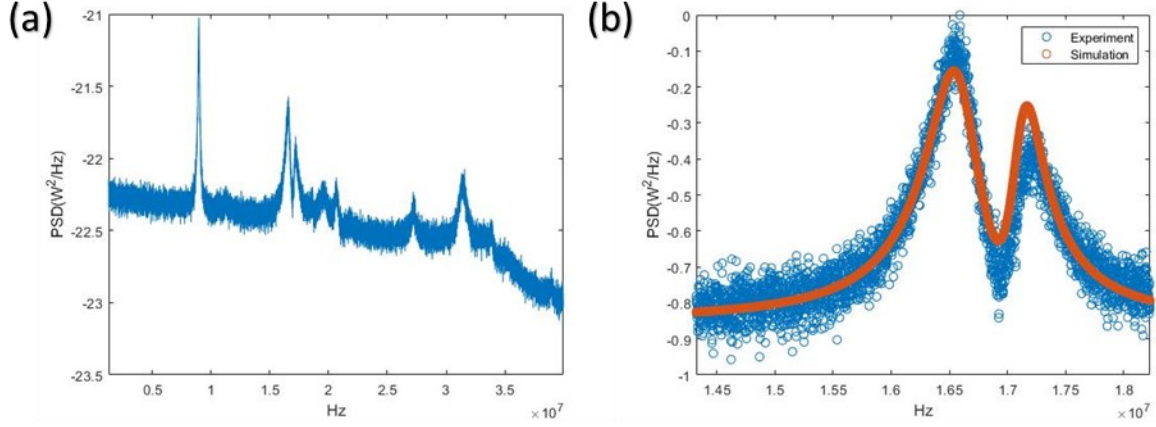


Figure 5.13 (a) Typical thermos-mechanical noise spectrum for the PECVD-deposited sample, with the device exhibiting an asymmetric Lorentzian feature at  $\sim 16.5$  MHz, similar to the devices shown in Fig 4.17(b). (b), the zoomed and normalized view (From 14.3MHz to 18.2MHz) of the asymmetric Lorentzian, the MSE of the fitting is 7.0810.

As mentioned, features such as shown in Fig. 5.13 (b) are possibly a signature of a coupled pair of mechanical resonators. Lin et al. [70] provided a formula to fit the asymmetric Lorentzian response for such a system, where the total thermomechanical noise spectrum is the overall response of the mechanical modes  $L_D(\Omega)$  and  $L_B(\Omega)$  associated with two coupled mechanical oscillators, and where  $\Omega$  is the mechanical vibration frequency:

$$S_{xb}(\Omega) = \frac{2k_B T}{m_b} * \frac{\eta^4 \Gamma_{md} + \Gamma_{mb} |L_D(\Omega)|^2}{|L_D(\Omega)L_B(\Omega) - \eta^4|^2} \quad (eq\ 5.2)$$

Here,  $k_B$  is the Boltzmann constant, T is the temperature,  $m_b$  is the effective mass of mode  $L_B(\Omega)$ ,  $\eta$  is the coupling strength, and  $\Gamma_{md}$  and  $\Gamma_{mb}$  are the loss rate of two mechanical modes,

respectively.

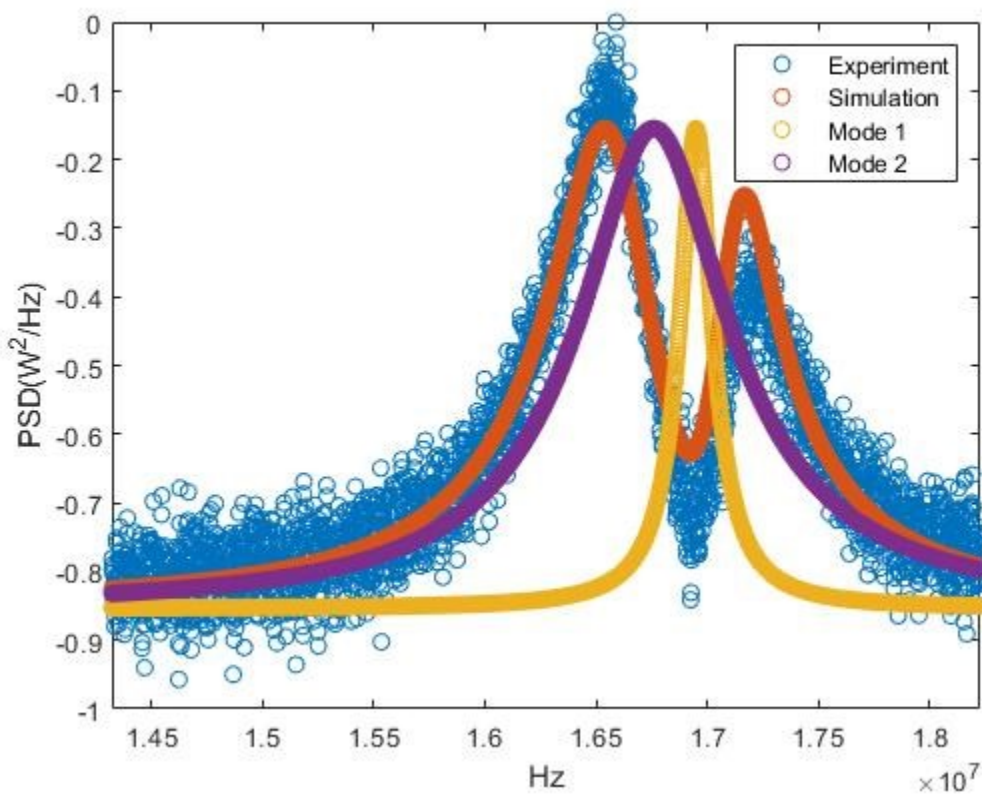


Figure 5.14 The experimental data for the asymmetric resonance near 16.5 MHz, from Fig 4.19 (b). The blue curve is the experimental data, the red curve is the overall fitting using Eq. 4.2. The purple curve is for the assumed mode 1 ( $L_D(\Omega)$ ), and the yellow curve is for the assumed mode 2 ( $L_B(\Omega)$ ) associated with a coupled pair of mechanical oscillators. Mode 1 and 2 destructively interfere and form such an asymmetric line shape.

To achieve an empirical fit to the asymmetric lineshape shown in Fig. 5.14 using Equation 5.2, we assumed a first mechanical mode  $L_D(\Omega)$  with a quality factor of 30 and resonating at 16.76 MHz and second mechanical mode  $L_B(\Omega)$  with a quality factor of 140 and resonating at 16.95 MHz. Since these two modes are closely located and coupled, an asymmetric line shape was generated. Considering the noise floor is about  $10E-22.5$ , by applying  $S_{tot}(\Omega) =$

$S_0 + S_{xb}(\Omega)$ ), a reasonable fit, which is linearly proportional to the measurement, is obtained. The MSE of this fit is 7.0810. This is a reasonable fitting; however, further experiments are required, this will be left as future work.

### 5.2.7 Discussion

We have demonstrated the design, fabrication, and characterization of MIM optomechanical cavities. The optical responses of the MIM devices generally agree with theoretical predictions (i.e.  $Q \sim 1800$ ,  $F \sim 450$ , and  $\sim 20$  nm transverse mode spacing).

For the sputtering sealing attempts, in the best-case scenario, the mechanical quality factor of the assumed membrane is 277, well below the theoretical projection ( $\sim 10000$ ). The fundamental frequency shifted from  $\sim 5$  MHz to  $\sim 8$  MHz, possibly due to the pinning of vibrating structures.

For the Parylene sealing attempts, in the best-case scenario, the quality factor of the assumed membrane is 121, again well below with the theoretical projection ( $\sim 10000$ ). Besides, the measured quality factor is lower than the control group, indicating that the deposition might also have occurred on the membrane, thus, damping its vibration further. The fundamental vibrating frequency shifted to higher frequency, from  $\sim 5$  MHz to  $\sim 10$  MHz.

For the PECVD sealing attempts, the fundamental vibration frequency shifted to higher frequency, from  $\sim 5$  MHz to  $\sim 10$  MHz. The quality factor of the assumed membrane is hard to define due to the coupled-resonator effect. Since there should be two vibrating structure to form a coupled resonator, these observations further verify that the existence of the membrane modes.

## Chapter 6 - Conclusion, and future work

### 6.1 Summary

This thesis described research on the fabrication and study of monolithic membrane-in-the-middle (MIM) cavity optomechanical systems, as well as research on highly birefringent, elliptical buckled-dome microcavities.

For the MIM resonators, compared to earlier generation devices, devices with improved photolithographic alignment and a higher tensile stress embedded silicon nitride membrane were fabricated. Various approaches to vacuum-sealing of the optomechanical cavity were attempted. A vacuum chamber system was also designed and fabricated and integrated into optical measurements. The optical response of the MIM devices was generally well predicted by theory ( $Q \sim 1800$ ,  $F \sim 450$ ). However, the mechanical resonator response still requires further experimentation. The devices exhibited thermomechanical noise spectra with a mechanical quality factor of  $\sim 200$  at various vibrational mode frequencies in the 5 MHz- 15 MHz range. Some thermomechanical noise spectra exhibited asymmetric Lorentzian shapes, which we speculatively attributed to coupling between two mechanical objects (i.e., the buckled mirror and the embedded silicon nitride membrane). This observation might have interesting implications for applications in quantum optomechanics, further experimentation is needed to confirm the underlying physics.

For the elliptical buckled-dome birefringent optical microcavities, devices were successfully fabricated with a large difference in radius of curvature along major and minor axis of the elliptical profile. For example, a typical device exhibited radii of curvature of  $\sim 300 \mu\text{m}$

and  $\sim 60 \mu\text{m}$  along major and minor axes, respectively. The optical spectra exhibited polarization-mode splitting of the Laguerre-Gaussian cavity modes, in good agreement with theoretical predictions from a vector solution of the paraxial wave equation. The finesse of these optical cavities was about  $\sim 250$ , and the polarization mode splitting of the fundamental optical mode was  $\sim 25\text{GHz}$  in  $1550 \text{ nm}$  wavelength range, significantly larger than reported for other elliptical spherical-mirror microcavities reported in the literature.

## 6.2 Future work

Perhaps the most interesting topic for future work is a further evaluation of the ‘coupled mechanical resonators’ that might be present in the MIM devices. Several observed line shapes within the mechanical vibrational spectra were qualitatively very similar to the shapes predicted by the theory of coupled mechanical oscillators found in the literature. Since our MIM optomechanical resonators have both a vibrating mirror and a vibrating membrane, it is highly likely that they are coupled to each other under the right conditions (i.e., when vibrational modes of the mirror and membrane happen to be nearly degenerate in frequency). In the future, it would be of significant interest to explore the design and fabrication of buckled dome MIM systems that are specifically designed to ensure strong coupling between the mirror and membrane vibrational modes.

Another topic for future work is the fabrication of third generation MIM devices with a  $\text{Ta}_2\text{O}_5/\text{SiO}_2$  bottom mirror. This would address the problem we encountered with the unintentional etching of a-Si layers in the bottom mirror of the second-generation devices, when performing the  $\text{XeF}_2$  membrane release step, as described in Chapter 4. A  $\text{Ta}_2\text{O}_5$ -based bottom mirror would not be prone to attack by the  $\text{XeF}_2$  etchant.

Another avenue for exploration is a possible switch to the use of low-pressure chemical vapor deposition (LPCVD) to fabricate the silicon nitride membrane, instead of the PECVD process used in the present work. Based on other results in the literature, and established procedures at the U of A nanoFab, this would improve the mechanical quality factor, since, compared to LPCVD, PECVD is still a high-energy plasma process. If a LPCVD silicon nitride membrane was made and successfully integrated into the buckled microcavity process, it is expected that a much higher mechanical quality factor should be achieved.

Finally, in the long term, the further integration of a microwave circuit into the cavity optomechanical system is also desirable. Such a device might serve as a quantum transducer, mediated the exchange of coherent quantum states between optical photons and microwave photons [15] [12].

## Reference

- [1] H. J. Kimble, "The quantum internet," *Nature*, vol. 453, pp. 1023-1030, 2008.
- [2] H. Walther, B. T. H. Varcoe, B.-G. Englert and T. Becker, "Cavity quantum electrodynamics," *Reports on Progress in Physics*, vol. 69, no. 5, 2006.
- [3] S. M. Girvin, R.-S. Huang, A. Blais, A. Wallraff and R. J. Schoelkopf, "Prospects for Strong Cavity Quantum Electrodynamics with Superconducting Circuits," in *Proceedings of the Les Houches Summer School 2003 (Les Houches, Volume Session LXXIX)*, 2004.
- [4] M. Aspelmeyer, T. J. Kippenberg and F. Marquardt, "Cavity optomechanics," *REVIEWS OF MODERN PHYSICS*, vol. 86, pp. 1391-1452, 2014.
- [5] G. Kurizki, P. Bertet, Y. Kubo, K. Mølmer, D. Petrosyan, P. Rabl and J. Schmiedmayer, "Quantum technologies with hybrid systems," *Proceedings of the National Academy of Sciences*, vol. 112, no. 13, 2015.
- [6] J. D. Thompson, B. M. Zwickl, A. M. Jayich, F. Marquardt, S. M. Girvin and a. J. G. E. Harris, "Strong dispersive coupling of a high-finesse cavity to a micronmechanical membrane," *Nature letters*, vol. 452, pp. 72-75, 2008.
- [7] D. R. Southworth, H. G. Craighead and a. J. M. Parpia, "Pressure dependent resonant frequency of micromechanical drumhead resonators," *APPLIED PHYSICS LETTERS*, vol. 94, 2009.
- [8] G. J. Hornig, S. Al-Sumaidae, J. Maldaner, L. Bu and a. R. G. DeCorby, "Monolithically integrated membrane-in-the-middle cavity optomechanical systems," *2020*, vol. 29, no. 19, pp. 28113-28125, Optics Express.
- [9] S. Schmid, L. G. Villanueva and M. L. Roukes, "Fundamentals of Nanomechanical Resonators," 2016, pp. 57-90.
- [10] D. Kleckner, B. Pepper, E. Jeffrey, P. Sonin, S. M. Thon and D. Bouwmeester, "Optomechanical trampoline resonators," *Optics Express*, vol. 19, no. 20, pp. 19708-19716, 2011.
- [11] Y. Tsaturyan, A. Barg, E. S. Polzik and A. Schliesser, "Ultracoherent nanomechanical resonators via soft clamping and dissipation dilution," *Nature*, vol. 12, pp. 772-783, 2017.

- [12] M. Metcalfe, "Applications of cavity optomechanics," *APPLIED PHYSICS REVIEWS 1*, 2014.
- [13] J.W.Hutchinson and Z.Suo, in *Mixed Mode Cracking in Layered Materials*, 1991, pp. 158-162.
- [14] T. Allen, J. Silverstone, N. Ponnampalam and R. DeCorby, "High-Finesse Cavities Fabricated by Buckling Self-Assembly," *Optics Express*, vol. 19, no. 20, pp. 18903-18909, 2011.
- [15] M. H. Bitarafan and R. G. DeCorby, "Small-mode-volume, channel-connected Fabry–Perot microcavities on a chip," *Applied Optics*, vol. 56, no. 36, pp. 9992-9997, 2017.
- [16] J. Maldaner, S. Al-Sumaidae, G. Hornig, L. LeBlanc and R. DeCorby, "Liquid infiltration of monolithic open-access Fabry–Perot microcavities," *Applied Optics*, vol. 59, no. 23, pp. 7125-7230, 2020.
- [17] G. Hornig, L. Bu, S. Al-Sumaidae and R. DeCorby, "Monolithic elliptical dome Fabry–Perot microcavities exhibiting large birefringence," *JOSA B*, vol. 39, no. 3, pp. 884-890, 2022.
- [18] B. D. Hauer, C. Doolin, K. S. D. Beach and a. J. P. Davis, "A general procedure for thermomechanical calibration of nano/micro-mechanical resonators," *Annals of Physics*, vol. 339, pp. 181-207, 2013.
- [19] S. O. Kasap, "Optoelectronics and Photonics, second edition," pp. 56-59.
- [20] W. Koechner and M. Bass, "Solid-State Lasers," in *Optical Resonator*, New York, NY, Springer, 2003, pp. 149-186.
- [21] N. Barré, M. Romanelli, M. Lebental and M. Brunel, "Waves and rays in plano-concave laser cavities: I. Geometric modes in the paraxial approximation," *European Journal of Physics*, 2017.
- [22] H. Kogelnik and T. Li, "Laser Beams and Resonators," *Applied Optics*, vol. 5, no. 10, pp. 1550-1567, 1966.
- [23] Wikimedia Commons, Wikimedia Commons, 20 03 2022. [Online]. Available: [https://commons.wikimedia.org/wiki/File:Laguerre-Gaussian\\_modes.png](https://commons.wikimedia.org/wiki/File:Laguerre-Gaussian_modes.png).
- [24] Wikimedia Commons, Wikimedia Commons, 20 03 2022. [Online]. Available: <https://commons.wikimedia.org/wiki/File:Hermite-gaussian.png>.



- [25] S. SAGHAFI and C. J. R. SHEPPARDt, "Near field and far field of elegant HermiteGaussian and Laguerre-Gaussian modes," *JOURNAL OF MODERN OPTICS*, vol. 45, 1998.
- [26] S. Schmid, K. D. Jensen, K. H. Nielsen and a. A. Boisen, "Damping mechanisms in high-Q micro and nanomechanical string resonators," *PHYSICAL REVIEW B*, vol. 84, no. 165307, 2011.
- [27] X. Zhou, S. Venkatachalam, R. Zhou, H. Xu, A. Pokharel, A. Fefferman, M. Zaknounge and C. Eddy, "High-Q Silicon Nitride Drum Resonators Strongly Coupled to Gates," *Nano Letters*, pp. 5738-5744, 2021.
- [28] COMSOL, COMSOL, 20 03 2022. [Online]. Available: <https://www.comsol.com/multiphysics/eigenfrequency-analysis>.
- [29] B. P. Dustin Kleckner, E. Jeffrey, P. Sonin, S. M. Thon and a. D. Bouwmeester, "Optomechanical trampoline resonators," *Optics Express*, vol. 19, no. 20, pp. 19708-19716, 2011.
- [30] M. Bao, "Analysis and Design Principles of MEMS Devices," ScienceDirect, 2005, pp. 115-174.
- [31] I. Wilson-Rae, R. A. Barton, S. S. Verbridge, D. R. Southworth, B. Ilic, H. G. Craighead and a. J. M. Parpia, "High-Q Nanomechanics via Destructive Interference of Elastic Waves," *PHYSICAL REVIEW LETTERS*, vol. 106, 2011.
- [32] E. Serra, B. Antonio, F. Marin, F. Marino, N. Malossi, B. Morana, P. Piergentili, G. A. Prodi, P. M. Sarro, P. Vezio, D. Vitali and a. M. Bonaldi, "Silicon-nitride nanosensors toward room temperature quantum optomechanics," *Journal of Applied Physics*, no. 130, 2021.
- [33] S. A. Fedorov, N. J. Engelsen, A. H. Ghadimi, M. J. Beryhi, R. Schilling, D. J. Wilson and a. T. J. Kippenberg1, "Generalized dissipation dilution in strained mechanical resonators," *PHYSICAL REVIEW B*, vol. 99, 2019.
- [34] N. J. Engelsen, A. R. Agrawal and D. J. Wilson, "ULTRA-HIGH-Q NANOMECHANICS THROUGH DISSIPATION DILUTION," in *2021 21st International Conference on Solid-State Sensors, Actuators and Microsystems (Transducers)*, Virtual, 2021.
- [35] L. Sementilli, E. Romero and W. P. Bowen, "Nanomechanical Dissipation and Strain Engineering," *Advanced Funcation Material*, vol. 32, no. 3, 2021.

- [36] D. J. Griffiths, "Introduction to Electrodynamics, 2nd," 1999, pp. 398-405.
- [37] R. C. Jaeger, Introduction to Microelectronic, Upper Saddle River, New Jersey: Prentice Hall, 2002.
- [38] B. Belgacem, D. Alquier, P. Muralt, J. Baborowski, S. Lucas and R. Jerisian, "Optimization of the fabrication of sealed capacitive transducers using surface micromachining," *Journal of Micromechanics and Microengineering*, vol. 14, 2003/2004.
- [39] Q. Wang, G. Luo, Y. Kusano and D. A. Horsley, "Low thermal budget surface micromachining process for piezoelectric micromachined ultrasonic transducer arrays with in-situ vacuum sealed cavities," in *Proceedings of the Hilton Head Workshop*, 2018.
- [40] R. B. Roy, O. Farhanieh, A. S. Ergün and A. Bozkurt, "Fabrication of High-Efficiency CMUTs With Reduced Parasitics Using Embedded Metallic Layers," *IEEE Sensors Journal*, vol. 17, no. 13, pp. 4013-4020, 2017.
- [41] G.-L. Luo, Y. Kusano and D. Horsley, "Immersion PMUTs Fabricated with a Low Thermal-Budget Surface Micromachining Process," in *IEEE International Ultrasonics Symposium (IUS)*, 2018.
- [42] L. F. Buchmann, L. Zhang, A. Chiruvelli and P. Meystre, "Macroscopic Tunneling of a Membrane in an Optomechanical Double-Well Potential," *PHYSICAL REVIEW LETTERS*, vol. 108, no. 210403, 2012.
- [43] Q. Li, H. Goosen, F. v. Keulen, J. v. Beek and G. Zhang, "Assessment of testing methodologies for thin-film vacuum MEMS packages," *Microsystem Technologies*, vol. 15, pp. 161-168, 2009.
- [44] C. Liu and Y.-C. Tai, "Sealing of Micromachined Cavities Using Chemical Vapor Deposition Methods Characterization and Optimization," *IEEE JOURNAL OF MICROELECTROMECHANICAL SYSTEMS*, vol. 8, no. 2, 1999.
- [45] J. Sarkar, "Sputtering Materials for VLSI and Thin Film Devices," in *Chapter 2 - Sputtering and Thin Film Deposition*, William Andrew, 2014, pp. 93-170.
- [46] T. Karabacaka and T.-M. Lu, "Enhanced step coverage by oblique angle physical vapor deposition," *Journal of Applied Physics*, vol. 97, no. 124504, 2005.
- [47] J. B. Fortin and T.-M. Lu, Chemical Vapor Deposition Polymerization: The Growth and Properties of Parylene Thin Films, Springer Science & Business Media, 2013.

- [48] HEIDELBURG INSTRUMENTS, "MLA150 Maskless Aligner," 2019. [Online]. Available: <https://nanofab.sites.olt.ubc.ca/files/2021/04/MLA150-User-Guide.pdf>. [Accessed 26 03 2022].
- [49] R. Arghavani, L. Xia, H. M'Saad, M. Balseanu, G. Karunasiri, A. Mascarenhas and S. Thompson, "A reliable and manufacturable method to induce a stress of >1 GPa on a P-channel MOSFET in high volume manufacturing," *IEEE Electron Device Letters*, vol. 27, no. 2, pp. 114-116, 2006.
- [50] M. Balseanu, L. Xia, V. Zubkov, M. Le, J. Lee and H. M'Saad, "Stress Modulation of PECVD Silicon Nitride," in *208th ECS Meeting, Abstract #532*, Los Angeles, 2005.
- [51] M. Belyanskaya, M. Chace, O. Gluschenkov, J. Kempisty, N. Klymko, A. Madan, A. Mallikarjunan, S. Molis, P. Ronsheim, Y. Wang, D. Yang and Y. Li, "Methods of producing plasma enhanced chemical vapor deposition silicon nitride thin films with high compressive and tensile stress," *Journal of Vacuum Science & Technology A*, vol. 26, no. 517, 2008.
- [52] D. Hunger, T. Steinmetz, Y. Colombe, C. Deutsch, T. W. Hänsch and J. Reichel, "A fiber Fabry–Perot cavity with high finesse," *New Journal of Physics*, vol. 12, no. 065038, 2010.
- [53] G. Wachter, S. Kuhn, S. Minniberger, C. Salter, P. Asenbaum, J. Millen, M. Schneider, J. Schalko, U. Schmid, A. Felgner, D. Hüser, M. Arndt and M. Trupke, "Silicon microcavity arrays with open access and a finesse of half a million," *light: science & applications*, vol. 8, 2019.
- [54] C. Vallance, A. A. P. Trichet, D. James, P. R. Dolan and J. M. Smith, "Open-access microcavities for chemical sensing," *Nanotechnology*, 2016.
- [55] A. Reiserer and G. Rempe, "Cavity-based quantum networks with single atoms and optical photons," *2015*, vol. 87, no. 4, pp. 1379-1418.
- [56] C. A. Potts, A. Melnyk, H. Ramp, M. H. Bitarafan, D. Vick, L. J. LeBlanc, J. P. Davis and R. G. DeCorby, "Tunable open-access microcavities for on-chip cavity quantum electrodynamics," *Applied Physics Letters*, vol. 108, no. 4, 2016.
- [57] R. C. Pennington, G. D'Alessandro, J. J. Baumberg and M. Kaczmarek, "Spectral properties and modes of surface microcavities," *PHYSICAL REVIEW A*, vol. 79, no. 063822, 2009.

- [58] J. Benedikter, T. Hümmer, M. Mader, B. Schlederer, J. Reichel, T. W. Hänsch and D. Hunger, "Transverse-mode coupling and diffraction loss in tunable Fabry-Perot microcavities," *New Journal of Physics*, vol. 17, no. 053051, 2017.
- [59] J. Volz, R. Gehr, G. Dubois, J. Estève and J. Reichel, "Measurement of the internal state of a single atom without energy exchange," *Nature*, vol. 475, pp. 210-213, 2011.
- [60] M. Uphoff, M. Brekenfeld, G. Rempe and S. Ritter, "Frequency splitting of polarization eigenmodes in microscopic Fabry-Perot cavities," *New Journal of Physics*, vol. 17, no. 013053, 2015.
- [61] L. Flatten, A. Trichet and J. Smith, "Spectral engineering of coupled open-access microcavities," *Laser and Photonic Reviews*, vol. 10, no. 2, pp. 257-263, 2015.
- [62] J.-M. Cui, K. Zhou, M.-S. Zhao, M.-Z. Ai, C.-K. Hu, Q. Li, B.-H. Liu, J.-L. Peng, Y.-F. Huang, C.-F. Li and G.-C. Guo, "Polarization nondegenerate fiber Fabry-Perot cavities with large tunable splittings," *Applied Physics Letters*, vol. 112, no. 171105, 2018.
- [63] S. Garcia, F. Ferri, K. Ott, J. Reichel and R. Long, "Dual-wavelength fiber Fabry-Perot cavities with engineered birefringence," *Optics Express*, vol. 26, no. 1, pp. 22249-22263, 2018.
- [64] H. Wang, Y.-M. He, T.-H. Chung, H. Hu, Y. Yu, S. Chen, X. Ding, M.-C. Chen, J. Qin, X. Yang, R.-Z. Liu, Z.-C. Duan, J.-P. Li, S. Gerhardt, K. Winkler, J. Jurkat, L.-J. Wang, N. Gregersen, Y.-H. Huo, Q. Dai, S. Yu and S. Höfli, "Towards optimal single-photon sources from polarized microcavities," *Nature Photonics*, vol. 13, pp. 770-775, 2019.
- [65] F. M. Buters, M. J. Weaver, H. J. Eerikens, K. Heeck, S. d. Man and D. Bouwmeester, "Optomechanics with a polarization nondegenerate microcavity," *PHYSICAL REVIEW A*, vol. 94, no. 063813, 2016.
- [66] T. D. Barrett, T. H. Doherty and A. Kuhn, "Pushing Purcell enhancement beyond its limits," *New Journal of Physics*, vol. 22, no. 063013, 2020.
- [67] A. Yariv and P. Yeh, *Photonics*, Oxford University Press, 2006.
- [68] M. Durand, Y. Wang and J. Lawall, "Accurate Gouy phase measurement in an astigmatic optical cavity," *Applied Physics B*, vol. 108, pp. 749-753, 2012.
- [69] J. Maldaner, S. A. Sumaiidae and R. G. DeCorby, "Theoretical study of silicon-based Bragg mirrors for cavity QED applications," *JOSA B*, vol. 37, no. 12, pp. 3707-3713, 2020.

- [70] Q. Lin, J. Rosenberg, D. Chang, R. Camacho, M. Eichenfield, K. J. Vahala and O. Painter, "Coherent mixing of mechanical excitations in nano-optomechanical structures," *Nature Photonics*, vol. 4, pp. 236-242, 2010.
- [71] T. Lee and H. Iizuka, "Acoustic resonance coupling for directional wave control: from," *New Journal of Physics*, vol. 21, no. 043030, 2019.
- [72] S. Stassi, A. Chiadò, G. Calafiore, G. Palmara, S. Cabrini and C. Ricciardi, "Experimental evidence of Fano resonances in nanomechanical resonators," *Scientific Reports*, vol. 7, no. 1065, 2017.

## **Appendix A- Record of Fabrication of the Device**

This document recorded the observation, experience, result, and analysis for the MIM fabrication run performed by Lintong. MIM stands for the membrane in the middle optomechanical device.

The device fabrication can be separated into steps:

1. The AR (antireflection) coating, bottom mirror deposition, and membrane deposition
2. Photolithography, Teflon deposition, and liftoff
3. Top mirror deposition and RTA
4. Photolithography (Alignment), etch hole etching, and membrane release

This report will discuss each step and provide instructions for the next fabrication run.

### **1. The AR coating**

The AR coating is deposited by the Trion PECVD system (plasma-enhanced chemical vapor deposition), using the recipe “standard nitride”. Detailed steps are listed below:

1. Piranha double side polished wafer (DSP)
2. Flexus on DSP
3. Flexus on test wafer 1
4. PECVD on test wafer 1
5. Flexus on test wafer 1, calibrate the deposition time
6. Filmetrix on test wafer 1
7. PECVD on the backside of the wafer (DSP) (SiN 193 nm)
8. Filmetrix on DSP
9. Flexus on DSP

, where the Flexus performs the thin film stress measurement and the Filmetrix performs the thin film thickness measurement.

As the result, the thickness of the AR coating is 176 nm, and the stress of the film is 362.2MPa compressive.

## 2. Bottom mirror deposition

Sputter deposition of the bottom mirror is performed by DOUG sputtering system. SOP can be found in the group drive.

The bottom mirror is a 3 period Si/SiO<sub>2</sub> mirror with 200 nm Si Sacrificial Layer and 30 nm SiO<sub>2</sub> Etch Stop.

Layer	Thickness (nm)	Time	Voltage	Arcing
Si Sacrificial Layer	200	23'8	567	no
SiO <sub>2</sub> Etch Stop	30	1'55	557	no
QWS Si	111	12'53	568	no
QWS SiO <sub>2</sub>	269	17'17	558	no
QWS Si	111	12'53	568	no
QWS SiO <sub>2</sub>	269	17'17	556	no
QWS Si	111	12'53	567	no
QWS SiO <sub>2</sub>	269	17'17	559	no

Table A.1 The detailed record of the sputtering deposition of bottom mirror

The target I used was RGD-rSi-8, and RGD-aSi-5, and there is some crack on the aSi target but turnout there was no arcing.

### **3. Membrane deposition**

The membrane desired is a 150 nm PECVD SiN high tensile-stressed membrane. Using the standard nitride recipe, the thin film is highly compressive stressed (700MPa compressive), even after annealing, the stress is about 300 MPa tensile. Thus, I modified the PECVD recipe a

The deposition pressure was increased from 1000 mTorr to 1500 mTorr, RF power was increased from 80W to 120W, and substrate temperature was decreased to 300C from 325C. The SiN thickness is less consistent due to the higher pressure.

The membrane has been annealed at 600 degrees for 2 hours to bake out the hydrogen – Silicon bonds. To be precise about the annealing recipe, the annealing will ramp up from 450C to 600C in 2 hours, and keep at 600C for 2 hours, and then ramp down to 450 C for 2 hours. The film stress is 250 MPa compressive and 984 MPa tensile before and after annealing respectively.

Due to the complex optical structure of the bottom mirror, the thickness of the membrane is very hard to measure by VASE of Filmetrix, however, the Silicon Nitride thickness of the test wafer is 160 nm on average, which is close to the desired thickness.

### **4. Photolithography for the alignment mark**

HMDS treatment is before the photolithography to promote adhesion. The photoresist was AZ 1512 photoresist. 5 milliliters of photoresist are enough for a 4-inch wafer. And the dose was 100mJ. The mask aligner I used was the Heidelberg MLA-150 mask-less aligner. The developer I used was the AZ 400K 1:4 developer, soaked in for 40 s. Moreover, both spin and bake recipes of AZ 1512 are loaded on the spinner. Alignment mark photolithography does not require precision because this will be the baseline for the later photolithographic steps.



## 5. Etching of the alignment mark

The etching process is performed by ICPRIE Cobra, the recipe used was SiO<sub>2</sub>-Ta<sub>2</sub>O<sub>5</sub>-TiO<sub>2</sub> recipe.

The procedures are as follows:

1. Clean with SF<sub>6</sub> 10 min, use Cobra cleaning wafer provided by the NanoFab.
2. Conditioning (SiO<sub>2</sub>-Ta<sub>2</sub>O<sub>5</sub>-TiO<sub>2</sub>) 5 min, use Cobra cleaning wafer
3. Etching (SiO<sub>2</sub>-Ta<sub>2</sub>O<sub>5</sub>-TiO<sub>2</sub>) 5 min

## 6. Photolithography for the dome mask

This mask is for the lift-off of the Teflon deposition. I used a similar recipe for this mask:

- HMDS
- AZ 1512 110mJ for a 405 nm laser
- MLA-150 Aligner

This time alignment is required, the alignment mark position is manually input into the system, which is  $((x, y) = (\pm 27150, \pm 31000) \text{ microns})$ . When performing alignment, the pneumatic alignment method is required, since the optical alignment method is only for a small sample such that the pneumatic alignment cannot be performed. Moreover, only 4 alignment marks are required, the overall alignment will not benefit from additional alignment marks.

- AZ400K developer 40s to take out, if not fully developed, put the sample in developer for another 20s.

## 7. Estralus Teflon deposition

The Teflon deposition method is a part of the BOSCH process. Procedures are given below:

1. Chamber cleaning with Estralus cleaning wafer provided by the Nanofab for 10 minutes.
2. Conditioning using the Decorby Dep modified recipe for 5 min, using the same wafer.
3. Quarter a wafer and use a crystal bond to mount a quartered wafer on a carrier wafer.
4. Perform deposition on the quartered wafer using Decorby Dep Val recipe for 30 s and do a scratch test. If the plasma is not ignited at a 25% angle of the turbopump, try reducing the pump angle to 24%. It is also noteworthy that the Teflon deposition is highly dependant on the previous deposition steps.
5. Repeat for the other three quartered wafers or pass the scratch test, which is using a Teflon tweezer to drag from the surface, do not push the tweeter, just use its mass.
6. Perform deposition on the device wafer using Decorby Dep valve recipe for 10 s.
7. If needed, use Filmetric to measure the thickness of the Teflon film.
8. After deposition of four of the quartered wafer, a test deposition on a full test wafer is performed. For this test run, the thickness of the Teflon measured by Filmetrix was 22nm, and the deposition time was 7 seconds, and the percentage of the turbopump was 24 percent.
9. Perform actual deposition on the device wafer, as a result, the thickness of Teflon on the device wafer was 13nm, with 7 s of deposition time and 24% of the valve percentage.
10. After device deposition, a chamber clean procedure of 10 min was performed with the wafer provided by NanoFab.

Below is the result of the scratch test to the deposited Teflon on the quartered test wafer.

Number of the quarter	Deposition time	Pass test?
Q1	30s	Yes

Q2	30s	No
Q3	30s	No
Q4	7s	Not applicable, too thin

Table A.2 The result from scratch test using Estralus System for Teflon deposition

Recipe	Power (W)	Deposition time (s)	Pressure setpoint (mTorr)	Observed pressure during 10s dep (mTorr)	C4F8 flow rate (sccm)	Chuck temp (°C)	Measured thickness (nm)
DeCorby Dep	600	10	5	5.5	60	0	~45
Modified	600	10	5	4.2 - 4.5	40	0	45 - 50
New Test	600	10	4		40	0	

Table A.3 The recipe of Estralus for Teflon deposition

### 11. Liftoff process

The liftoff process is performed by putting the wafer into an acetone bath and sonicating the wafer for 1 hour. When finished with the lift-off process, the sample was cleaned by rinsing with acetone, IPA, and DI water twice, and then put into the dump rinser for 1 cycle.

**This process will need a big amount of acetone because the acetone evaporates fast.** And if some photoresist residue is formed on the back side of the wafer, we can use a cleanroom wipe to wipe it down.

## 12. Top mirror deposition

The top mirror is a 4.5 period Ta<sub>2</sub>O<sub>5</sub>/SiO<sub>2</sub> QWS at 1550 nm.

Detailed parameters are listed below:

Layer	Thickness (nm)	Time	Voltage	Arcing
Ta <sub>2</sub> O <sub>5</sub>	186	17'29	511	no
SiO <sub>2</sub>	265	17'33	524	no
Ta <sub>2</sub> O <sub>5</sub>	186	17'29	518	no
SiO <sub>2</sub>	265	17'33	525	no
Ta <sub>2</sub> O <sub>5</sub>	186	17'29	520	no
SiO <sub>2</sub>	265	17'33	525	no
Ta <sub>2</sub> O <sub>5</sub>	186	17'29	520	no
SiO <sub>2</sub>	265	17'33	526	no
Ta <sub>2</sub> O <sub>5</sub>	186	17'29	520	no

Table A.4 The detailed record of the sputtering deposition of top mirror

It is noticeable that the deposition pressure is 3.7mTorr instead of 4mTorr, due to the location change of the vacuum gauge. It is important to use a cleanroom wipe to bring the wafer down.

The deposition rate of Tantalum pentoxide is affected by 'target poisoning', which means the target is 'poisoned' by the oxide formed on the target, which greatly affects the deposition rate of the Ta<sub>2</sub>O<sub>5</sub> layer, for example, two consecutive test layers of Ta<sub>2</sub>O<sub>5</sub> can have a deposition rate of 0.172 nm/s and 0.159 nm/s respectively. To reduce the target poisoning of the Tantalum target,

10 minutes “after-burn” was performed to etch the excessive oxide layer, to obtain a repeatable deposition rate.

### **13. Rapid thermal annealing (RTA)**

RTA was performed with the recipe “Decorby 400” by ramping the wafer to 400 degrees Celsius. The thermal couple temperature gauge was used for more accurate temperature measurement. And most of the 50-micron diameter domes were ideally buckled, some of the 70- and 100-microns domes are popped off. The general yield of the whole device is estimated to be 50 percent.

### **14. Photolithography for the access hole mask**

This mask is for the access hole etching, this time we need a thicker photoresist for the etching.

Important parameters are listed:

- HMDS
- AZ 4620,600 mJ, normal depth of focus.
- MLA150 Aligner
- AZ400K developer and the development time was 2min 20s.
- Spinner #2 with the standard spinning recipe of AZ 4620
- A multiple-stage baking recipe is employed

For the photolithography of AZ 4620 resist using MLA 150 aligner:

1. Choose pneumatic alignment methods to reduce the error.
2. When using the AZ 4620 recipe, use the normal depth of focus, because when the large or extra larger depth of focus was selected, 99% and 99.5% percent of light is blocked to increase the depth of focus. This function is mainly used on very thick photoresists (about 100um) to avoid a cone shape of the vertical profile.

For the baking process:

1. SOP baking
2. Rehydrate for 15 min
3. 90s baking at 115 degrees Celsius
4. Rehydrate for 15 min

After the baking, the wafer is ready for alignment.

The alignment was accurate, all the access hole was aligned with the dome microcavity.

### **15. Cobra etching**

The etching process is performed by ICPRIE Cobra, the recipe used was SiO<sub>2</sub>-Ta<sub>2</sub>O<sub>5</sub>-TiO<sub>2</sub> recipe.

The procedures are as follow:

1. Clean with SF<sub>6</sub> 10 min, use Cobra cleaning wafer provided by the Nanofab.
2. Conditioning (SiO<sub>2</sub>-Ta<sub>2</sub>O<sub>5</sub>-TiO<sub>2</sub>) 5 min, use Cobra cleaning wafer
3. Etching (SiO<sub>2</sub>-Ta<sub>2</sub>O<sub>5</sub>-TiO<sub>2</sub>) about 18 min 20s.

In this stage, it is a good idea to dice the wafer and perform etching on each dice, the etching time is most likely on a trial base.

For the first trial, the etching time was 16 min 15s, and the etching did not go through the top mirror.

### **16. XeF<sub>2</sub> membrane release**

XeF<sub>2</sub> is used to release the membrane by selectively etching the Si Sacrificial layer. After releasing, a free-standing membrane is produced.

For this step, I used the standard recipe with 5 cycles.

1. Condition the chamber
2. 5 cycles etching.

### 17. Deposition of Si/SiO<sub>2</sub> QWS

After the XeF<sub>2</sub> membrane releasing another period of Si/SiO<sub>2</sub> quarter-wave stack was deposited by the DOUG system.

Layer	Thickness (nm)	Time	Voltage	Arcing
QWS SiO <sub>2</sub>	269	16'16	515	no
QWS Si	111	13'06	540	no

Table A.5 The detailed record of the sputtering deposition for vacuum sealing, first trial

Afterward, another period of Si/SiO<sub>2</sub> QWS as well as a capping layer of SiO<sub>2</sub> was deposited to seal the access holes and create a vacuum inside the microcavity.

Layer	Thickness (nm)	Time	Voltage	Arcing
QWS SiO <sub>2</sub>	269	16'16	504	no
QWS Si	111	13'06	541	no
SiO <sub>2</sub>	NA	60'	NA	no

Table A.6 The detailed record of the sputtering deposition for vacuum sealing, second trial